

Solvent-free solid-state materials for lithium
ion batteries based on $(AB)_n$ segmented
copolymers

DISSERTATION

Zur Erlangung des akademischen Grades

eines Doktors der Naturwissenschaften (Dr. rer. nat.)

in der Bayreuther Graduiertenschule für Mathematik und Naturwissenschaften

(BayNAT)

der Universität Bayreuth

vorgelegt von

Markus Sebastian Stihl

geboren in Freiburg im Breisgau

Bayreuth, 2024

Der experimentelle Teil der vorliegenden Arbeit wurde in der Zeit von September 2016 bis August 2021 in Bayreuth am Lehrstuhl für Makromolekulare Chemie I der Universität Bayreuth unter Betreuung von Herrn Professor Dr. Hans-Werner Schmidt angefertigt.

Vollständiger Abdruck der von der Bayreuther Graduiertenschule für Mathematik und Naturwissenschaften (BayNAT) der Universität Bayreuth genehmigten Dissertation zur Erlangung des akademischen Grades des Doktors der Naturwissenschaften (Dr. rer. nat.).

Dissertation eingereicht am: 08.09.2023

Zulassung durch das Leitungsgremium: 10.10.2023

Wissenschaftliches Kolloquium: 16.04.2024

Amtierender Direktor: Prof. Dr. Jürgen Köhler

Prüfungsausschuss:

Prof. Dr. H.-W. Schmidt (Gutachter)

Prof. Dr. A. Gröschel (Gutachter)

Prof. Dr. M. Bianchini (Vorsitz)

Prof. Dr. N. Vargas-Barbosa

Die vorliegende Arbeit wurde als Monographie verfasst.

Teile der Arbeit sind bereits in den folgenden Publikationen erschienen:

(AB)_n Segmented Copolyetherimides for 4D Printing

M. Jin, M. Stihl, R. Giesa, C. Neuber, H.-W. Schmidt

Macromol. Mater. Eng. **2020**.

Diese Publikation ist in der vorliegenden Arbeit mit der Literaturstelle [88] zitiert.

List of abbreviations

$^1\text{H-NMR}$	Proton nuclear magnetic resonance spectroscopy
3D	3-dimensional
a.u.	Arbitrary units
CEI	Cathode electrolyte interphase
CV	Cyclic voltammetry
DMA	Dynamic mechanical analysis
DMC	Dimethyl carbonate
DSC	Differential scanning calorimetry
EC	Ethylene carbonate
FT-IR	Fourier-transform infrared
GCPL	Galvanostatic cycling with potential limits
Jeff	Jeffamine ED-Series
LCO	Lithium cobalt oxide
LFP	Lithium iron phosphate
LIB	Lithium ion battery
LiTFSI	Lithium bis(trifluoromethane)sulfonimide
LMS	Lithium manganese spinel
LTN	Lithium transport number
NCA	Nickel cobalt aluminum
NMC	Nickel manganese cobalt
NMR	Nuclear magnetic resonance spectroscopy
PC	Propylene carbonate
PDMS	Polydimethylsiloxan
PEG	Poly ethylene glycol
PEIS	Potentiostatic electrochemical impedance spectroscopy
PEO	Poly ethylene oxide
PPO	Poly propylene oxide
PS	Lithium plating/stripping
PTCDA	3,4,9,10-Perylenetetracarboxylic dianhydride
PTCDI	3,4,9,10-Perylenetetracarboxylic diimide
SEI	Solid electrolyte interphase
SEM	Scanning electron
<i>t</i> BPA	<i>tert</i> phthalic anhydride
TGA	Thermogravimetric analysis

List of symbols

E	Potential
I	Current
V	Spannung
Δ	Delta
Θ	Theta
Π	pi
σ	Chemical shift

Table of contents

List of abbreviations	V
List of symbols	VI
Summary	1
Zusammenfassung	3
1. Introduction.....	7
1.1 Lithium ion batteries.....	7
1.1.1 Principle of lithium ion batteries	8
1.1.2 Dendrite and solid electrolyte interphase formation.....	10
1.2 Electrolyte materials for lithium ion batteries.....	12
1.3 Electrode materials for lithium ion batteries.....	19
1.3.1 Cathode materials for lithium ion batteries	20
1.3.2 Anode materials for lithium ion batteries	22
1.3.3 Energy levels in lithium ion batteries	24
1.3.4 Graphene.....	25
1.4 Characterization of lithium ion batteries	32
1.4.1 Electrochemical impedance spectroscopy (PEIS)	32
1.5.2 Cyclic voltammetry (CV)	34
1.5.3 Galvanostatic cycling with potential limits (GCPL)	35
1.5 (AB)_n segmented copolymers	36
2. Aim and Motivation of the thesis	41
3. Results and Discussion	45
3.1 (AB)_n segmented copolymers	45
3.1.1 Synthesis of (AB) _n segmented copolymers.....	45
3.1.2 Thermal characterization of (AB) _n segmented copolymers	58
3.1.3 Mechanical characterization	67
3.1.4 Melt-processing of (AB) _n segmented copolymers.....	68
3.1.5 Conclusion of the chapter	70
3.2 Melt-processable solvent-free solid-state electrolyte materials	71
3.2.1 Thermal characterization of electrolyte material	71
3.2.2 Melt-processing of electrolyte materials	81
3.2.3 Electrochemical characterization of electrolyte materials.....	84
3.2.4 Conclusion of the chapter	97

3.3	Melt-processable solid-state cathode materials.....	98
3.3.1	Synthesis and characterization of graphene via chemical vapor deposition	99
3.3.2	Melt-processing of cathode materials for lithium ion batteries	106
3.3.3	Conclusion of the chapter	109
3.4	Solvent-free solid-state lithium ion battery via melt-processing.....	110
3.4.1	Lithium ion battery via extrusion-based 3D printing.....	110
3.4.2	Conclusion of the chapter	115
4.	Experimental Part	117
4.1	Materials.....	117
4.2	Characterization methods.....	117
4.3	Processing methods.....	120
4.4	Synthesis of tBPA end-capped (AB)_n segmented copolymers.....	121
4.5	Synthesis of perylene end-capped (AB)_n segmented copolymers.....	123
4.6	Synthesis of graphene via chemical vapor deposition	124
5.	References.....	125
6.	Appendix	135
6.1	Additional topics investigated during the PhD	135
6.1.1	Physical vapor deposition of hole transport material for perovskite solar cell applications	135
7.	Acknowledgment.....	137
8.	(Eidesstattliche) Versicherungen und Erklärungen	139

Summary

Solid-state electrolytes have the potential to substantially improve lithium ion batteries by replacing liquid electrolyte materials. Metallic lithium as anode material can increase the battery's capacity by a factor of ten. The objective of this thesis is to synthesize and prepare tailored solid-state electrolyte materials based on $(AB)_n$ segmented copolymers. Using $(AB)_n$ segmented copolymers as matrix material allows battery fabrication in an all-dry process (without solvents) and the preparation of solvent-free solid-state lithium ion batteries.

To ensure melt-processing, the electrolyte material needs to feature low viscosities at elevated temperatures while transferring in an elastomeric state at temperatures below 80 °C, a typical maximum operating temperature for commercial lithium ion batteries. Additionally, sufficient mechanical stability and a certain elastomeric character at temperatures below 80 °C are beneficial to avoid the formation of lithium dendrites, as well as a suitable electrochemical stability towards the applied voltages is required to avoid degradation. Such a suitable matrix material for solid-state electrolyte materials can also be applied as binder for electrode materials.

In the first chapter, the *synthesis, optimization, and characterization of physically crosslinked $(AB)_n$ segmented copolymers* with desired thermal and mechanical properties are described. These copolymers consist of two segments, rigid perylene segments and soft polyether segments. Copolymers with tailored mechanical and thermal properties were synthesized by varying the chain length of the polyether segments. The perylene segments ensure mechanical stability due to the formation of a reversible physically crosslinked network *via* π - π interactions, while the amorphous polyether segments ensure the solvation of the lithium salt and the ion conductivity mandatory for lithium ion battery applications.

For the synthesis the solvent-free melt-polycondensation was developed and optimized concerning reaction time, avoidance of side reactions and scaled up to a 50 g scale. Detailed investigations of the thermally-triggered stacking behavior of perylene units in the copolymers were conducted showing the reversibility of the formation of physical crosslinks, also allowing melt-processing. The optimization of the melt-processing parameters was carried out, as well as melt-processing via extrusion-based 3D printing, was demonstrated.

The objective of the second chapter is the *preparation, processing, and characterization of solvent-free solid-state lithium ion battery electrolytes*. The electrolyte materials were based on the synthesized $(AB)_n$ segmented copolymers as matrix materials, allowing standard melt-processing techniques like compression molding or extrusion-based 3D printing. The filament for 3D printing was prepared *via* injection molding. The 3D printing process was optimized regarding printing parameters like e.g., pre-

load, speed, temperature, and 3D printing build surface. The thermal and electrochemical stability was investigated in detail. The ionic conductivity was investigated *via* potentiostatic electrochemical impedance spectroscopy measurements leading to a maximum of $2 \cdot 10^{-4} \text{ S cm}^{-1}$ (80 °C), a promising value for PEG-based systems. The mechanical stability of the electrolyte material could be demonstrated with plating and stripping experiments by *being stable for more than 1250 cycles, showing the material can avoid the formation of dendrites*. This allows the use of metallic lithium as anode material. This unique combination of mechanical, thermal, and electrochemical stability combined with the melt-processing capability opens up new opportunities in the field of solvent-free solid-state electrolyte materials and processing of all solid-state lithium ion batteries.

The third chapter deals with a *melt-processable lithium ion battery cathode material*. As electron conductive additive graphene was synthesized *via* chemical vapor deposition. Graphene sheets were synthesized at roughly 1000 °C using hot nickel foil as a catalyst and carrier substrate. However, the quality was not consistent and therefore not enough high-quality graphene could be synthesized. Therefore, commercially available graphene was used as an electron-conducting additive for the cathode material preparation. The cathode materials consist of three components: $(\text{AB})_n$ segmented copolymer as binder material, graphene as electron conducting material, and lithium iron phosphate as cathode active material. The cathode material was optimized regarding mixing temperature (200°C for 15 min and 220°C for 2 min) as well as the ratio of the components. The mixture was injection molded into a filament rod for extrusion-based 3D printing with a diameter of approx. 3 mm. The 3D printing process was optimized regarding pre-load, pressure, speed, temperature, and 3D printing build surface. Using extrusion-based 3D printing has the advantage to avoid solvents during battery fabrication. This new processing procedure enables new tailored cell designs as nearly any desired shape can be 3D printed.

The final chapter concludes with the *fabrication of a solvent-free solid-state melt-processed lithium ion battery*. The melt-processing was done *via* extrusion-based 3D printing and the printed battery was encapsulated in a coin cell. The solvent-free solid-state materials allowed the use of pure lithium as anode material making this a promising material for future investigations. A working 3D printed battery with a capacity of 80 mAh g^{-1} was achieved with a maximum coulombic efficiency of 96%, demonstrating the proof of principle to prepare functioning solvent-free solid-state lithium ion batteries *via* melt-processing without the use of solvents.

Zusammenfassung

Feststoffbatterien haben das Potential die Eigenschaften der Lithium Ionen Batterien durch den Einsatz von Feststoffelektrolyten erheblich zu verbessern. Metallisches Lithium als Anodenmaterial kann die Kapazität der Batterie um einen Faktor 10 erhöhen. Diese Doktorarbeit beschäftigt sich mit der Präparation von maßgeschneiderten Materialien für Feststoffbatterien basierend auf $(AB)_n$ segmentierten Copolymeren. Der Einsatz dieser Copolymere als Matrix- bzw. Bindermaterial erlaubt die lösungsmittelfreie Herstellung von feststoffbasierten Lithium-Ionen-Batterien.

Um eine Schmelzverarbeitung zu gewährleisten, muss das entsprechende Material eine geringe Viskosität bei hohen Temperaturen aufweisen und nach Abkühlen erstarren, um in Feststoffbatterien Verwendung finden zu können. 80 °C ist ein typisches oberes Limit des Temperaturbereichs in dem Lithium-Ionen-Batterien verwendet werden, somit muss der Feststoffelektrolyt unterhalb dieser Temperatur eine entsprechend hohe mechanische Festigkeit aufweisen und im verwendeten Spannungsfenster der Batterie eine ausreichende elektrochemische Stabilität zeigen, damit keine Zersetzung der Materialien stattfindet.

Das erste Kapitel umfasst die auf Schmelzverfahren basierende, *lösungsmittelfreie Synthese, Optimierung und Charakterisierung von physikalisch reversibel vernetzten $(AB)_n$ segmentierten Copolymeren*. Diese Copolymere weisen maßgeschneiderte thermische sowie mechanische Eigenschaften auf und bestehen aus zwei Segmenten, den steifen Perylensegmenten sowie den weicheren Polyethersegmenten. Durch Variation der Kettenlängen der Polyethersegmenten wurden die thermischen bzw. mechanischen Eigenschaften eingestellt. Die Perylensegmente sorgen für die mechanische Festigkeit durch von π - π Wechselwirkungen hervorgerufene physikalisch verknüpfte Vernetzungspunkte. Die Polyethersegmente sorgen für die notwendige Ionenleitfähigkeit.

Die Polykondensationsreaktion aus der Schmelze wurde hingehend der Reaktionszeit optimiert und das Auftreten von thermisch induzierten Nebenreaktionen wurde durch Veränderung der Reaktionsführung unterdrückt. Die Synthese der $(AB)_n$ segmentierten Copolymere konnte auf 50 g - Maßstab erfolgreich hochskaliert werden. Die thermisch induzierte reversible Verknüpfung der Perylensegmente wurde im Detail untersucht und analysiert. Die Optimierung der Parameter zur Schmelzverarbeitung wurde anhand des extrusionbasierten 3D Drucks demonstriert.

Das zweite Kapitel befasst sich mit der *Präparation und der Verarbeitung neuartiger lösungsmittelfreier Feststoffelektrolyte für Lithium-Ionen-Batterien*. Die Elektrolytmaterialien basieren auf den zuvor synthetisierten $(AB)_n$ segmentierten Copolymeren, welche als Matrixmaterial eingesetzt wurden. Dadurch wurde die Schmelzerarbeitung mittels Verfahren wie Heißpressen oder 3D Druck ermöglicht. Das Filament, welches für den 3D Druck verwendet wurde, wurde selbstständig mittels Spritzgusses

hergestellt und das Druckverfahren wurde in Bezug auf Vordruck, Geschwindigkeit, Temperatur und Druckunterlage optimiert und die thermischen und elektrochemischen Eigenschaften wurden im Anschluss im Detail untersucht. Die Ionenleitfähigkeit wurde mittels potentiostatischer elektrochemischer Impedanzspektroskopie analysiert und konnte mit einem Maximalwert von $2 \cdot 10^{-4} \text{ S cm}^{-1}$ (80 °C) bestimmt werden, welches einen hohen Wert für PEG-basierte Systeme darstellt. Die mechanische und elektrochemische Stabilität konnte durch *Plating/Stripping* Experimente verifiziert werden. Mit einer Stabilität des hergestellten Feststoffelektrolyten über mehr als 1250 Zyklen konnten herausragende Eigenschaften bestätigt werden. Ein Durchdringen des Feststoffelektrolyts von möglicherweise gebildeten Lithium-Dendriten konnte nicht beobachtet werden. Diese herausragende Leistung in Bezug auf mechanische, thermische und elektrochemische Eigenschaften in Verbindung mit der möglichen Schmelzverarbeitung eröffnet neue Möglichkeiten im Bereich der lösungsmittelfreien Feststoffelektrolyte für Lithium-Ionen-Batterien.

Im dritten Kapitel wird die *Präparation und Verarbeitung von Feststoffkathodenmaterialien* beschrieben. Graphen wurde mittels *chemical vapor deposition* hergestellt, mit heißer Nickelfolie als Katalysator, auf die Naphthalin aufgedampft wurde. Bei 1000 °C konnten die besten Ergebnisse erzielt und Graphen mit 1-2 Schichten erfolgreich hergestellt werden. Leider war die Qualität des synthetisierten Graphen über die gesamte Nickelfolie nicht ausreichend, um es in einer Lithium-Ionen-Batterie verwenden zu können. Daher wurde kommerzielles Graphen als elektronenleitendes Additiv in der Kathodenpräparation eingesetzt.

Die Kathodenmaterialien wurden in einem Mischer basierend auf drei Komponenten zusammen gemischt: dem $(AB)_n$ segmentierten Copolymer als Bindermaterial, Graphen als elektronenleitendes Material und Lithiumeisenphosphat als Aktivmaterial. Die Herstellung des Kathodenmaterials wurde hinsichtlich Mischungstemperatur, Verhältnis der Komponenten als auch Reihenfolge der Zugabe der Komponenten optimiert. Die Komponenten wurden bei 200 °C für 15 min und bei 220 °C für 2 min gemischt um eine homogene Mischung zu gewährleisten. Im Anschluss wurden für den extrusionsbasierten 3D-Druck mittels Spritzgusses Filamente mit einem Durchmesser von ca. 3 mm hergestellt. Das 3D-Druckverfahren wurden auch für diese Materialien in Bezug auf Druck, Geschwindigkeit, Temperatur und Druckunterlage optimiert. Die Verwendung der 3D-Druck Technik erlaubt die Präparation von Kathodenmaterialien ohne die Verwendung von Lösungsmitteln. Diese neue flexible Verarbeitungsmethode eröffnet die Möglichkeit mittels 3D Drucks beliebige Formen und Strukturen zu generieren.

Die Doktorarbeit schließt mit der *Herstellung einer funktionstüchtigen Lithium-Ionen-Batterie ab, hergestellt über die lösungsmittelfreie Schmelzverarbeitung der einzelnen Komponenten*. Der Elektrolyt als auch die Kathode wurden mittels 3D-Druck aus der Schmelze hergestellt, was neue Möglichkeiten

maßgeschneiderter Designs von Lithium-Ionen-Batterien ermöglicht. Die 3D-gedruckte Batterie wurde in einer Knopfzelle verschlossen und konnte unter Normalbedingungen betrieben werden. Als Materialien wurden ausschließlich lösungsmittelfreie Feststoffmaterialien verwendet, was Sicherheitsrisiken durch Lösungsmittelrückstände ausschließt, als auch die Verwendung von metallischem Lithium als Anodenmaterial ermöglicht, welches die Kapazität um ein Vielfaches im Vergleich zu graphitbasierten Lithium-Ionen-Batterien erhöhen kann.

Eine funktionstüchtige 3D gedruckte Batterie mit einer Kapazität von ca. 80 mAh g⁻¹ konnte erfolgreich hergestellt und vermessen werden. Die maximale Coulomb-Effizienz konnte mit 96 % bestimmt werden. Somit konnte der *proof of principle* für die Herstellung einer funktionstüchtigen lösungsmittelfreien Feststoff-Lithium-Ionen-Batterie mittels 3D Druck erbracht werden.

1. Introduction

1.1 Lithium ion batteries

Lithium ion batteries (LIBs) revolutionized the market as the most common energy storage device in the field of portable electronics, electric vehicle markets, and grid energy storage.^[1] Considering the impact of LIBs on daily life, John Goodenough, Stanley Whittingham, and Akira Yoshino were rewarded by winning the Nobel Prize in chemistry in 2019 for the development of lithium ion battery technology.^[2] As first choice for portable electronic devices LIBs gained their position on the market due to the combination of high energy densities and high operating voltages ($\approx 4V$)^[1,3,4] as well as their excellent cyclability^[4,5] and their more and more decreasing cost^[5]. The intense research all over the world made them the number one in terms of energy storage devices and could leave potential other technologies such as sodium-ion batteries^[6] or redox-flow batteries^[7] behind. LIBs are highly applicable in small electronic devices like smartphones, laptops, tablets, *etc.*^[4] Armand^[8] *et al.* was the first one to report the potential of intercalating materials as electrode materials enabling the flow of lithium ions from one electrode to another^[8,9]. Sony picked up on that technology and was the first company to manufacture, distribute and sell LIBs in 1991 featuring LiCoO₂-based cathode and carbon-based anode materials^[9].

However, LIBs show promising features not only in small electronic devices but also in the emerging field of e-mobility^[5,9,10], being already state-of-the-art power sources and promising candidates in large-size batteries.^[4] This allows the use of LIBs in pure electric or hybrid vehicles^[4,10], increasing the applicable market of LIBs even further. With the use of LIBs in electric vehicles the demands in terms of safety and high-energy density-related aspects are increasing.^[5,10,11] Conventional LIBs suffer from flammable liquid electrolyte materials posing a safety risk due to the possibility of a thermal runaway^[11–13] and carbon-based anode material suffering from insufficient energy densities.^[11,12] One common approach to avoid safety issues is to use solid-state materials as electrolyte materials.^[11,12] There are different kinds of solid-state electrolyte materials e.g., polymer-based^[14,15], inorganic^[15,16], and hybrid composite^[15,17] electrolyte materials.

1.1.1 Principle of lithium ion batteries

A LIB consists of three major components: The electrodes in anode and cathode as well as the electrolyte material. A schematic setup of a LIB is shown in **Figure 1**.

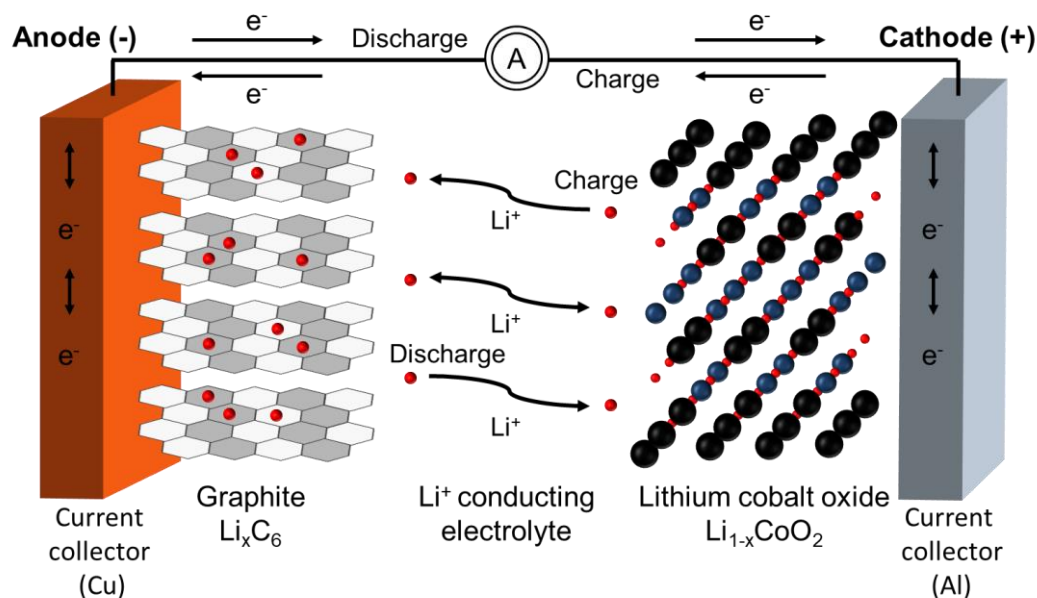


Figure 1: General schematic setup of a lithium ion battery (LIB). As standard anode material graphite is used. Here the Li-ion can intercalate in between the graphene sheets. A copper foil is used as a current collector to ensure fast transportation of the electrons. As cathode material metal oxides are used, in this case, lithium cobalt oxide with aluminum as a current collector. In between the electrodes, there is the electrolyte, responsible for the transportation of the lithium ions from one electrode to the other. In commercially available LIBs the electrolyte consists of liquid materials like ethylene carbonates or propylene carbonates. During discharge, the lithium ions move out of the graphite through the electrolyte towards the cathode. In the meantime, the electrons move through the device toward the cathode. For the charge process it applies *vice versa*. Figure adapted with permission from ^[18].

Apart from the electrodes and electrolyte materials, a LIB consists of current collectors on each side. Common materials are copper on the anode side and aluminum on the cathode side. Anode materials mainly consist of carbon-based materials like graphite^[19] or related materials e.g., graphene.^[20] Here, the lithium ions intercalate between the graphene layers^[5,9,19,20] which are linked by weak π - π interactions.^[19] Upon discharging, the lithium ions deintercalate out of the anode material and move through the electrolyte toward the cathode. At the cathode, the lithium ions incorporate into the lattice of the cathode active material^[21]. In the case of LIBs with liquid electrolytes a separator is necessary. The separator is a micro-porous polymer film that allows lithium ions to pass while acting as an electronic isolator, thus avoiding short-circuiting of the battery.

Solid-state LIBs often do not use a separator since the solid-state electrolyte is responsible for the lithium ion transporting and the electron isolating features. Therefore, the electrolyte material has the crucial task to transport the lithium ions from one electrode to the other and must fulfill several

requirements, like good ionic conductivity as well as thermal, mechanical, and electrochemical stability. A high ionic conductivity usually benefits from an amorphous polymer since crystalline polymers can act as traps and therefore decrease the ionic conductivity.^[14] The electrolyte influences cell properties like cyclability, working temperature range, safety, and cell capacity significantly. Liquid LIB electrolyte materials consist of materials like ethylene carbonate (EC), propylene carbonate (PC), and mixtures thereof in combination with lithium salts. They show very good ionic conductivities of about $10^{-2} \text{ S cm}^{-1}$. With liquid electrolyte materials, safety issues can occur when used in combination with lithium metal as anode material due to residual solvents, flammable electrolyte materials as well as short circuits caused by lithium dendrites. Therefore, they are limited to intercalating electrode materials like graphite-based anodes. To overcome these issues the use of solid-state electrolyte materials gained more interest.^[21] Solid-state electrolytes show worse ionic conductivity in comparison to the liquid electrolytes. Nevertheless, they can avoid safety issues due to their mechanical stability and non-flammable behavior. Moreover, dendrite formation can be avoided by solvent-free electrolytes under certain conditions.^[21]

The third major component in LIBs is the cathode material. During discharge, the lithium ions get incorporated into the lattice of the cathode materials. Upon charge, the lithium ions move out of the lattice towards the anode. The cathode materials not only need to show good ionic conductivity but also good electronic conductivity ensuring a good connection to the current collector and external circuit. The current market is dominated by intercalating materials like lithium cobalt oxide (LCO), nickel-cobalt-aluminum (NCA), lithium manganese spinel (LMS), nickel-manganese-cobalt (NMC), or lithium iron phosphate (LFP) based cathode materials.^[22] The cathode materials differ in their electrochemical properties which leads to different applications of each cathode material depending on the requirements needed.

1.1.2 Dendrite and solid electrolyte interphase formation

The formation of dendrites is the biggest concern when thinking of high-capacity LIBs of the future. The capacity of commercial batteries can be drastically increased by switching from graphite-based anode materials to lithium metal anodes. Here, the theoretical capacity of the anode increases up to a factor of 10.^[10,19,23,24] There are three major holdbacks to using lithium metal-based batteries. The most famous issue is the formation of dendrites which lead to safety issues due to a short circuit reducing the cyclability of the battery cell.^[25] Another concern is the high reactivity of lithium which could lead to side reactions with other materials. The resulting side products can increase the resistance of the battery cell, decreasing its performance. A rather less discussed issue is the volume change of the lithium electrode during charge and discharge which is a non-neglectable amount. Expansion of the battery could lead to cracks which can damage the battery cell.

However, the biggest issue remains the formation of dendrites. The mechanism of the dendrite formation is illustrated in **Figure 2**.

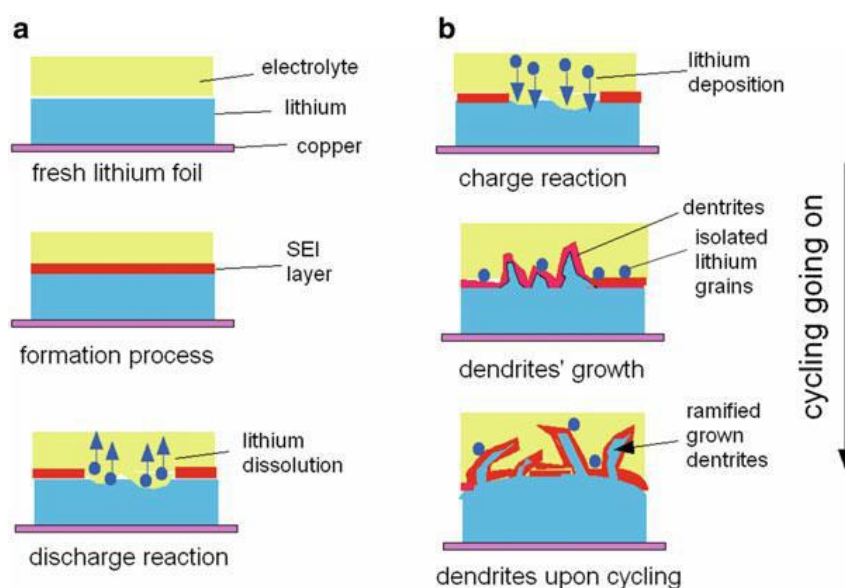


Figure 2: Sketch of the formation of lithium dendrites and deposition of lithium at the electrode surface for the first cycle **(a)** and upon further cycling **(b)**. Reprinted with permission from ^[26].

After the preparation of the LIB, during the first cycle, the solid electrolyte interphase (SEI) is formed **(a)**.^[24,26,27] The electrolyte material is thermodynamically unstable at low and very high potentials vs Li/Li^+ . Hence, during the first charge the electrolyte material begins to reduce and degrade.^[28] In the electrolyte material, there are several different materials involved. This leads to competing and parallel matrix and salt reduction processes resulting in the deposition of several organic and inorganic compounds. These compounds precipitate on the anode surface forming the SEI. The SEI is a multilayered interphase comprising an inorganic inner layer near the electrode mainly consisting of

lithium salts and an outer layer consisting of an organic layer depending on the used electrolyte.^[29] However, these layers are responsible for the kinetic stability of the electrolyte material against any further reduction during ongoing cycles.^[24,30] Although the SEI leads to an irreversible charge “loss”, this layer allows a good cyclability of the cell^[28]. In case of graphite-based intercalation anodes, the SEI also prevents co-intercalation of different compounds which could lead to the exfoliation of the graphite.^[31] An ideal SEI should have minimum electronic and maximum ionic conductivity. The kinetics should be fast allowing the formation to be completed before the onset of lithium ion intercalation.^[28] Up to now, the formation of the SEI cannot stop the formation of dendrites. So, with an increasing number of cycles (b) the dendrites are still formed. There is no memory effect of where the lithium ions came from, resulting in non-uniform deposition of lithium on the electrode surface.^[26,27] There are several approaches to prevent the formation of lithium dendrites, like adding nanodiamonds as seeds for the lithiation on the surface^[32], or modifying the SEI to get a mechanically stable layer, suppressing the lithium dendrites. Different approaches were used to increase the mechanical stability e.g., the addition of additives with a less negative redox potential acting as reagent or with the lithium, avoiding the reaction of the electrolyte itself.^[33]

Apart from tailoring the SEI, another promising approach to avoid dendrite formation is the preparation of solid electrolytes. Increasing the mechanical stability of the electrolyte can suppress the lithium dendrites, leading to safer lithium ion batteries.^[27]

1.2 Electrolyte materials for lithium ion batteries

There are several different options of electrolyte materials for LIB applications. A variety of electrolytes will be described in the following. Electrolytes for LIB applications must fulfill several requirements like: An electrochemical stability in a wide potential range (0-5.0 V)^[34], as well as good ionic conductivity to ensure a smooth ion transport.^[14] These requirements limit the choice of the corresponding materials and selected types of suitable electrolytes will be discussed in the following.

Liquid electrolytes

Commercially available liquid electrolytes are based on mixtures of alkyl carbonates like e.g., ethylene carbonate (EC), propylene carbonate (PC) or other organic esters of carbonic acid.^[34] Alkyl carbonates proved to be the best liquid electrolyte materials for lithium ion batteries.^[35] They show sufficient electrochemical stability while having very good ionic conductivity. The dependence on the solvent mixture composition, in this case of EC and ethyl methyl carbonate (EMC), the salt concentration, and the temperature is shown in **Figure 3**. The 5:5 mixture (top left) shows the best conductivity with a maximum of $1.6 \cdot 10^{-2} \text{ S cm}^{-1}$ at 60 °C. No matter the carbonate mixture, the ionic conductivity increases impacted by the lower viscosity with increasing temperature. In addition to the temperature dependence, there is a salt concentration dependency as well. There is a maximum of ionic conductivity where there is enough lithium salt to achieve a good conductivity. With increasing the amount further, the conductivity decreases due to the lithium salt being not soluble in the solvent anymore, resulting non-dissociated lithium salts which can lead to crystals in the electrolyte. The crystals can act as traps and therefore decrease the overall ionic conductivity. The optimal amount of lithium salt varies with every lithium salt and with every solvent composition used as an electrolyte. Using liquid electrolytes, usually, a separator is added to the cell to avoid short circuits. Liquid electrolytes shine due to their ionic conductivity but lack mechanical stability. Therefore, they do not allow the usage of metal lithium as an anode material. For this reason, commercial batteries based on liquid electrolytes use graphite-based intercalation anodes.

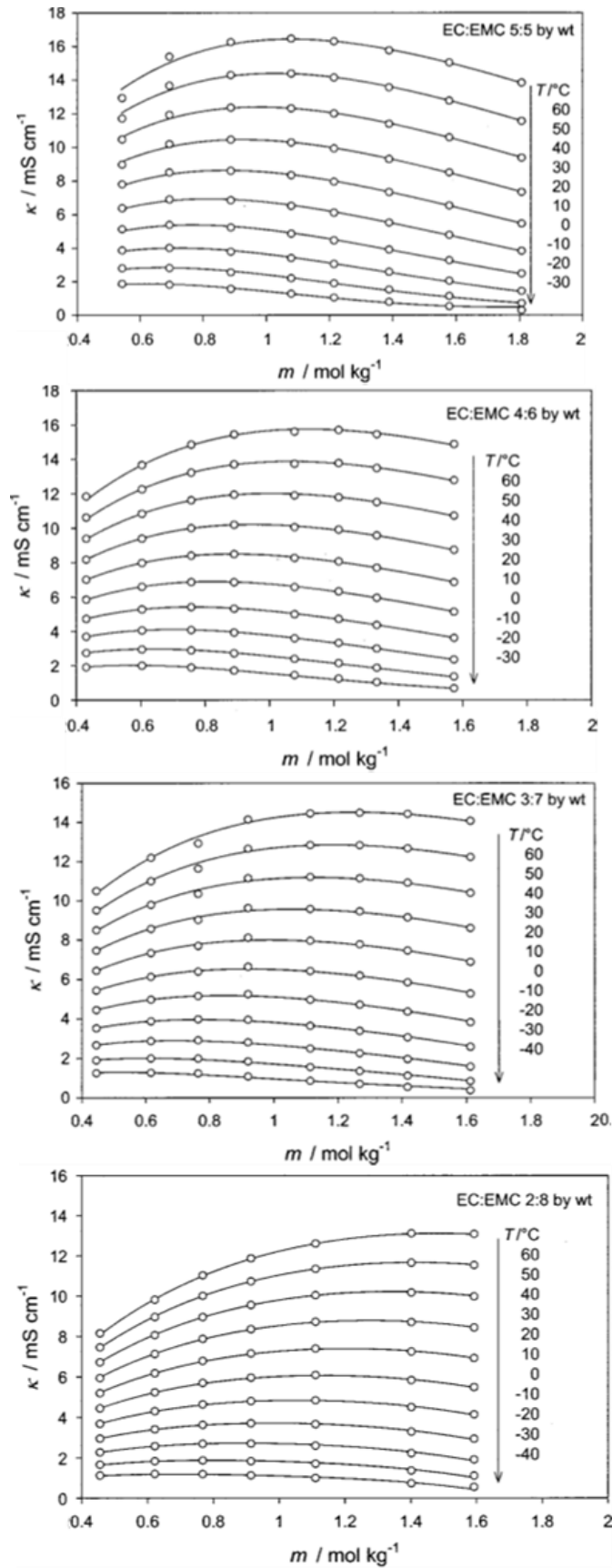


Figure 3: Conductivity depending on the salt concentration m at different temperatures and different solvent compositions. As lithium salt LiPF_6 was used. Reprinted with permission from [35].

Solid-state electrolytes

An approach to overcome the issue of dendrite formation is to increase the mechanical stability of the electrolyte in LIBs. Switching from liquid electrolyte to solid electrolyte materials could not only overcome the persistent problems of liquid electrolytes but enable the development of new battery chemistries.^[36,37] There are a variety of different solid-state electrolyte materials and an overview and a comparison of their performance are depicted in **Figure 4**.

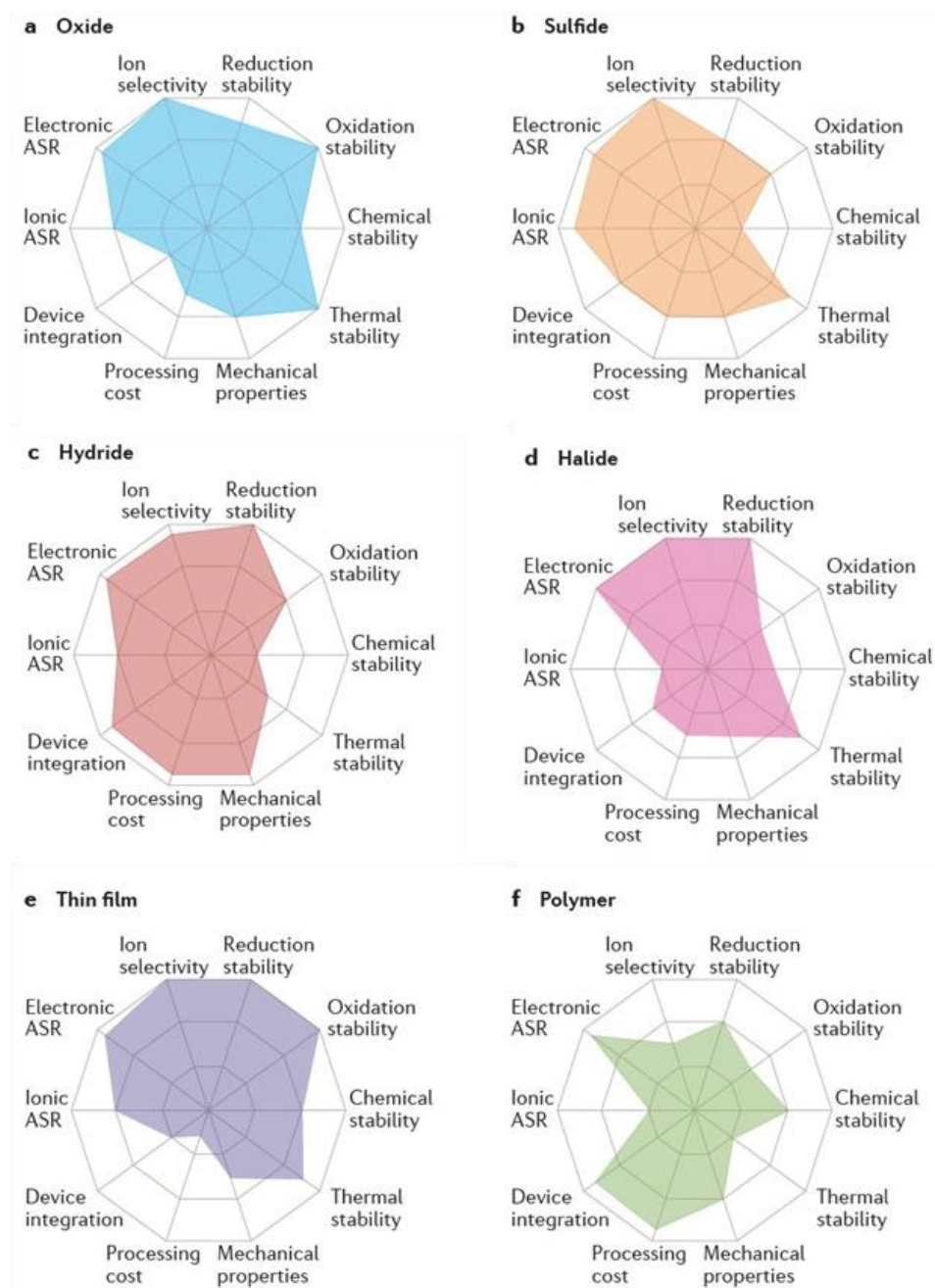


Figure 4: Performance comparison of different solid electrolyte materials with ASR being the area-specific resistance. Radar plots of **a)** oxide solid electrolytes, **b)** sulfide solid electrolytes, **c)** hydride solid electrolytes, **d)** halide solid electrolytes, **e)** thin-film electrolytes, and **f)** polymer solid electrolytes. Reprinted with permission from ^[36].

Ionic conductivity is the key property of solid electrolytes as the main drawback in comparison to liquid electrolytes. Therefore, the electrolytes have to show a sufficient ionic conductivity of $10^{-3} \text{ S cm}^{-1}$.^[37] Solid electrolytes must retain the required ionic conductivity while keeping their superior mechanical stability and safety. All types of solid electrolytes perform differently compared to their competitors. The decision of what kind of solid electrolyte to use depends on the desired application. Altogether, solid electrolytes allow the fabrication of all-solid-state LIBs which offer higher energy densities than traditional batteries.^[36] Additionally, the field of solid polymer electrolytes (SPEs) gains interest due to their easy processing and the possibility to produce them on large scale. Therefore, they will be discussed in more detail in the upcoming chapter.

Solid polymer electrolytes

In 1973, Fenton *et al.* was the first one to demonstrate alkali ion transport in a solid polymer material based on poly(ethylene oxide).^[38] This increased the scope of solid-state ionics which were no longer limited to inorganic materials. Moving from inorganic to polymeric materials allowed the development of flexible materials for LIBs^[39,40] and enabled new fields of application. Polymer electrolytes can be divided into three classes^[34,36]: dry solid polymer electrolytes^[41,42], composite polymer electrolytes.^[43,44], and gel polymer electrolytes.^[45,46] The used polymers can act either as gelation materials of liquid electrolyte or used as electrolyte material, with usually long chain-length, without any liquid electrolyte components. The neat polymer-based electrolytes can often be accompanied by an inorganic additive, resulting in composite polymer electrolytes. An overview of their conductivities is given in **Figure 5**.

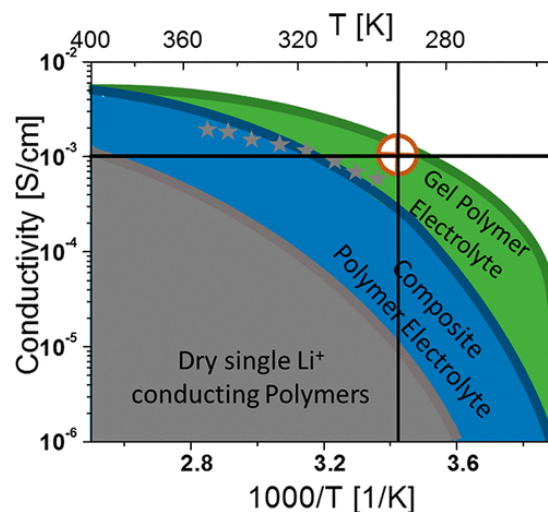


Figure 5: Temperature-dependent ionic conductivity comparison of different solid polymer electrolyte materials. Gel polymer electrolytes (green), composite polymer electrolytes (blue), as well as dry single lithium ion conduction polymers (grey). Gel polymer electrolytes still provide the highest ionic conductivity due to their amount of liquid electrolyte components. Second, the composite polymer electrolyte show promising ionic conductivities due to the addition of inorganic additives. Currently dry polymer electrolytes show the lowest ionic conductivity compared to afore-mentioned electrolytes. Reprinted with permission from ^[47].

The diagram shows the reported ionic conductivities for different types of polymer electrolytes. Gel polymer electrolytes show the highest average ionic conductivity in the literature.^[47] However, not only the ionic conductivity is a crucial property of solid polymer electrolytes but their mechanical stability to avoid dendrites as well as the transference number are important factors. Gel polymer electrolytes e.g., often suffer from the weakest mechanical stability.

The cross in the diagram describes the aimed ionic conductivity to make the material interesting for an industrial application.^[47] In the following, this chapter will only deal with dry polymer electrolytes, since they are the main interest of this thesis due to their superior mechanical stability.

Poly(ethylene oxide) (PEO) was the first polymer investigated in terms of LIB electrolyte materials. The long-time research on PEO materials makes them the only electrolyte material where the ion movement is investigated and determined in detail. **Figure 6** demonstrates the ion movement of lithium ions in PEO-based electrolytes.

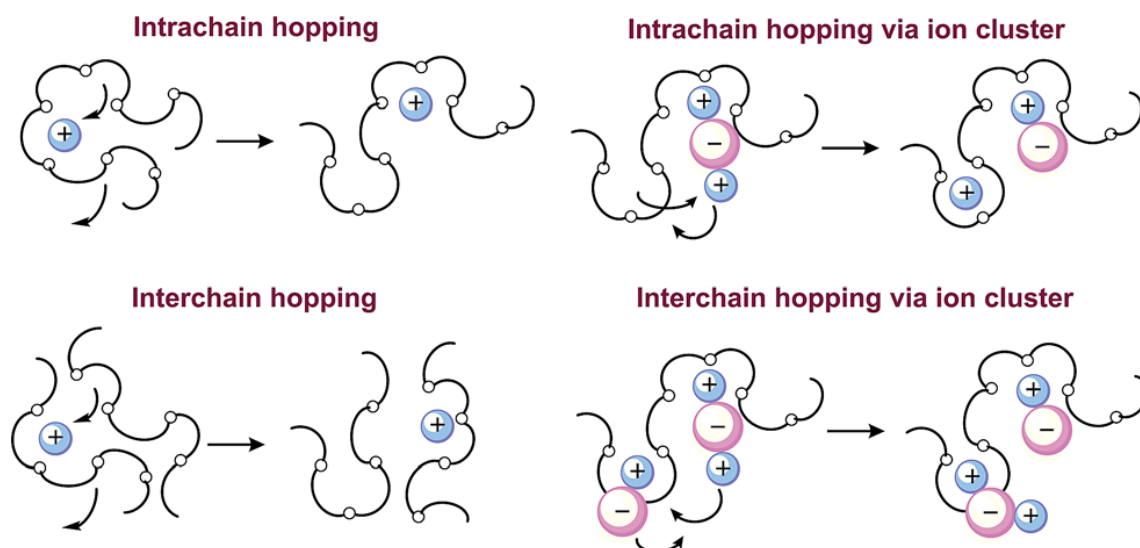


Figure 6: Movement mechanisms of lithium ions in PEO. Reprinted with permission from ^[48].

The ethylene oxide units have a high donor number for lithium ions and also show a high flexibility of the polymer chain which promotes rapid ion transport.^[48] In **Figure 6** (left) the lithium ions are coordinated by the ether oxygen atoms. The coordination from the ether oxygen atoms to the lithium ions is stronger than the competitive coordination with the counterion of the lithium salt, e.g. TFSI⁻. Here, during the breaking and forming of lithium-oxygen coordinative bonds, the lithium ions are transported *via* intrachain or interchain hopping. Accompanied by the gradual replacement of the ligands for the solvation of the lithium ions, the ongoing segmental rearrangement results in long-range displacement of lithium ions.^[48]

In general, the SPE is sandwiched between the anode and the cathode, acting as both electrolyte and separator. The polymer electrolyte plays a crucial role in the LIB and should inherently possess several properties:^[21,49]

High ionic conductivity: The electrolyte material should be a good ionic conductor and a good electronic isolator to minimize self-discharge of the battery. The aim is to achieve an ionic conductivity of $10^{-4} \text{ S cm}^{-1}$ or higher at ambient temperatures.^[21,34,49]

Appreciable lithium transference number: The lithium transference number describes what relative amount of charges are transported of the lithium ions compared to the counterions e.g., TFSI⁻. A large lithium transference number can reduce the concentration polarization of the battery over time. Reducing the mobility of the anions is the major approach to increase the transference number.^[21]

Good mechanical strength: Good mechanical strength is the most important factor thinking of electrolyte manufacturing. Mechanical strength is the main advantage that solid electrolytes have in comparison to liquid electrolyte systems. Polymer electrolytes should not be brittle as many ceramic inorganic electrolytes but be able to relax elastically to ensure safe processing and usage of the battery.^[14,21,49]

Wide electrochemical stability window: The electrochemical window in LIBs is defined as the potential range between the oxidation and the reduction reactions. The primary requirement for the electrolyte is to be electrochemically stable over the entire cell voltage, which means neither being readily reduced at the most negative potential, nor being readily oxidized at the most positive potential. The stability of the electrolyte determines the operation voltage limits of the LIB.

High thermal and chemical stability: The electrolyte material should be chemically stable towards all components in the cell such as the anode, cathode, current collector, and all used additives. A good thermal stability is mandatory for the safety of the battery even in the case of a thermal runaway or thermal abuse due to a short-circuiting of the battery cell.^[21]

As the high mechanical strength of polymeric electrolytes is advantageous in comparison to liquid electrolytes, most of the research focuses on increasing the mechanical stability while aiming for an ionic conductivity as high as possible. Different approaches are made to increase the mechanical integrity of the electrolyte e.g., building a crosslinked polymer network^[50,51] or synthesizing block copolymers.^[52]

Block copolymers attract due to their combination of an ion-conducting polymer block and a polymer block providing mechanical stability.^[52] Common examples are block copolymers based on polystyrene and PEG achieving ionic conductivities of $10^{-3} \text{ S cm}^{-1}$ at 90 °C.^[53] However, their synthesis is often very complex which makes it difficult to produce them on large scale, necessary for industrial applications.

Crosslinking the polymer allows higher working temperatures in the battery while still avoiding melting the electrolyte.^[48] Crosslinking is often conducted by applying heat, UV light, or by adding multifunctional comonomers. As the crosslinked electrolytes shine in their mechanical strength after the crosslinking, they have to be processed into their final shape beforehand. A change of shape of the electrolyte material is not possible any longer as soon as the material is crosslinked.

1.3 Electrode materials for lithium ion batteries

Electrode materials are responsible for energy storage in the LIB by intercalating lithium or by conversion of materials. Typical types of materials of each category are shown in **Figure 7**.

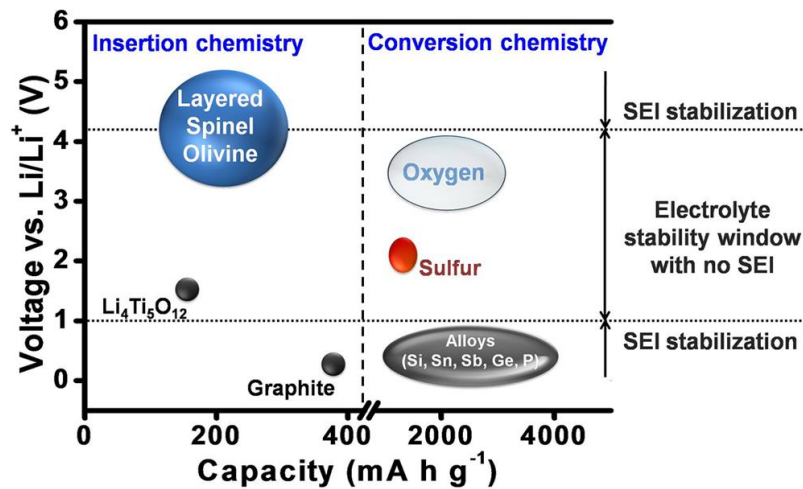


Figure 7: Capacity and voltage ranges of anode and cathode materials for LIBs. In the middle the voltage range is based on currently used liquid electrolytes. Top and bottom voltages are enabled by optimizing the SEI towards a more stable interface against the electrolyte. Reprinted with permission from^[1].

Composite electrodes consist of three different species of materials, each with different requirements.

Active material: The active material is the most important material and is responsible for the energy storage of the lithium ions which occurs *via* insertion or conversion chemistry as described above. As an anode material, the potential has to be very low, and as a cathode material, the potential has to be very high to ensure a high nominal voltage in the resulting battery. This will be discussed in more detail later on. In the following, if not declared otherwise, when reporting about electrode materials it refers to the active material used in the electrode.

Electron-conducting material: The electron-conducting material assures the smooth transport of electrons from the electrolyte surface of the electrode toward the current collector of the electrode. Since most of the active materials are rather insulating materials the addition of electron-conducting material is necessary.

Binder material: The third component is the binder material, assuring a homogeneous electrode material and ensuring a smooth contact between single active material particles as well as a smooth contact towards the current collector. Often the active material and the electron-conducting material are solid materials a homogeneous mixture is difficult. The binder material not only has to achieve a homogeneous mixture but has to allow sufficient lithium ion conducting abilities to ensure the lithium transport from the electrolyte interface of the electrode towards the electrode material at the back end towards the current collector.

1.3.1 Cathode materials for lithium ion batteries

Cathode materials used in LIBs are responsible to incorporate the lithium ions during discharge. As mentioned before, the cathode material can store lithium ions either *via* insertion or conversion chemistry. The current market of cathode materials is dominated by intercalating materials like lithium cobalt oxide (LCO), nickel-cobalt-aluminum (NCA), lithium manganese spinel (LMS), nickel-manganese-cobalt (NMC), or lithium iron phosphate (LFP) based cathode materials.^[22] The cathode materials differ in terms of crystal structure and array.^[2] There are three groups the crystal structures are divided in: layered (e.g., NMC, LCO), spinel (e.g., LMS), and the more complex polyanion oxides.^[2] Usually, a good cation ordering benefits the lithium ion diffusion which is critical for a good cathode material. LiCoO_2 (LCO) was the first cathode material to be commercially relevant and is up to now one of the best of its kind, but with 140 mAh g^{-1} lacks a high capacity.^[26] The loss of oxygen over time with an increasing number of cycles limits LCO in terms of cyclability. Considering graphite as an anode material, often the cathode material is the limiting factor in terms of the overall capacity. Therefore, materials with a higher specific capacity of about 160 mAh g^{-1} , like NCA, NMC, and LMS were introduced.^[22,26]

Besides the capacity of the cathode materials the voltages of the resulting cells is an important factor especially in industrial applications. The cell operating voltages depend on the redox potentials of the used anode and cathode materials. The energy levels and with that the redox potentials of the different cathode materials will be discussed in more detail later on.

Spinel-type cathode materials show very good lithium ion as well as electrical conductivity which enables a fast charging and discharging process. In terms of cyclability, they are limited due to the dissolution of Mn into the electrolyte which can poison the anode material as well. The dissolution of manganese can be reduced by introducing cobalt into the material (NMC). However, the elements nickel and cobalt are scarce materials with geographically limited availability. Especially in the field of electric vehicles, which will have the highest market share of LIBs in the near future, availability becomes more important with increasing demand. There are already trends reducing the amount of cobalt, which is the most critical element in high-performance LIBs e.g., going from NMC 111 towards NMC 811. The number behind NMC describes hereby the ratio of the elements nickel, manganese, and cobalt.

With the ever-growing need for LIBs and due to this expected lack of resources in the upcoming future, the prices of the raw materials are expected to rise.^[54] In addition to the development of new or improved recycling methods to enable reuse of the raw materials^[54], other materials gained more interest, which are based on nickel and manganese-free materials such as LFP. It belongs to the class of polyanion oxides which show a practical capacity of 140 mAh g^{-1} which is a rather low capacity and a lower operating voltage compared to, e.g. NMC^[55]. The lack of electron conductivity and a low

volumetric energy density can be compensated with very good characteristics in terms of fast charge, cycling, temperature runaway, and safety^[1,2,26]. In addition, LFP shows good thermal stability without oxygen release due to the tight hold of oxygen by the covalently bonded PO₄-groups. An overview of the different cathode materials and a comparison of their performances is depicted in **Figure 8**.

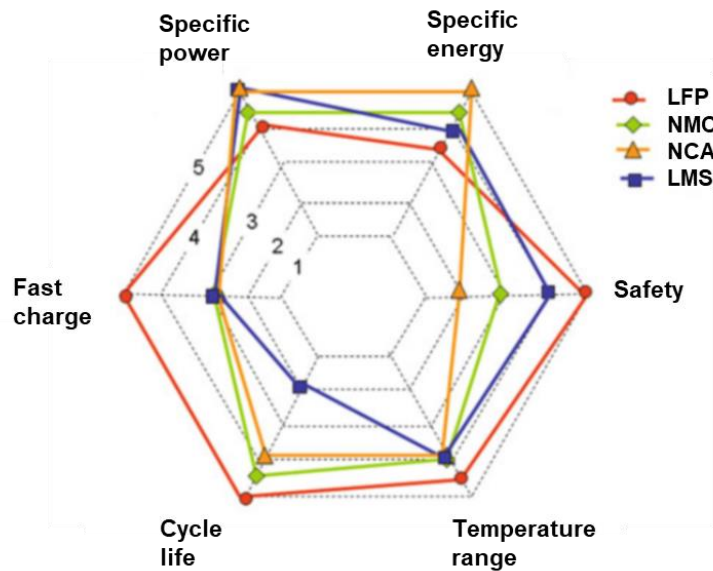


Figure 8: Comparison of the performance of various cathode materials used in LIBs. Reprinted with permission from ^[26].

The differences between cathode materials in their electrochemical properties and their performance determine the field of applications of the corresponding LIBs. NMC-based LIBs are used for high-capacity battery applications, while LFP-based batteries are considered where especially high-temperature stability, fast charging, safety as well as long cycle life come into play.

1.3.2 Anode materials for lithium ion batteries

An ideal active anode material should fulfill several requirements:^[26]

- lightweight, while accommodating as much lithium as possible to optimize the gravimetric capacity,
- the redox potential vs Li/Li⁺ must be as small as possible to optimize the energy density of the battery,
- a good electronic and ionic conductivity since the movement speed of the lithium ions correlates with the power density of the cell,
- the electrolyte material needs to be able to swell the active anode material
- the anode active material must not reaction with the lithium salt,
- high safety *i.e.*, avoid any thermal runaways of the battery,
- cheap and environmentally friendly.

Graphite-based materials are still the most common anode materials due to their good chemical, mechanical, and electrochemical properties:^[19] In combination with its low cost, graphite shines as the most suitable intercalating anode material for nowadays devices.^[19] Nevertheless, graphite-based electrodes suffer from different issues e.g., capacity fade or exfoliation due to the intercalation of solvents in the lattice^[10].

The aim for future LIB generations is the use of pure lithium metal as anode material.^[23,24] Lithium shows with -3.04 V vs the standard hydrogen electrode the lowest reduction potential of all metals and with 3860 mAh g⁻¹ an outstanding theoretical capacity^[23] which makes it the most promising anode material.^[24] However, the use of liquid components as electrolytes does not allow the use of elemental lithium due to the formation of dendrites.^[14,24] For this reason, common LIBs use graphite-based materials avoiding the issue of dendrite formation.

Graphite is a layered material based on numerous graphene layers. These layers show relatively weak interaction to on another. These weak interactions allow the intercalation of ionic or molecular species, in the case of LIBs the intercalation of the lithium ions. This results in an expansion of the graphite due to the increase of the interlayer distance and therefore decrease in the π - π interactions. This phenomenon is shown in **Figure 9**.

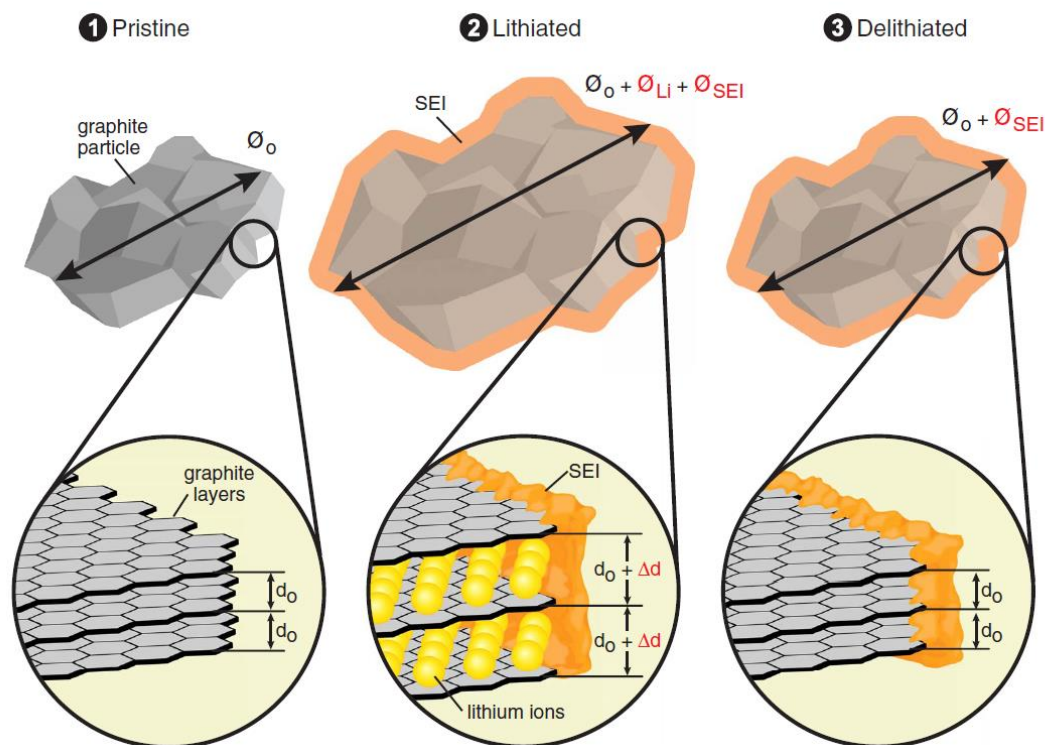


Figure 9: Schematic depiction mechanisms of reversible and irreversible deformation of graphite electrodes. Reprinted with permission from ^[56].

While the formation of the SEI leads to an irreversible deformation of the graphite electrode, the intercalation of the lithium ions leads to a reversible increase in the graphite layer spacing.

Graphite as intercalating anode material for LIBs was first reported in 1983 by Yazami and Touzian.^[57] The maximum theoretical specific capacity having a LiC_6 stoichiometry is 372 mAh g^{-1} .^[10,19,26] Stoichiometries with a higher lithium content are possible to achieve but the reversibility of the system is then no longer given.^[26]

Besides graphite-based anode materials, titanium dioxide is a low-cost, environmentally friendly, non-toxic alternative and is considered a promising candidate as an anode material. The theoretical capacity of 335 mAh g^{-1} , corresponding to the insertion of one lithium per mol of titanium dioxide, is comparable to graphite^[26,58]. Due to its good thermal stability and the formation of stable SEI titanium dioxide anodes are recommended for safety issues. However, its higher potential compared to graphite leads to less cell operating voltages. These low voltages result in a low energy density but leads to very high safety since lithium plating is no issue. This makes LTO interesting for high safety, low energy density applications.

Another upcoming anode material with high potential is silicon which is material with established supply chains and a specific capacity of 4200 mAh g^{-1} when lithiated to $\text{Li}_{4.4}\text{Si}$ is a very high value.^[59]

With a redox potential of 0.3-0.4 V vs Li/Li⁺ it averts the concern of lithium deposition^[26]. Since Si is a semiconductor already most of the before-mentioned requirements can be fulfilled. However, when using silicon materials the volume change upon cycling is a huge concern.^[26] During the charging/discharging process from Si to Li_{4.4}Si the volume expansion is 420%.^[60] This can lead to cracks in the material and therefore damage the whole cell.^[26] A damaged cell can leak liquid components like the electrolyte which then can lead to safety issues upon burning due to being highly flammable (for common liquid electrolytes).

1.3.3 Energy levels in lithium ion batteries

The energy levels of the anode, cathode, and electrolyte materials determine the performance of the battery cell. **Figure 10** shows the position of various redox couples relative to the top of the oxygen:2p band. (a). The relative schematic energy levels of anode, cathode, and electrolyte material in an open circuit are depicted in **Figure 10** (b).

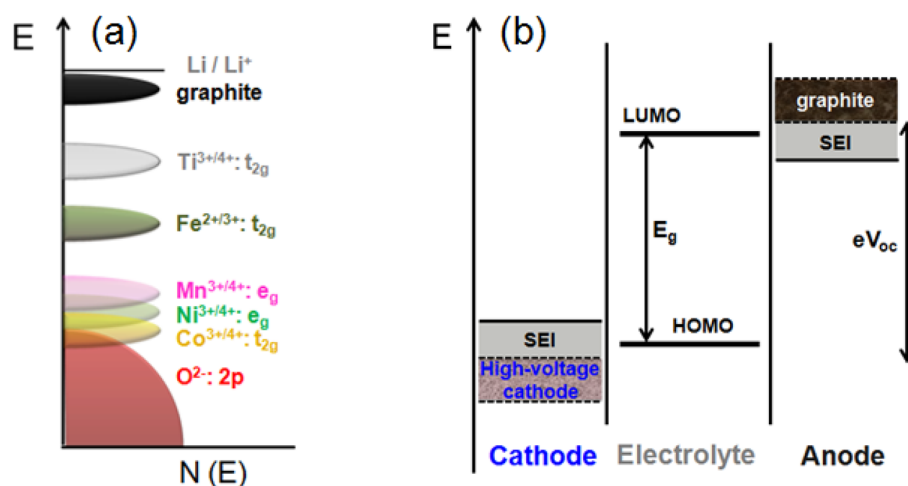


Figure 10: Positions of various redox couples relative to the top of the oxygen:2p band (a) and schematic energy levels (b) of anode, cathode, and electrolyte in an open circuit. Optimal SEI layers can widen the stability window as indicated in (b). Reprinted with permission from ^[1].

The chemical stability of different cathode materials can be explained by their relative redox potential (c.f. **Figure 10** (a)). For example, LiCoO₂ suffers from poor chemical stability due to an overlap of the Co^{3+/4+} band with the oxygen band resulting in a removal of electron density from the O²⁻ band. In contrast, Mn suffers from poor electron conductivity but shows improved chemical stability due to no overlap of the Mn^{3+/4+} with the O²⁻ band. Nickel shows electronic and chemical properties between Co and Mn. Considering the advantages and disadvantages of those elements the industry uses compositions of all three elements to realize the best possible among those (NMC)^[1]. **Figure 10** (b) shows the energy levels of the anode, cathode, and electrolyte material relative to each other. Graphite has dominated the anode materials for decades but shows a redox energy that is higher than

the LUMO of the electrolyte material. However, the formation of the SEI provides the stability necessary for the battery cell. Different anode materials e.g., LTO-based materials have a redox energy level below the HOMO of the electrolyte. That is the reason for no formation of an SEI and therefore improved cycle life compared to graphite-based materials.

A similar phenomenon occurs for cathode materials. Although the redox energy of most cathode materials is below the HOMO of the electrolyte, the formation of the SEI, for cathode materials often referred to as cathode electrolyte interphase (CEI) allows the usage of those materials due to the increased stability provided by the CEI.

1.3.4 Graphene

Graphene is one of the most promising two-dimensional carbon materials^[61] based on an aromatic carbon network with a honeycomb structure. It gained interest in electrochemical applications due to its outstanding mechanical, optical, thermal, and electronic properties.^[61–64] This allows graphene to play a role in various applications e.g., organic electronics^[65] like solar cells,^[63] supercapacitors,^[66] biomedical applications,^[67] as well as lithium ion batteries.^[68,69] Despite the huge interest in graphene as applicable material in many different fields, the production of large amounts of high-quality graphene still is a challenging task.^[62,69] The principle of the exfoliation of graphene is depicted in **Figure 11**.

There are several approaches for the synthesis of graphene. They can be divided into two different groups, the bottom-down strategies and the bottom-up strategies. As bottom down strategy mainly the exfoliation of graphene comes into play which is the most used technique to synthesize graphene on an industrial scale. There are different ways of exfoliation, mainly wet-chemical^[70] and mechanical^[71] routes are used.

As ascribed in **Figure 11** two different approaches can be done during the wet chemical route. One way is to use chemical agents to oxidize the graphene layers in the graphite. The oxidation process leads to a volume change resulting in a drift of the graphene layers apart from each other. This process weakens the adhesion forces between the layers enabling the separation of the single layers. The result of this oxidation process is oxidized graphene which has to be reduced afterward. The resulting graphene is known as reduced graphene oxide (rGO). The harsh conditions during this process lead to defects in the graphene layers. Besides wet chemical exfoliation, one other major process is mechanical exfoliation. Hereby, the graphite undergoes sonication as part of a dispersion of graphite in the corresponding solvent (e.g., NMP). The sonication leads to the separation of the graphene sheets. Since the sonication process also involves harsh conditions, the quality of the resulting graphene usually does not fulfill the highest standards. Therefore, the quality of the exfoliated graphene is not as high as with other techniques, which will be described later. However, the

exfoliation process is the only process up to now that could be established in the industry, capable of producing large amounts of graphene. There are many more exfoliation processes besides the ones mentioned before. However, most of them are based on the wet chemical or the mechanical exfoliation technique.

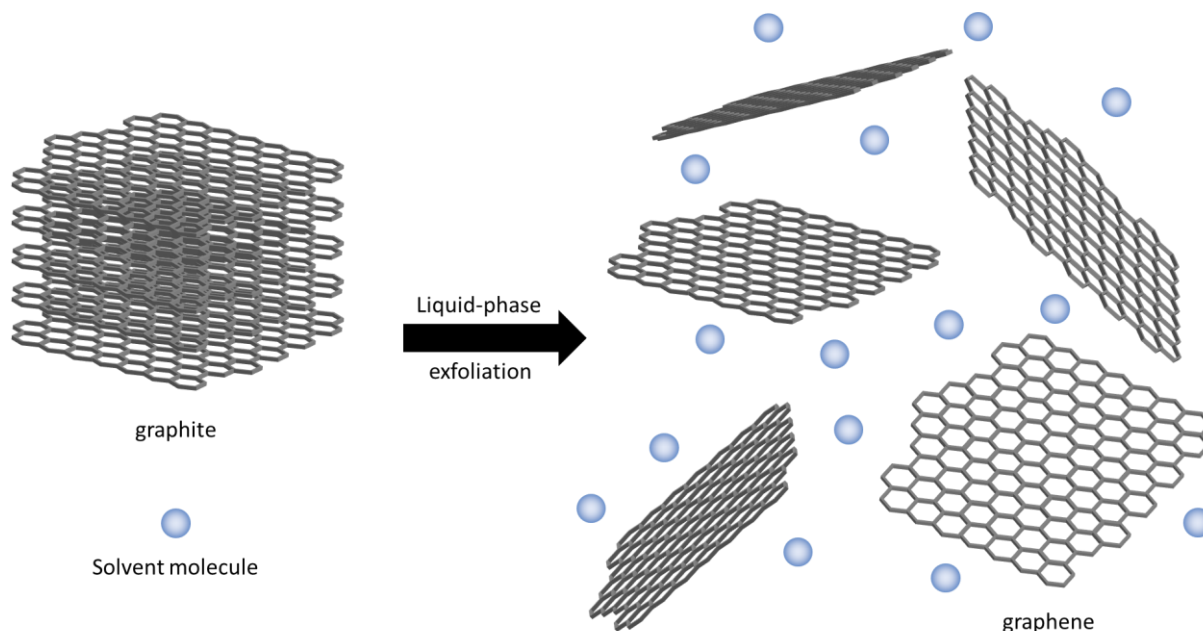


Figure 11: Liquid-phase exfoliation of graphite resulting in dispersed graphene sheets in the corresponding solvent. There are two different approaches: Either using chemical agents to oxidize the graphene, leading to a volume change, causing the graphene layers to drift apart; or sonicating the graphite in the solvent, leading to a weakening of the intramolecular interactions due to the diffusion of the solvent molecules between the graphene layer in the graphite and thus over time to the separation of the graphene layers. Graphene occurs in layer numbers from one to ten and usually shows plenty of defects due to the rather harsh exfoliation conditions.

Besides the exfoliation of graphene, several different possibilities to synthesize graphene were investigated. Most of them are based on bottom-up approaches where graphene gets synthesized using smaller precursors which then add up building graphene layers. There are techniques e.g., coating carbon sources in terms of polymers like PMMA^[85] or aromatic precursors^[72] on catalytic metal like copper, enabling upon heating the separation to hydrogen and carbon to form graphene from the built carbon while the hydrogen evaporates. A different approach starts from silicon carbide single crystals where upon heating silicon evaporates and carbon remains, forming graphene layers on the surface.^[73] This highly sensitive process results in high-quality graphene. However, due to the complicated setup and processing the amount of graphene producible with this technique is limited. Since the before-mentioned techniques were not used in this work there will not be a more detailed process description.

One interesting technique, allowing the preparation of high-quality graphene with industrial interest due to roll-to-roll process possibilities is the chemical vapor deposition (CVD) technique.

CVD describes a process where typically gaseous carbohydrate precursors undergo pyrolysis forming elemental carbon and hydrogen. This process requires high temperatures as well as a catalyst. As a combination of both, a heated foil of a catalytically active material is typically used. Common examples of catalyst materials are nickel or copper metal. While the elemental hydrogen vanishes in the atmosphere of the CVD chamber, carbon remains on the catalyst. Upon nucleation and reorganization of the carbon atoms graphene can be formed. The main principle of the CVD process is depicted in **Figure 12**.

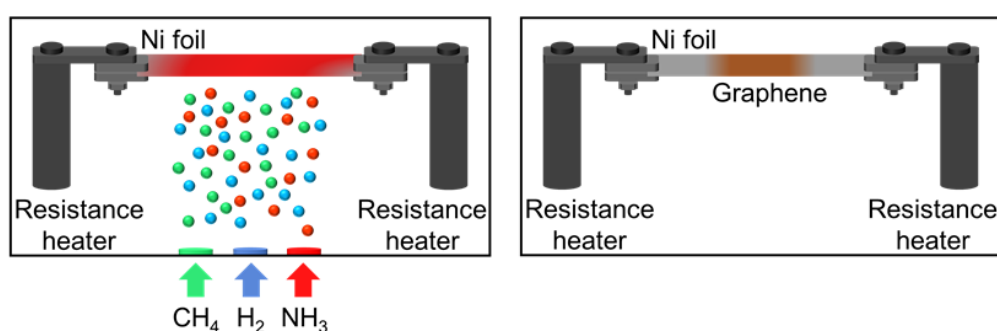


Figure 12: Typical setup for chemical vapor deposition synthesis of graphene. The catalyst foil (here nickel) is heated up resistively. Hydrogen is used on the one hand to reduce the catalyst surface to ensure a highly active area in the surface, and on the other hand, it is used as a co-catalyst. Here methane is used as a carbon source, which will be necessary for the formation of graphene sheets. The addition of ammonia is an option to be able to dope the graphene in-situ.

Raw materials which are used for the synthesis of graphene *via* CVD can be classified as two kinds of materials: precursors and assistant gases.^[61] Organic precursors often are methane, ethane, propane, or other hydrocarbons which are in gaseous state^[74]. Since the dehydrogenation energy differs, using different carbon sources leads to the necessity of using different temperatures depending on the material. During the CVD process, often an assistant gas is used. Common assistant gases are hydrogen, argon, or a combination of both. Hydrogen can activate as well as etch the surface of the catalytic foil, controlling the morphology and size of the final graphene domains.^[61] Argon gas is used to ensure an inert atmosphere which is critical at such high temperatures as used during the CVD process. Additionally, argon can be used as a carrier gas, controlling the amount of carbon material on the catalyst surface. These effects can also be influenced by the ratio of hydrogen and argon.^[75]

As catalytic materials metals are used that are capable of splitting the hydrogen from the carbon of the hydrocarbons. Different metals used for CVD synthesis of graphene are shown in **Table 1** depending on their carbon solubility.

Table 1: Reported values of the carbon solubility and melting point of some metals used for CVD graphene synthesis^[76].

METAL	CARBON SOLUBILITY [ATOMIC PPM]	MELTING POINT [°C]
NI	9.000 (900°C)	1455
CU	7,4 (1020°C)	1085
CO	10.000 (1000°C)	1495
PT	11.000 (1000°C)	1768
PD	33.000 (1000°C)	1555
MO	700 (1500°C)	2623
GE	<1000	938
RU	2.300 (900°C)	2334

As mentioned before, nickel and copper are typically used for the CVD synthesis of graphene. However, they show very different carbon solubilities. Nickel offers a very high but copper shows a very low carbon solubility, their difference leads to a different mechanism of graphene growth. The graphene growth mechanism using nickel and copper is depicted in **Figure 13**.

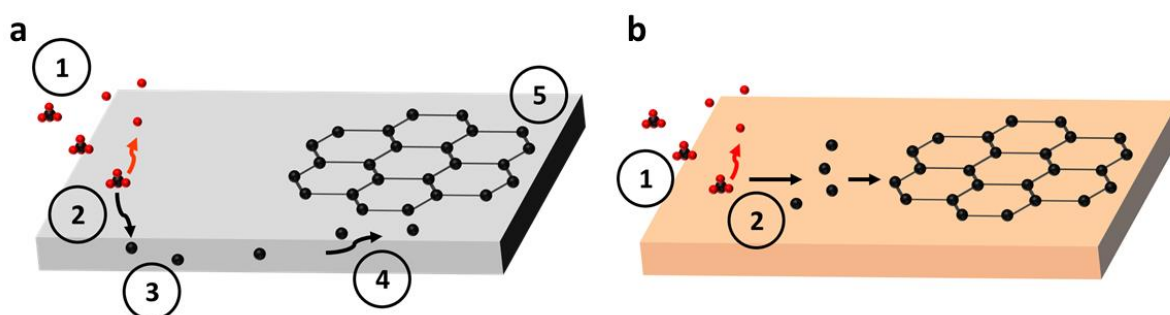


Figure 13: Comparison of the mechanism using nickel (a) or copper (b) as catalysts. The mechanisms differ due to different abilities to dissolve carbon inside the metal film. (a) shows a five-step mechanism *via* starting materials like methane (**1**), the decomposition thereof on the nickel surface, at elevated temperatures, into carbon and hydrogen atoms (**2**). Here the carbon atoms dissolve in the nickel until decreasing the temperature, then the carbon atoms diffuse to the surface (**3,4**). The diffusion of the carbon atoms to the surface yields graphene on the nickel surface (**5**). In comparison to nickel, the formation of graphene using copper as catalyst (b) takes two steps to the final graphene sheets. After the arrival of the starting materials (**1**), the materials decompose on the surface and build carbon atoms (**2**) which afterward migrate on the surface until upon cooling down when they form graphene sheets. Picture adapted with permission from ^[77].

As soon as methane reaches the hot Ni surface (a), it chemisorbs to the surface and carbon and hydrogen become catalytically dissociated (1,2).^[77,78] Both the carbon and the hydrogen atoms can contribute to the reduction of residual nickel oxide to elemental nickel. The period of the nickel oxide reduction depends on the treatment of the nickel foil and the purity of the nickel surface, before

starting to add the carbon source. The dissociation process needs a minimum temperature of 400 °C to start.^[77] Due to the high carbon solubility of nickel, the dissociated carbon atoms diffuse into the bulk metal.^[78] Upon cooling, when the threshold for nucleation is reached and the solubility of nickel is decreased due to decreased temperature, the carbon atoms diffuse back to the surface of the metal (4). Once the carbon atoms reach the metal surface, the segregation process and the graphene growth start (5). The segregation process stops once the number of carbon atoms which are able to dissolve in the metal reaches its equilibrium depending on the temperature.

In the case of using copper, the mechanism of the graphene growth differs, already indicated by the difference in carbon solubility comparing nickel and copper. The chemisorption of the carbon source to the copper surface and the dissociation of carbon and hydrogen atoms would automatically start the growth of graphene. However, the graphene stops immediately as soon as providing carbon sources stops. To ensure a sufficient amount of carbon source, copper does already get exposed to the carbon source at room temperature. Using copper as a catalyst, the temperature is very critical to achieve high-quality graphene. Starting from room temperature, a sequential temperature profile is used to heat to the appropriate temperature to start the decomposition of the carbon source.

Graphene synthesized *via* CVD results in the highest quality compared to the exfoliation methods described before. However, the CVD process itself is highly complex.

After the synthesis, the quality of the graphene sheets needs to be determined. Here, the Raman spectroscopy serves as the main tool. Ferrari *et al.* specialized in the characterization of graphene *via* Raman spectroscopy.^[79,80] The differences between a high-quality graphene and graphene with defects can be detected *via* Raman spectroscopy as shown in **Figure 14**.

High-quality graphene (**Figure 14**, top) differs from defective graphene (**Figure 14**, bottom) with the number and intensity of peaks depicted in the Raman spectrum. Characteristic peaks arise either due to different electron dispersions or phonon scattering in the material.^[79] The main characteristic peaks of high-quality graphene are at roughly 2700 cm⁻¹ (2D) and 1650 cm⁻¹ (G), respectively. In defective graphene, the D peak at about 1500 cm⁻¹ and its overtones D' and D'' arise. The more holes or edges are inside the graphene, the higher the intensity of the D peak. In addition to the quality of the graphene, the number of layers can be determined by Raman spectroscopy. The ratio of the intensities of the 2D and G peaks can be used to calculate the number of graphene layers according to the following equation.

$$I_{G/2D} = 0.14 + \frac{n}{10} \quad (1)$$

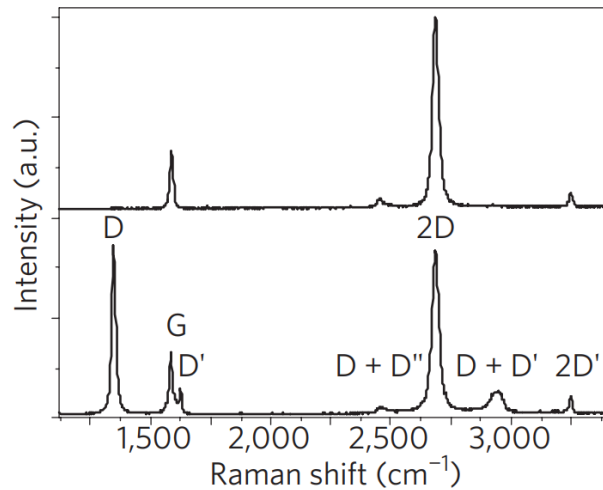


Figure 14: Comparison of the Raman spectra of defect-free single-layer graphene (upper spectrum) with defective graphene (lower). The defect-free graphene shows mainly two peaks, namely the G and the 2D peak. Their ratio indicates the quality of the graphene and tells the number of layers (cf. equation 1). The higher the 2D/G ratio is, the higher the quality of the graphene. Mainly the arising of the D peak, along with its overtones, indicates defects in the graphene layer. Reprinted with permission from [79].

Besides the ratio of the intensities, the shape of the 2D peak can help to interpret the number of graphene layers. The evolution of shape with an increasing number of layers is shown in **Figure 15**.

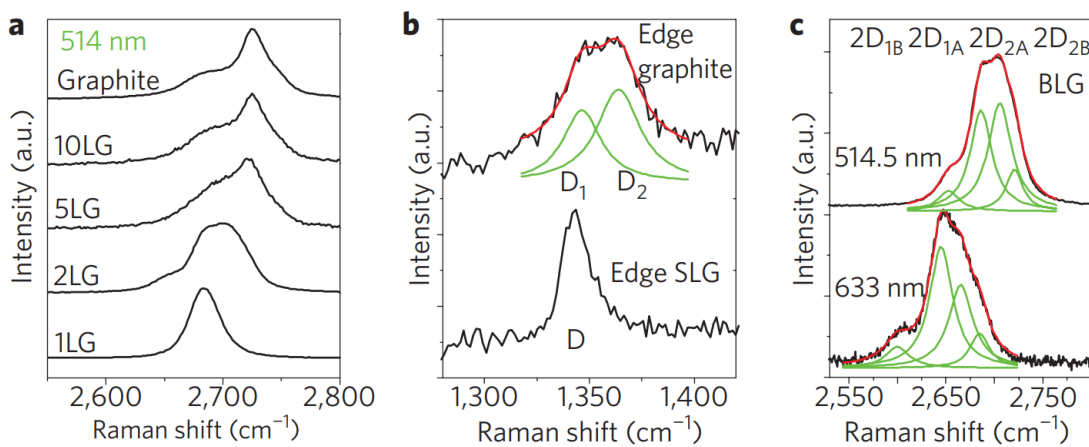


Figure 15: Dependencies of the Raman spectra in correspondence to the number of graphene layers. The symmetry of the 2D peak shows a strong dependence on the number of layers (a). Single-layer graphene has a symmetric 2D while with increasing layers the symmetry gets lost due to the appearance of overtones shown in (c). Reprinted with permission from [79].

The number of graphene layers in correspondence with the difference in shape is depicted in **Figure 15** (a). With an increasing number of layers, more symmetry of the peak is lost and the overlay of different peaks becomes more visible. The interaction of one layer with a different number of other layers leads to a different electron dispersion throughout the material. As mentioned before, Raman spectroscopy is sensitive toward differences in electron dispersions, therefore there are more tones

of the 2D peak visible with an increasing number of layers. Not only the number of layers affects the shape of the 2D peak but also the laser used for the spectroscopy. Different lasers with different wavelengths of incoming light lead to a difference in the shape of the peaks, as shown in **Figure 15** (c). Therefore, during one study the laser source of the Raman spectroscope should not be changed.

The D peak, arising due to defects or due to a higher amount of edges, respectively, changes its shape from single-layer graphene (SLG) to multi-layer graphene or graphite, **Figure 15** (b).

These studies by Ferrari *et al.* show how sensitive Raman spectroscopy is and how much information can be gathered to determine the quality of graphene from one spectroscopy method.

1.4 Characterization of lithium ion batteries

1.4.1 Electrochemical impedance spectroscopy (PEIS)

Electrochemical impedance spectroscopy (EIS) can be applied to measure the ionic conductivity of a system. EIS can be measured either galvanostatically or potentiostatically. During an impedance spectroscopy measurement, an alternating current (galvanostatic) or an alternating voltage (potentiostatic) is applied while measuring the respective voltage or current response over a frequency range. Since in this thesis, only potentiostatic electrochemical impedance spectroscopy (PEIS) was used, only PEIS will be discussed in this chapter. The applied alternating voltage can be described as the following:

$$V = |V| \sin(\omega t) \quad (2)$$

Here ω is the angular frequency ($\omega = 2\pi f$), f being the frequency, and t the time. Due to this applied alternating voltage, the material responds with an alternating current which can be described as:

$$I = |I| \sin(\omega t + \theta) \quad (3)$$

Here θ is the phase shift due to reactance (e.g., capacitance, inductance) in the material. Extending Ohm's law (resistance as ratio of amplitudes in a direct current circuit), the impedance in an alternating circuit can be calculated the following:

$$Z = \frac{V}{I} = \frac{|V| \sin(\omega t)}{|I| \sin(\omega t + \theta)} = |Z| \frac{\sin(\omega t)}{\sin(\omega t + \theta)} = |Z| e^{i\theta} \quad (4)$$

Using Euler's formula ($e^{ix} = \cos(x) + i \cdot \sin(x)$), this term can be divided into its real and its imaginary parts. The Impedance can then be described as:

$$Z = Z' + iZ'' \quad (5)$$

Z' is the real or "resistive" part while iZ'' is the imaginary "reactive" part.

The most common way to plot the impedance is the Nyquist plot. Here, the imaginary impedance is plotted vs. the real impedance, with one data point per tested frequency. An example of a Nyquist plot is depicted in **Figure 16**.

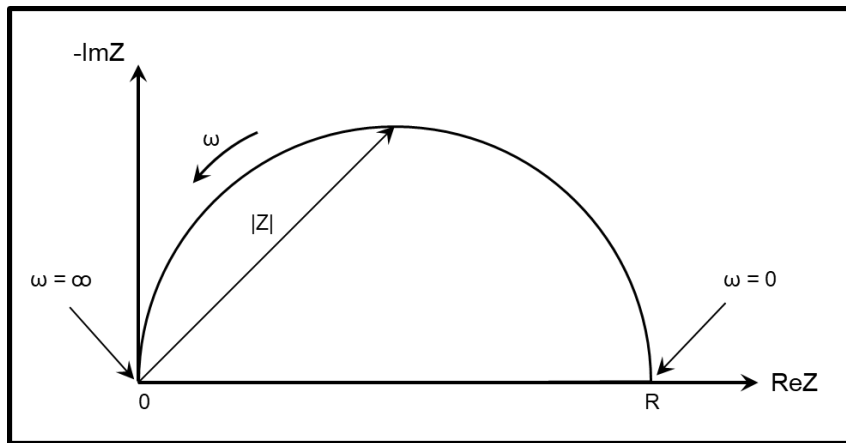


Figure 16: Nyquist plot of an EIS. The real impedance is plotted vs. the imaginary impedance. The Nyquist plot often shows a semicircle. This shape of the impedance spectroscopy measurement can be modeled with a simple equivalent circuit.

Nyquist plots obtained from EIS measurements of electrochemical systems are often similar to one or several semicircles. To extract quantitative values of interest, mathematical fitting can be used which becomes increasingly complex, especially for overlapping semicircles or additional patterns. Alternatively, an equivalent circuit of electrical components can be used to model the system and simulate the resulting plot. The shape of the Nyquist plot highly depends on the equivalent circuit elements used to model the battery setup. The most basic equivalent circuit model is shown in **Figure 17**.

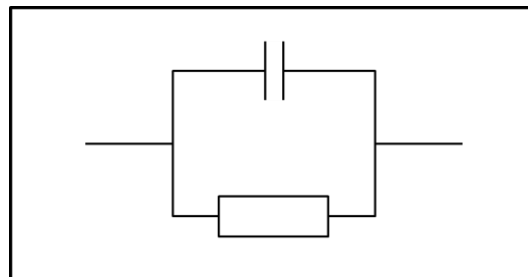


Figure 17: Basic equivalent circuit model used for PEIS.

The parallel setup of a capacitor and a resistor can be used as a basic model of a LIB. The resistor reflects the common resistance of the charges moving through the investigated system. The capacitor reflects e.g., grain boundaries and interfaces in the investigated system. In a battery setup, the interface from the electrolyte towards the cathode or anode can be explained *via* a capacitor setup. Since the before-explained setup is sufficient for the matter of measuring the ionic conductivity of an electrolyte in the system, impedance spectroscopy will not be explained in more detail.

During a PEIS measurement, an alternating voltage with different frequencies is applied to the system while measuring the current response of the system. The current response can be explained according to the used circuit model. At high frequencies there is not enough time to charge the capacitor, resulting in a very low resistance compared to the resistor in parallel. Thus, all the charges go through the capacitor and neglect the resistance ($\omega \rightarrow \infty$; $Z \rightarrow 0$). At low frequencies the capacitor is charged and “blocks” any charges going through the capacitor, thus all the charges will move through the resistor ($\omega \rightarrow 0$; $Z \rightarrow \infty$). In between the two extremes, both the resistance of the materials as well as the interaction of interfaces come into play resulting in the semi-circle observed in the Nyquist plot. The Nyquist plot can then be used to calculate the measure of the impedance of the investigated system using the minima of the semicircle at low frequencies since only the resistance or impedance comes into play.

1.5.2 Cyclic voltammetry (CV)

Cyclic voltammetry (CV) is a very fast and therefore common method to investigate the electrochemical behavior of a material. This technique directly visualizes rather complex redox behaviors in a material. During a CV measurement, a potential is applied and changed back and forth over a specific voltage range, while measuring the current response of the material. The potential is applied between the working electrode and the counter electrode to investigate the material in between the electrodes in terms of its electrochemical behavior. To ensure a sufficient and meaningful result, the scan rate [mV/s] needs to be small enough to allow the material to react to the applied potential. A characteristic cyclic voltammogram is depicted in **Figure 18**.

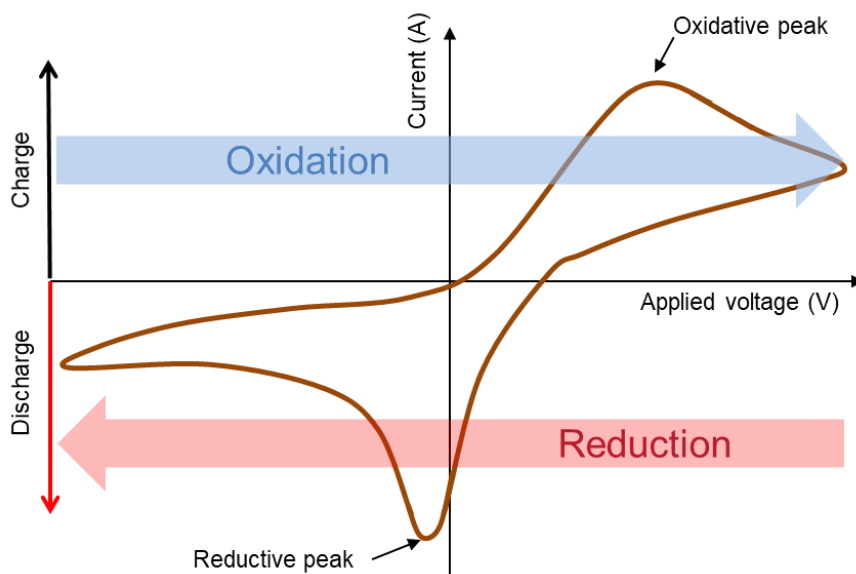


Figure 18: A schematic diagram of a cyclic voltammogram highlighting the characteristic oxidative and reductive peaks. The oxidation process can be investigated applying a positive current (charge), the reductive process can be investigated applying a negative current (discharge).

The current response of the material allows the recording of oxidative or reductive behavior of the material depending on the algebraic sign of the current. Oxidation processes can be investigated applying a positive current, reductive process applying a negative current respectively.

1.5.3 Galvanostatic cycling with potential limits (GCPL)

The capacity of a LIB can be measured using galvanostatic cycling with potential limits (GCPL). During GCPL, a constant current is applied to the battery measuring from lower potential limit to high potential limit (charge) and *vice versa* in the discharge direction. The selected potential limits avoid damaging the battery by avoiding side reactions that can be caused by too high or too low potentials. A typical charge/discharge profile of an LFP battery using a C-rate of 1/10 is shown in **Figure 19**. A C-Rate of 1 is defined as the current that is needed to fully charge a LIB in one hour (1C).

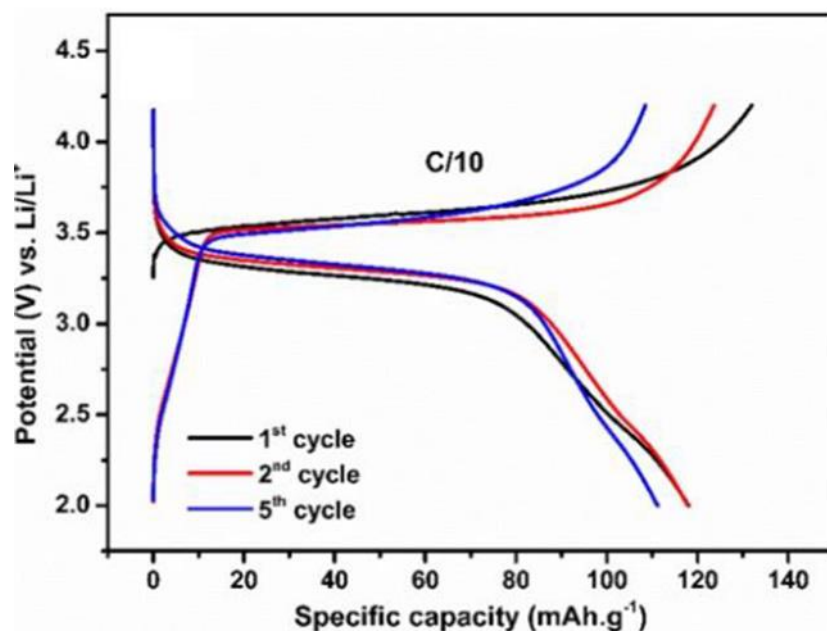


Figure 19: Typical galvanostatic charge/discharge profile of LiFePO_4 at a C-rate of 1/10 within a potential range of 2.0-4.2 V vs Li/Li^+ . Picture was reprinted with permission from ^[81].

The capacity of the battery is depending on the C-rate of the measurement, the smaller the C-rate the higher the measured capacity. With an increasing number of cycles, the capacity of the battery should be stable which is indicating that no side reactions occur. Due to e.g., SEI formation a decrease in the capacity is a typical behavior in LIBs. The course of the graph of the potential vs the capacity of the LIB is characteristic for the used electrode materials. For example, for LFP based LIBs the curve has a smaller slope as e.g. a NMC-based LIB. Another characteristic based on the electrode materials is the maximum potential of the LIB. According to chapter 1.4.1 the potential is lower for LFP cells compared to NMC cells, having a nominal voltage of 3.2V and 3.66V, respectively. The difference in the nominal voltage can impact the applications the LIBs are used for.

1.5 (AB)_n segmented copolymers

(AB)_n segmented copolymers are a very versatile class of polymers due to the ability to tailor the copolymers toward desired properties. Multiblock copolymers often are synthesized *via* living anionic polymerization^[82,83] or controlled radical polymerization.^[84] In contrast, (AB)_n segmented copolymers were synthesized *via* polycondensation reaction using telechelic oligomers and polymers.^[85,86] These copolymers were typically synthesized in a solution-based polycondensation reaction. Melt-polycondensation synthesis of (AB)_n segmented copolymers offers the benefit of reduced purification steps and the potential of a one-pot synthesis.^[87,88] Different reaction mechanisms, monomers, and reaction conditions open up a wide variety of (AB)_n segmented copolymers e.g., alternating-linear,^[89] spherical,^[84] star-shaped,^[82,84] or microphase-separated copolymers.^[90] The variety of (AB)_n segmented copolymers allows them to be used in various applications such as melt-electro-writing,^[86] melt extrusion-based additive manufacturing,^[85,88] and shape memory hydrogels.^[91] An example for (AB)_n segmented copolymers processable *via* melt electrowriting based on hard segments (urea) and soft segments (PDMS) is shown in **Figure 20**.

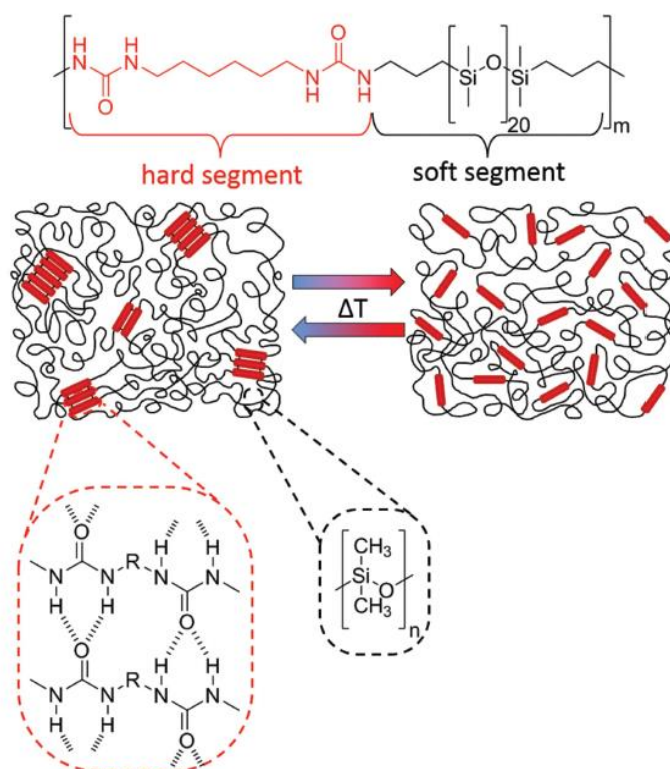


Figure 20: Sketch of the thermal reversibility of a thermoplastic elastomer represented by hard segments (urea) and soft segments (PDMS). Picture was reprinted with permission from.^[86]

In this case the (AB)_n segmented copolymer consists of a rigid segment, the urea segment, and a more soft segment, the PDMS segment. The physical crosslinks arise from the formation of hydrogen bonds

of the urea segments which was shown to be reversible by adapting the temperature. This reversibility of the hydrogen bond formation allows the processing with melt processing techniques e.g. melt electrowriting.

In the view of battery applications Mecerreyes^[92] *et. al* published polyimide-polyether copolymers based on *pyromellitic* as well as *naphthalene polyimides*. These polyimide-polyether copolymers were used in cathode materials for lithium metal batteries. Therefore a slurry using acetonitrile as solvent to enable the preparation of cathode material films *via* doctor blading.

Another class of (AB)_n segmented copolymers are based on *perylene segments* as hard segment and PPO-PEO-PPO segments as soft segments. Such (AB)_n segmented copolymers are in focus of this thesis. Here, the perylene segment ensures mechanical stability and the polyether segment chain flexibility. The former arises from the π - π stacking of the perylene units which leads to a physically crosslinked network.

The π - π -stacking of perylene imide is a well-known phenomenon which was investigated in more detail.^[93] UV/Vis studies show the absorption in dependence on the concentration (c.f. **Figure 21**).

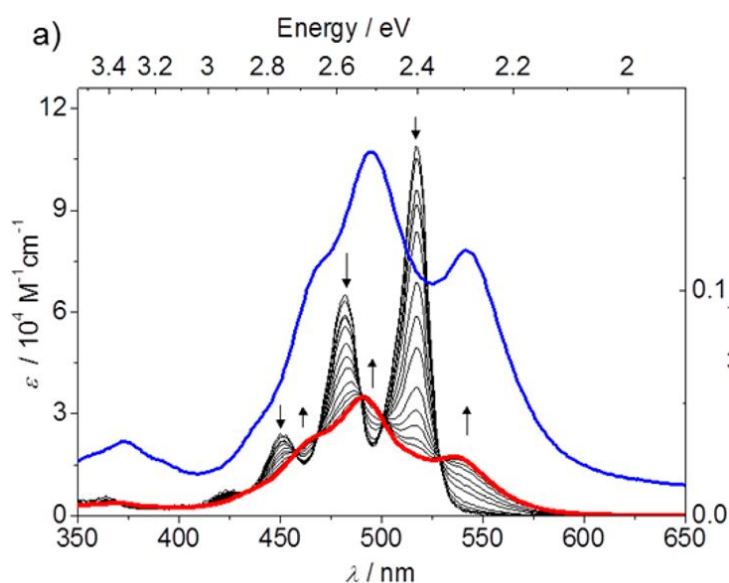


Figure 21: Concentration-dependent UV/Vis absorption spectra of perylene imides. Arrows indicate changes with increasing concentration, starting with the lowest concentration of 2×10^{-7} (red). The blue line shows spin-coated film after annealing, indicating a fully aggregated perylene imide system. Reprinted with permission from ^[93].

The spectra were recorded in methylcyclohexane solution. Upon increasing concentration, hypsochromic shift and broadening of the absorption bands can be observed. The change results from the stacking of the perylene units.^[93] A similar effect can be observed investigating the solvent-dependent absorption of perylene units as shown in **Figure 22**.

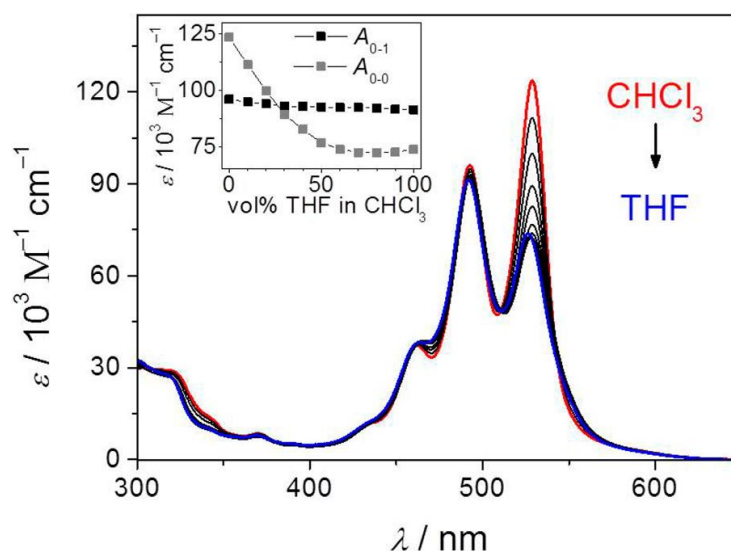


Figure 22: Solvent-dependent UV/Vis absorption spectra of perylene imides. Changing from pure CHCl_3 (red, not aggregated) to pure THF (blue, aggregated). Reprinted with permission from ^[93].

CHCl_3 is a better solvent for perylene imides. Therefore, the perylene units occur as non-aggregated units. Upon increasing the THF content the solubility of the perylene decreases and therefore initiates the stacking of the perylene units. The stacking induces a change in absorption and induces a slight hypsochromic shift in the spectra.^[93] The correlation between the absorption of the perylene units and their stacking makes UV/Vis studies a suitable technique to investigate the stacking behavior of perylene-based materials.

During the course of this thesis, Mecerreyes *et al.*^[94] demonstrated the synthesis of perylene polyimide-PEO copolymers for the use as binder material in an anode for organic polymer *sodium ion batteries*. This $(\text{AB})_n$ segmented copolymer was used as electrode material for an all-organic aqueous *sodium-ion based battery*^[94] and consists of perylene and polyether (Jeffamine) segments. The synthesis was carried out in a *solvent-based approach* using NMP as corresponding solvent. A schematic structure is shown in **Figure 23**.

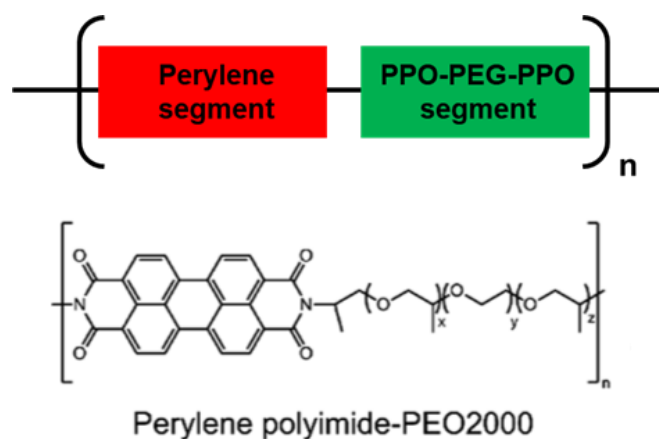


Figure 23: $(AB)_n$ segmented copolymer based on perylene dianhydride and Jeffamine ED-2003 using NMP as solvent. Reprinted with permission from ^[94].

In contrast to Mecerreyes *et al.* this thesis focusses on the synthesis of $(AB)_n$ segmented copolymers based on a *solvent-free* synthesis. This opens the way to use such copolymers as *matrix material for solid electrolytes* as well as *binder material for electrode materials in lithium ion batteries*. In addition Mecerreyes *et. al* did not consider the endgroups of the polymers which may contain protic groups. To achieve an usability in lithium ion battery applications an aprotic system is required. Therefore, the synthetic work in this thesis combines the synthesis of $(AB)_n$ segmented copolymers for *lithium ion batteries* by designing completely aprotic material *via* the incorporation of suitable endgroups.

2. Aim and Motivation of the thesis

Nowadays commercially available lithium ion batteries are based on solid electrodes and liquid electrolytes. The liquid electrolyte poses the risk of a short circuit due to the formation of lithium dendrites. Therefore, solvent-free solid-state lithium ion batteries are currently intensively investigated in order to avoid dendrite formation and should result in safer lithium ion batteries.

In this context the thesis addresses four main aims which are illustrated in **Figure 24**. The overall aim is the synthesis of suitable polymers with the purpose to serve as *matrix material for solid-state electrolytes and as binder materials* tailored for the use in *lithium ion batteries*.

Therefore, the $(AB)_n$ segmented copolymers composed of perylene segments and polyether segments should be synthesized and tailored towards their thermal, mechanical, and morphological requirements. Here, a melt-polycondensation should be developed to avoid the use of solvents and to be more sustainable. The second aim is the preparation and characterization of solvent-free lithium ion battery electrolyte materials by incorporating lithium salts into suitable $(AB)_n$ segmented copolymers. The third aim is the preparation and characterization of a melt-processable cathode material based on the $(AB)_n$ segmented copolymers as binder material for cathode active materials and electron conducting materials. The fourth aim is the novel processing of a fully melt-processed solvent-free solid-state lithium ion batteries and the characterization of their functionality.

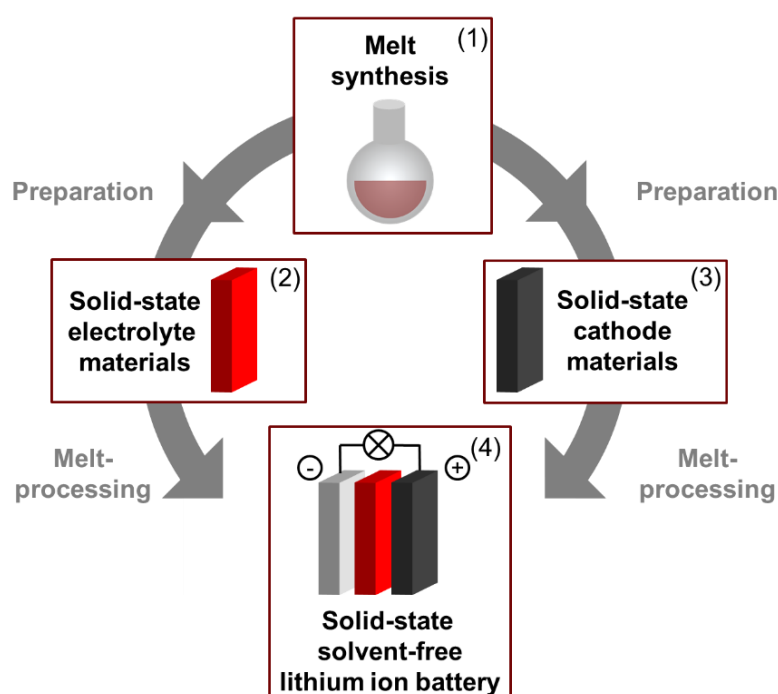


Figure 24: Schematic overview of the four parts of this work. Starting with the aimed bulk synthesis of $(AB)_n$ segmented copolymers (1), the thin film processing of yielded thermoplastic elastomeric polymer material used for solid-state electrolyte materials (2) as well as newly developed cathode materials (3). The combination of these materials should result in a newly developed solid-state solvent-free lithium ion battery (4).

Synthesis of $(AB)_n$ segmented copolymers

At first, a polymer suitable for the use as matrix and binder material in electrolyte and electrode materials in lithium ion batteries is planned to be synthesized which shall allow melt processing while fulfilling the before-mentioned requirements. To ensure melt processing it is planned to use a physically crosslinked network allowing a thermally induced reversible crosslinking providing a thermoplastic behavior necessary for melt processing. In this regard, one class of $(AB)_n$ segmented copolymers consisting of perylene segments and Jeffamine® segments, which can be described as poly ethylene glycol derivatives flanked by a few PPO-diamine units on each side, are planned to be synthesized in a solvent-free melt polycondensation reaction. The resulting polymers should be investigated for their thermal and mechanical properties. The Jeffamine® segments should hereby ensure ionic conductivity, as it is known for PEO-based systems, while the mechanical stability should arise from the π - π interactions of the stacked perylene segments. At elevated temperatures, the stacking should disassemble to ensure melt processing (see **Figure 25**). Investigations on the reversible physical crosslinking via π - π stacking of the perylene unit containing copolymers should identify the optimal polymer composition and corresponding optimal melt processing temperature.

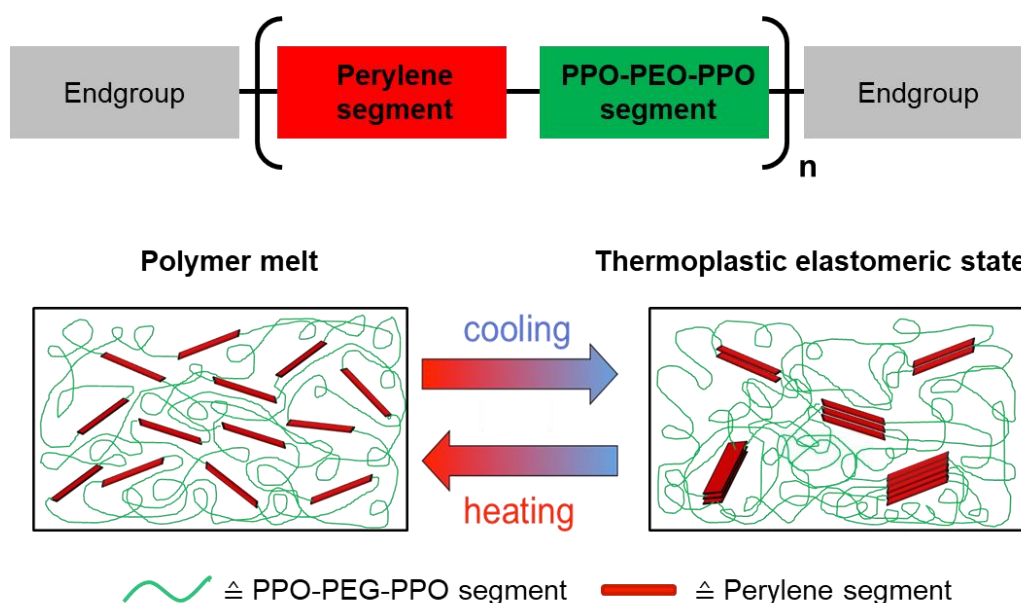


Figure 25: Schematic procedure of the planned $(AB)_n$ segmented copolymers. Upon cooling the thermo-reversible physical crosslinking of the perylene segments should result in an thermoplastic, elastomeric material. Upon heating above the disaggregation temperature of the perylene segments, the $(AB)_n$ segmented copolymer is planned to deaggregate allowing melt-processing.

Solvent-free solid-state electrolyte materials for lithium ion batteries

State of the art lithium ion batteries use low molecular weight materials like ethylene carbonate and/or propylene carbonate as electrolyte materials due to their high ionic conductivity as well as their electrochemical and thermal stability. Due to the lack of mechanical stability liquid electrolyte materials allow the formation of Li-dendrites which leads to serious safety issues in case of a short circuit. The second part of this work should address this by investigating solvent-free solid-state materials as electrolyte. In this context (AB)_n segmented copolymers should be focused as promising candidates as matrix material due to their PPO-PEG-PPO segments which ensure the ionic conductivity, necessary for the use in lithium ion batteries, while the π - π interactions of perylene segments contribute the mechanical stability to that typically applied thin layer. For their usage as electrolyte material in lithium ion batteries sufficient ionic conductivity, as well as sufficient electrochemical stability, is crucial. Therefore, a lithium salt e.g. LiTFSI is planned to be added to the (AB)_n segmented copolymers by mixing. Knowing that LiTFSI is highly hygroscopic, the planned processing at elevated temperatures as well as a suitable transfer towards an inert environment should avoid water absorption of the electrolyte material mixture. Nevertheless, LiTFSI is the most used lithium salt in research while LiPF₆ showed to be used in most commercial applications due to its improved electrochemical stability. The resulting polymer/salt mixtures are planned to be investigated towards their melt processability as well as their ionic conductivity and their mechanical and electrochemical stability.

Solid-state cathode materials for lithium ion batteries

In the third part solid-state cathode materials are planned to be prepared via melt processing without the use of solvents. Cathode materials consist of an active material, often lithium metal oxides, an electron conducting material, usually carbon black or graphene, as well as a binder material e.g. PVDF to ensure the homogeneity of the system.

For this purpose, high-quality graphene is planned to be synthesized via chemical vapor deposition and to be analyzed via Raman spectroscopy to verify the quality of the resulting graphene. Graphene flakes should then be used as an additive to increase the electronic conductivity in the cathode material. As cathode active material lithium iron phosphate is planned to be used, featuring similar properties comparable to most commercially used lithium cobalt oxide while being much less expensive. Instead of PVDF, (AB)_n segmented copolymers are planned to be used as the binder material in this work. The resulting cathode material, a mixture of lithium iron phosphate, graphene, and (AB)_n segmented copolymer, should be investigated on melt processability and prepared films should be analyzed towards their electrochemical properties.

Fabrication of solvent-free solid-state lithium ion batteries

The final chapter aims to develop a preparation route for a working lithium ion battery produced via melt-processing techniques. Interesting processing techniques for the layer preparation of the electrolyte as well as the cathode are compression molding as well as extrusion-based 3D printing which are planned to be investigated.

The final full battery setup is planned the following: firstly, a carbon-coated aluminum foil, secondly the cathode material, which should be a blend of lithium iron phosphate, $(AB)_n$ segmented copolymer and graphene, followed by the electrolyte material, which should be a blend of an $(AB)_n$ segmented copolymer and LiTFSI and lastly on top lithium metal as anode material. The obtained sandwich should be finally transferred and encapsulated into a coin cell setup to characterize the battery in terms of capacity and cyclability.

3. Results and Discussion

3.1 (AB)_n segmented copolymers

3.1.1 Synthesis of (AB)_n segmented copolymers

The aim of this chapter is to synthesize a copolymer suitable for use as matrix respectively binder material in electrolyte and electrode materials for lithium ion battery applications. For usage in lithium ion batteries, the polymer has to fulfill several requirements such as an aprotic and polar nature as well as an amorphous behavior. When a protic material is used, side reactions occur, leading to safety issues. The polymer must be polar to dissolve the lithium salt necessary for lithium ion conductivity. It also should be amorphous to enable consistent lithium ion transport. The presence of crystals in the polymer could foster the trapping of the lithium ions and therefore decrease the lithium ion conductivity. In addition to the afore-mentioned criteria, the polymer has to show sufficient thermal, mechanical, and electrochemical stability. For lithium ion battery applications, the electrolyte must be mechanically stable to avoid the formation of lithium dendrites. The mechanical stability must be provided up to a temperature of approx. 80 °C, which is the highest operating temperature of the battery. Often solvents, used during synthesis or processing, remain in the final material. Those can also cause safety issues by being flammable or volatile and thus could damage the cell. Therefore, solvent-free synthesis and processing are favored to avoid any complications. Besides thermal and mechanical requirements the polymer has to be electrochemically stable, to avoid side reactions in the battery which could lead to a decrease in performance and operating lifetime.

The most common polymer electrolytes, and therefore suitable as lithium ion conducting materials, are based on poly ethylene glycol (PEG). PEG is an aprotic, polar polymer that enables the dissolution of a lithium salt necessary for lithium ion conduction. However, pure high molecular weight PEG is crystalline. The crystallinity is reduced by adding a lithium salt e.g. lithium bis(trifluoro methane sulfonyl)imide (LiTFSI), as the salt acts as a plasticizer for the polymer. LiTFSI is the most common lithium salt used in research activities due to its good thermal and electrochemical stability as well as the dissolution behavior of the lithium ion. A further drawback of using PEG as a matrix material is the low melting point in the range of 30-60 °C, depending on the molecular weight. This leads to a liquid system at the working temperature of a lithium ion battery, and hence to dendrite formation.

In this thesis, a polymer based on a PEG-like structure but with enhanced mechanical stability was synthesized. The approach uses physical crosslinking to achieve a network resulting in a solid polymer. Here, the monomer perylene tetracarboxylic dianhydride (PTCDA) was chosen to form a physical crosslinked network via π - π stacking. PTCDA was integrated into the polymer main chain by copolymerization of PTCDA with suitable diamino-functionalized PEG derivatives. Here, Jeffamine ED-series were selected as PEG derivatives which are flanked with PPO-diamine units at both ends (H₂N-

PPO-PEG-PPO-NH₂). Three are different Jeffamines from the ED-series commercially available and used within this thesis: Jeffamine ED-600, Jeffamine ED-900, and Jeffamine ED-2003. The number in the name correlates with the molecular weight of the corresponding Jeffamine. The Jeffamine-ED series will be referred to as PPO-PEG-PPO units. PTCDAs and PPO-PEG-PPO units were used as monomers in a polycondensation reaction performed in the melt. In the first synthesis series, the Jeffamine derivatives were used in excess to control the molecular weight according to the Carothers equation and to enable end-capping. The end-capper contains *tert*-butyl moieties and allows the investigation of the molecular weight of the copolymer *via* ¹H-NMR end-group analysis. Contrary to Jeffamine and PTCDAs, *tert*-butyl groups show signals in the high field of the ¹H-NMR avoiding any interference with the starting materials. For this reason, 4-*tert*-butyl phthalic anhydride (*t*BPA) was selected as the end-capping agent.

Regarding the melt processing capability, a low molecular weight is favored to ensure a low viscosity in the melt. The molecular weight can be tailored on the one hand by varying the length of the PPO-PEG-PPO segment and on the other hand by using an excess of one component in accordance with the Carothers equation. The degree of polymerization according to the Carothers equation for an AA/BB system is defined as **equation 6**:

$$DP = \frac{1+r}{1+r-2pr} \quad (6)$$

Here, r is the stoichiometric ratio of monomer A and monomer B, while $r < 1$, and p is the conversion of the reaction. The maximum degree of polymerization can be achieved when $r = 1$, meaning an exact 1:1 ratio of the starting materials. To enable valid calculations using this equation, the conversion has to be close to 100%. By varying the molar ratio of the starting monomers, the degree of polymerization and hence the chain length of the copolymer can be set to the desired value. A schematic structure of the copolymer was shown in **Figure 25**.

The PPO-PEG-PPO segments enable the solvation of lithium ions and with that the ionic conductivity of the material. The perylene segments ensure certain mechanical stability of the system, proposing, that the perylene segments undergo π - π stacking forming a physically crosslinked network. A schematic illustration of the proposed physically crosslinked network is depicted in **Figure 25**.

This schematic sketch illustrates the physical crosslinks of the perylene segments forming hard segments, which enable a thermally reversible crosslinked network. Due to the ability of low T_g amorphous PEG derivatives to conduct lithium ions, this type of material can be proposed as a matrix respectively binder material in electrolyte and electrode materials in lithium ion batteries. As mentioned before it would advantageously be that the materials are solvent-free and solid-state. Therefore, the synthesis was conducted in a metal reactor in a melt-polycondensation reaction at

elevated temperatures. This avoids the adsorption of water in the hygroscopic PPO-PEG-PPO units and decreases the reaction time. The high reaction temperatures shift the reaction equilibrium, according to the principle of 'le Chatelier', to the product side by removing the formed water. The reaction was carried out under an inert gas atmosphere to prevent side reactions. Further, the constant argon flow fosters the removal of the formed water.

The obtained reaction mixtures were highly viscous. Hence a mechanical stirrer was used to ensure homogeneous mixing of the melt as depicted in **Figure 26**. The temperature was controlled throughout the process by a temperature control unit in combination with an electronic heating unit. The reactor was covered on top with an elastic HNBR rubber lid to maintain an inert gas atmosphere.

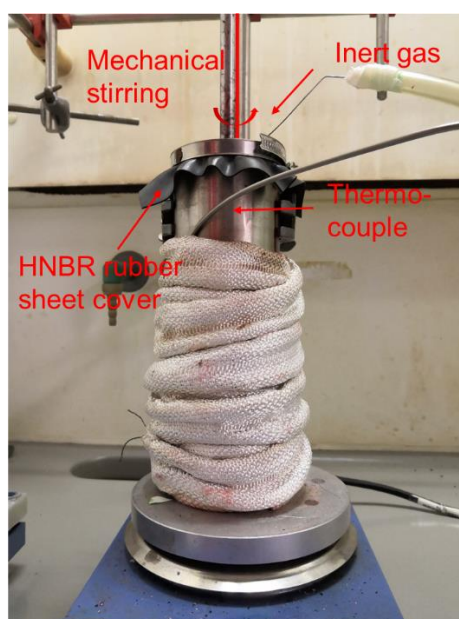


Figure 26: Setup of the polycondensation reactor used for the $(AB)_n$ segmented copolymer bulk synthesis. A metal reactor was utilized as a reaction vessel and heated by a heating jacket. The reaction mixture was mechanically stirred under inert conditions and controlled temperature settings.

For the extensive screening of the optimal synthesis parameters for the polycondensation reaction of PTCDAs with the corresponding PPO-PEG-PPO segments firstly the setup was optimized. In cooperation with our in-house workshop a series of metal reactors were manufactured (**Figure 27**). This enabled an increased throughput of the $(AB)_n$ segmented copolymer synthesis.



Figure 27: Series of three metal reactors used for parallel melt polycondensation reactions for the synthesis of $(AB)_n$ segmented copolymers out of perylene and selected Jeffamines.

The ratio of the monomers was kept the same throughout all the experiments keeping an excess of 25% of Jeffamine to PTCDA. The latter was used as received while the molecular weights of the Jeffamine ED-Series were determined by titration measurements. A solution of Jeffamine in THF was titrated against a solution of HCl in isopropanol (0.1 mol/L) to determine the actual amino groups and to calculate their corresponding average molecular weights, which are listed in **Table 2**.

Table 2: Comparison of calculated average molecular weight of investigated Jeffamines (PPO-PEG-PPO units) given by supplier and determined *via* titration.

Jeffamine ED-Series (H ₂ N-PPO-PEG-PPO-NH ₂)	Average molecular weight from supplier [g mol ⁻¹]	Calculated average molecular weight* [g mol ⁻¹]
600	600	624
900	900	894
2003	2003	2018

*determined *via* titration vs. HCl in isopropanol solution (0.1 mol/L)

Two step synthesis towards tBPA endcapped (AB)_n segmented copolymers

For the melt polycondensation synthesis a two step synthesis was chosen to synthesize (AB)_n segmented copolymers. In the first step the copolymers will be synthesized with a desired molecular weight or number of repeating units, respectively. In the second step the end-capping of the before synthesized copolymer will be done. The end-capping process will be conducted for two reasons. On the one hand the end-capping allows to synthesize an apolar copolymer, beneficial for the use in lithium ion batteries, and on the other hand the usage of a selected end-capper is beneficial for post-synthetic analysis.

The determined average molecular weight *via* titration was used to set the aimed ratio of the monomers. For each synthesis the respective Jeffamine monomer was used in excess, to get amine end-groups of the copolymer (**step 1**) which then enable end-capping (**step 2**). The according reaction equation is shown in **Figure 28**.

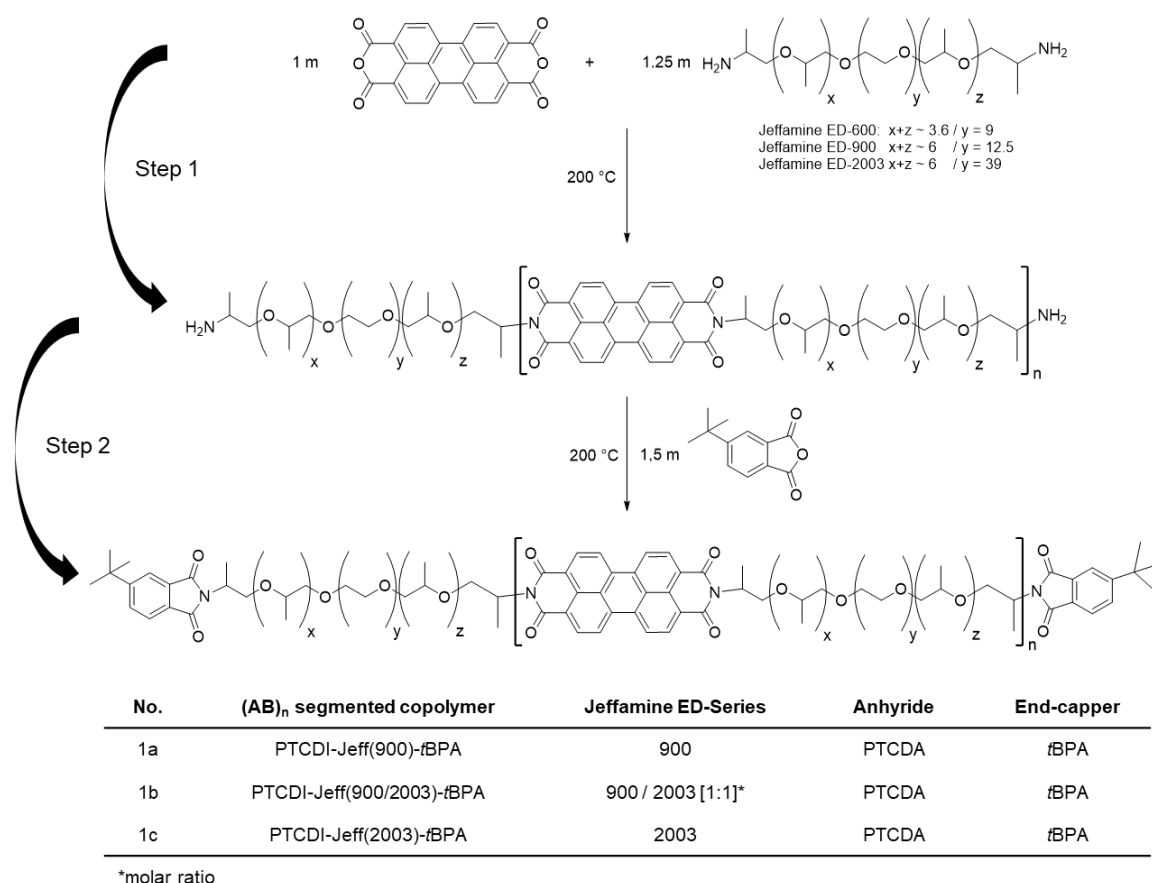


Figure 28: Reaction scheme of the applied melt polycondensation reaction resulting in corresponding (AB)_n segmented copolymers listed in the bottom table.

The elevated reaction temperature of 200 °C was determined to be suitable for the polycondensation reaction. Three different monomers from the Jeffamine ED series were used: Jeffamine ED-600, 900,

and 2003. Jeffamine ED-900 and Jeffamine ED-2003 revealed a homogeneous reaction mixture. However, Jeffamine ED 600 could not be mixed homogeneously due to the applied high content of PTCDA which was not completely dissolved in the reaction melt. Therefore, only Jeffamine ED-900 and Jeffamine ED-2003 were selected for further reactions.

The Carothers equation is only applicable for a conversion close to 100%. The corresponding reaction time of step 1 for a very high conversion was investigated for Jeffamine ED-900/PTCDA in kinetic studies. During the polycondensation reaction of Jeffamine ED-900 and PTCDA, samples were taken out of the reaction mixture hourly to measure FT-IR spectra. Here, the formation of the imide bands at 1655 cm^{-1} (Imide II) and 1700 cm^{-1} (Imide I) was used to track the reaction progress. The measured spectra are shown in **Figure 29**. **Figure 29** (a) shows the full FT-IR spectra of the melt polycondensation reaction of PTCDA and Jeffamine ED-900 from 450 cm^{-1} to 4000 cm^{-1} . The increasing imide bands over time are magnified in **Figure 29** (b). The relative intensity (normalized to the C-H vibration band at 2900 cm^{-1}) *versus* time is plotted in **Figure 29** (c). The formation of imide groups and therefore the progress of the polycondensation reaction reaches a plateau after about 20-25 h. Hence, the reaction time was set to 25 h for further polycondensation syntheses.

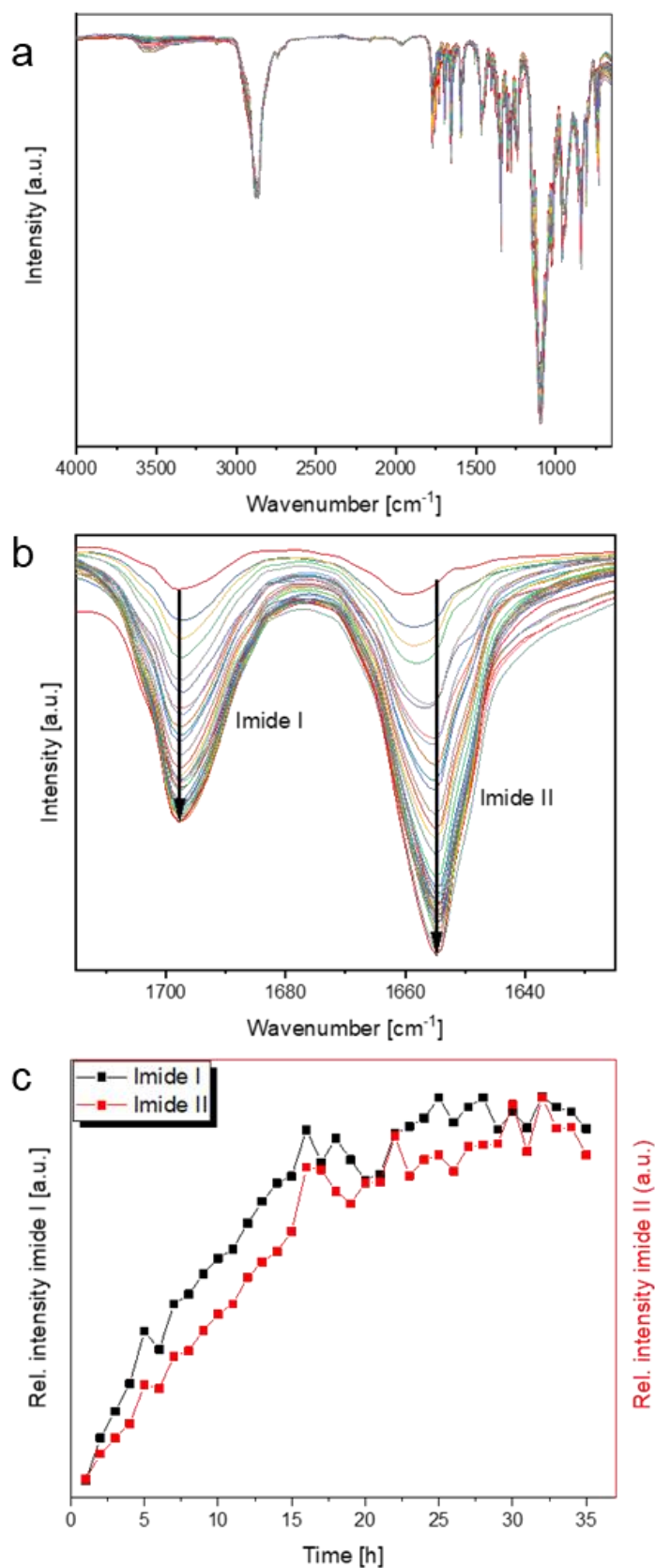


Figure 29: Kinetic investigations on the progression of step 1 of the polycondensation reaction resulting in an (AB)_n segmented imide-based copolymer by FTIR. Every hour the FT-IR spectrum was recorded from a sample of the reaction mixture. (a) recorded full spectra, (b) magnified FT-IR spectra of the imide bands, (c) relative imide band intensities, determined using the maximum intensity, in dependency of the reaction time. The kinetic study shows the reaction reaches a plateau after 20-25 hours meaning the reaction was completed after that time.

After the completion of the copolymerization reaction (cf. **Figure 28**, step 1), the end-capping reaction was performed. *t*BPA was selected as end-capping agent because of the strong NMR signal of the *tert*-butyl group which shows isolated peaks in the high field of the $^1\text{H-NMR}$ and hence enables the calculation of the degree of polymerization of the copolymer. The end-capping reagent was used in a large excess to ensure a complete end-capping of all end groups and somehow to overcome the competing sublimation process at the applied reaction conditions. Unfortunately, *t*BPA sublimates starting at 150 °C (see **Figure 30**). A decrease in the reaction temperature was not appropriate due to a lower reaction rate below 200 °C.

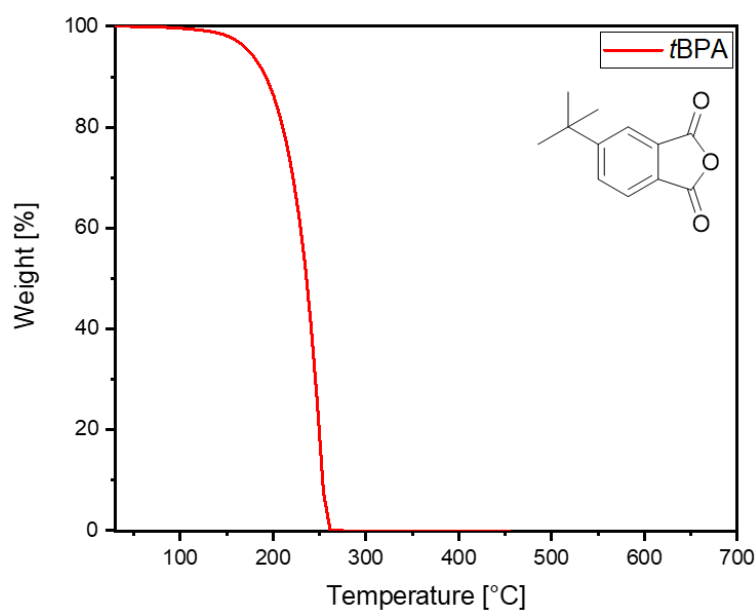


Figure 30: Thermogravimetric investigation on the end-capping reagent 4-*tert*-butyl phthalic anhydride (*t*BPA). Sublimation of *t*BPA is given at about 200 °C. Using *t*BPA in the reaction mixture the reaction temperature should not exceed 200 °C to reduce sublimation before the reaction.

Therefore, the reaction temperature was kept at 200 °C also during end-capping. As in the step before, kinetic FT-IR studies were conducted to follow the reaction progression of the end-capping. Characteristic imide vibration bands of five membered imide rings appear. The different wavenumbers of these bands enable the kinetic investigation although there are already six-membered ring imide groups within the copolymer. Selected FT-IR spectra are depicted in **Figure 31**.

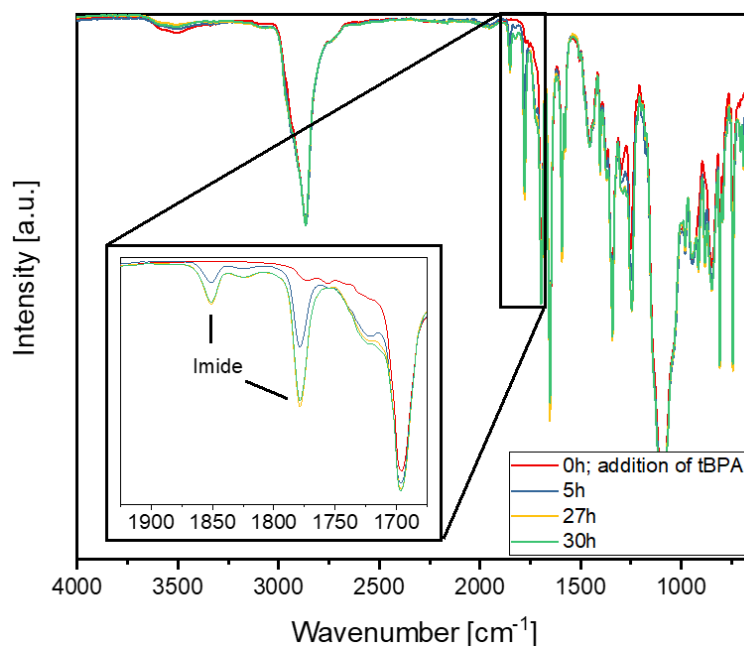


Figure 31: Kinetic investigation on the *tBPA* end-capping reaction of **1a** (PTCDI-Jeff(900)-*tBPA*) to determine the optimal reaction time. Every hour a spectrum was recorded from a sample of the reaction mixture. Here, only selected FT-IR spectra are shown. Since the intensity did not change significantly after 27 and 30 hours, it can be assumed that the reaction was completed after 27 hours.

FT-IR studies revealed the same time frame for the completion of the end-capping reaction as for the copolymerization reaction, showing no change in absorption after 27 h reaction time. After the end-capping process was finished, the excess of *tBPA* end-capper was removed from the polymer melt by sublimation at 200 °C under high vacuum. The removal of the *tBPA*, thus the lack of residual end-capping agent, was followed *via* TGA measurements. Considering a successful end-capping process, there are *tBPA* units on both ends of each polymer chain. This allows the calculation of the number of repeating units and hence the molecular weight by ¹H-NMR. The obtained ¹H-NMR spectrum of **1a** (PTCDI-Jeff(900)-*tBPA*) is shown in **Figure 32**.

The signals of the methyl groups of the *tert*-butyl group of the end-capping agent *tBPA* were used to calibrate the integrals of the perylene and PPO-PEG-PPO segment peaks. Considering the *tert*-butyl groups on both ends, the number of methyl H-atoms can be set to 18 (1.4 ppm). Using this calibration, the perylene units at about 7.3 ppm can be determined to be 80 protons. With 8 protons per PTCDI unit, the average number of PTCDI segments per polymer chain is calculated to be 10. This is equivalent to the average number of 11 PPO-PEG-PPO segments in each polymer, due to the excess of the Jeffamine monomers according to the Carothers equation. The resulting average molecular weight of the copolymer can be calculated as follows:

$$10 \cdot M_{(\text{PTCDI})} + 11 \cdot M_{(\text{Jeffamine})} + 2 \cdot M_{(\text{tBPA})} = 10 \cdot 392 \frac{\text{g}}{\text{mol}} + 11 \cdot 894 \frac{\text{g}}{\text{mol}} + 2 \cdot 204 \frac{\text{g}}{\text{mol}} = 10,242 \frac{\text{g}}{\text{mol}} \quad (7)$$

Theoretical calculations using the Carothers equation predict 9 PTCDA units. This proves that the average molecular weight of the resulting polymer can be successfully determined by the ratio of the starting monomers with only small deviations. Several polymers were synthesized accordingly.

Table 3 lists a selection of synthesized polymers.

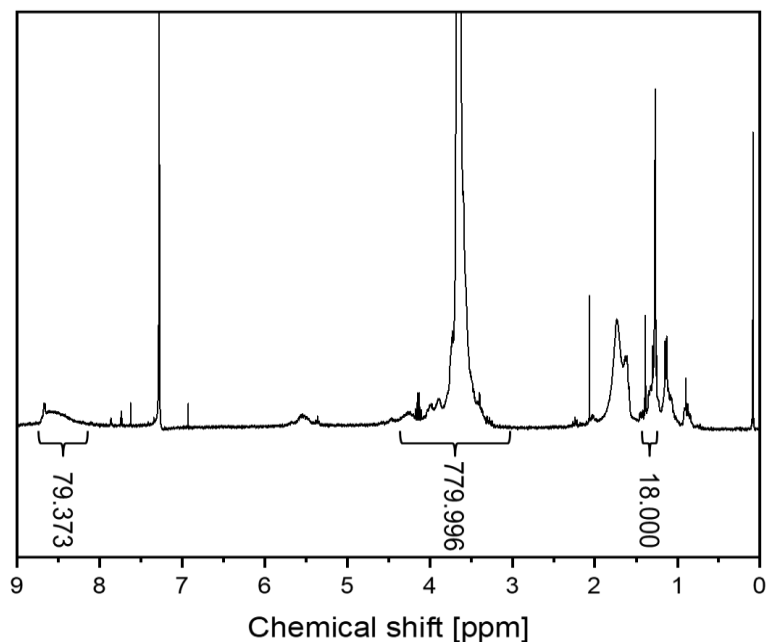


Figure 32: $^1\text{H-NMR}$ spectrum of **1a** (PTCDI-Jeff(900)-*t*BPA). The number of repeating units can be calculated by using the 18 H-atoms of methyl groups of *t*BPA at 1.4 ppm for calibration. According to this calibration, the number of PTCDA repeating units can be calculated to 10.

Table 3: Overview of synthesized copolymers, their applied weight ratios, and their average molecular weights.

No.	Polymer	PTCDA** [wt-%]	Jeffamine ED-900*** [wt-%]	Jeffamine ED-2003*** [wt-%]	Calculated average molecular weight [g mol ⁻¹]
1a	PTCDI-Jeff(900)- <i>t</i> BPA	28	72	-	10,242
1b	PTCDI-Jeff(900/2003)- <i>t</i> BPA*	22	24	54	20,334
1c	PTCDI-Jeff(2003)- <i>t</i> BPA	15	-	85	26,526

* 1:1 molar ratio of Jeffamine ED-900 and Jeffamine ED-2003

** based on the number of repeating units of 10

*** based on the number of repeating units of 11

Further detailed investigations revealed that exposing the copolymer to this high temperature during the melt polycondensation leads to changed behavior in the melt. After such a high and long thermal treatment, a very high viscous melt is formed which indicates side reactions. A possible side reaction could be the reaction of amino end groups with the carbonyl C-atom of the imide unit which forms an

imine-linked side chain. This side reaction would lead to crosslinking and with that to a distinct molecular weight increase of the polymer. A possible reaction scheme is shown in **Figure 33**.

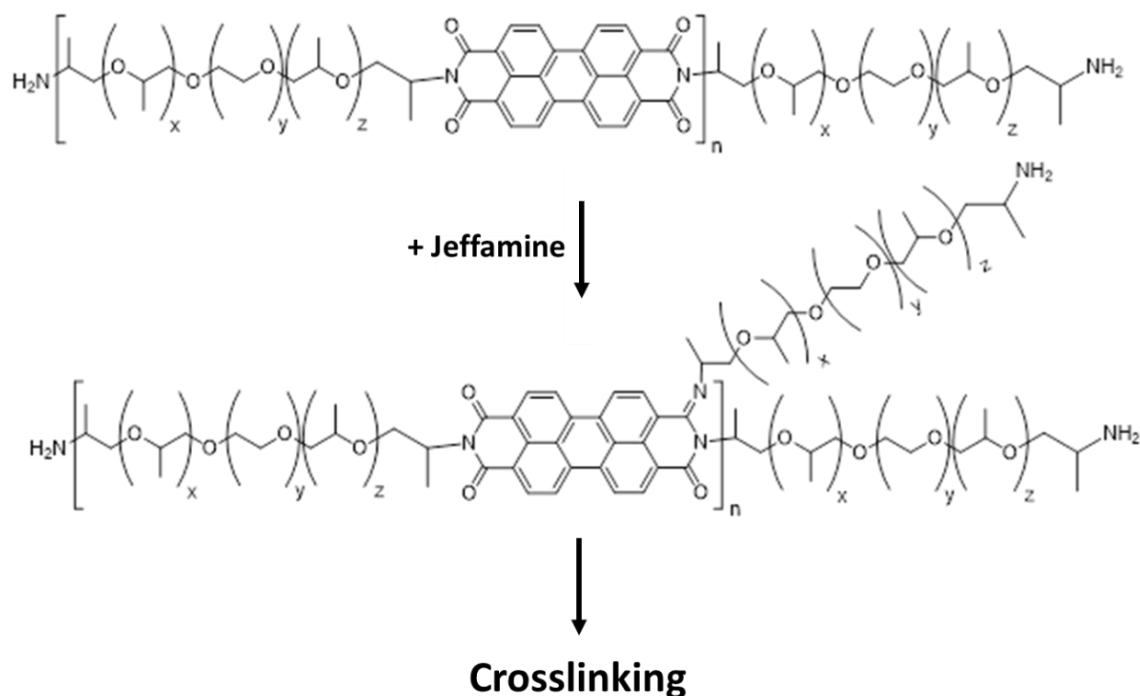


Figure 33: Possible side reaction occurring during long-term copolymerization of PTCDA and Jeffamine ED Series. The functional amines or amino end-groups react with the imide groups of the perylene segments resulting in a distinct increased molecular weight or crosslinked polymer chains.

The possible side reaction required an optimization of the polymerization procedure. It would be beneficial to shorten the reaction time and remove functional groups on the copolymer chain that could lead to side reactions.

One step synthesis of (AB)_n segmented copolymers

For this purpose, the structure of the segmented (AB)_n copolymer was not changed significantly, but it was changed decisively. The monomer ratio was switched and the polymer synthesized with 25% excess of PTCDA resulting in a perylene anhydride end-functionalized copolymer. By doing so, the need for an end-capper to ensure no protic end groups becomes obsolete. The resulting telechelic bis anhydride polymer structure is schematically shown in **Figure 34**.



Figure 34: Schematic structure of the (AB)_n segmented copolymers, consisting of repeating units of perylene and PPO-PEG-PPO segments, but show telechelic perylene anhydride groups.

To further decrease the reaction time, $\text{Zn}(\text{OAc})_2$ - a common catalyst for polycondensation reactions - was used. The reaction scheme for the optimized polycondensation reaction is depicted in **Figure 35**.

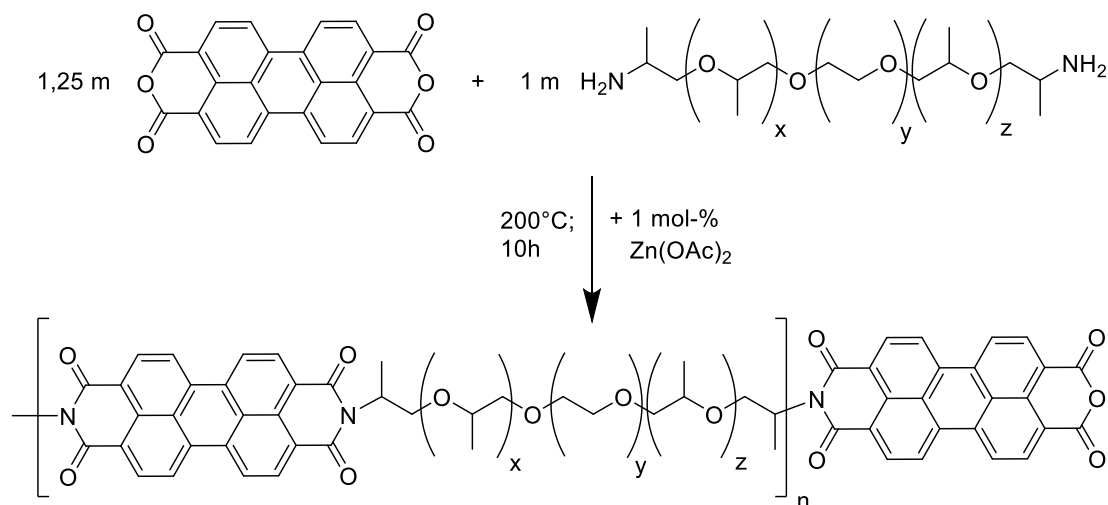


Figure 35: Catalyzed polycondensation reaction leading to telechelic bis anhydride (AB)_n segmented copolymer consisting of perylene and selected PPO-PEG-PPO segments. Small amounts of $\text{Zn}(\text{OAc})_2$ were added as catalyst.

The resulting polymer is *in situ* end-functionalized with PTCDA. An overview of all (AB)_n segmented copolymers synthesized in this thesis is shown in **Table 4**.

Table 4: Overview of synthesized (AB)_n segmented copolymers and their used terms.

No.	(AB) _n segmented copolymer	Jeffamine ED-Series	Anhydride	End-capper/ telechelic group
1a	PTCDI-Jeff(900)- <i>t</i> BPA	900	PTCDA	<i>t</i> BPA
1b	PTCDI-Jeff(900/2003)- <i>t</i> BPA	900/2003 [1:1]*	PTCDA	<i>t</i> BPA
1c	PTCDI-Jeff(2003)- <i>t</i> BPA	2003	PTCDA	<i>t</i> BPA
2a	PTCDI-Jeff(900/2003)	900/2003 [1:1]*	PTCDA	peryene anhydride
2b	PTCDI-Jeff(2003)	900/2003 [1:1]*	PTCDA	peryene anhydride

*molar ratio

As for the prior polymerization reactions, kinetic studies were performed *via* FT-IR. The spectra are depicted in **Figure 36**.

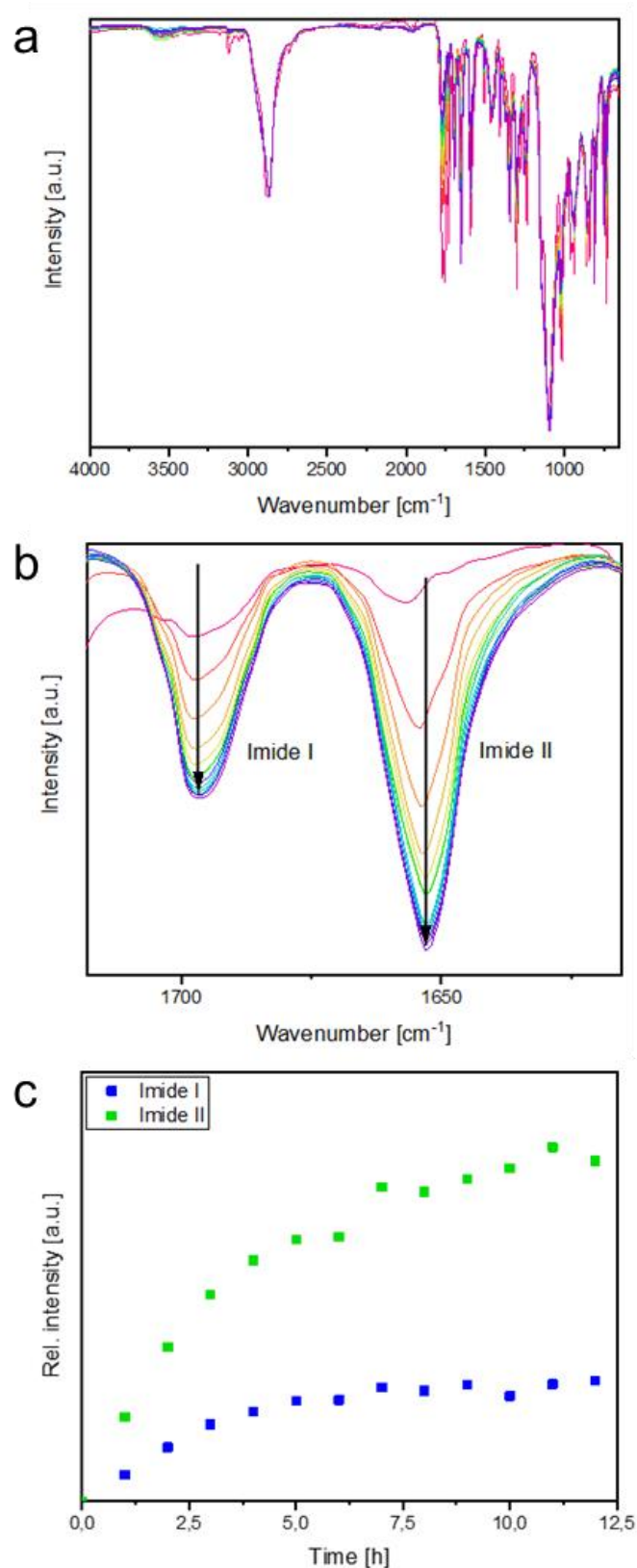


Figure 36: Kinetic investigations on the progression of the polycondensation reaction resulting in the telechelic bis anhydride (AB)_n segmented copolymer **2b** (PTCDI-Jeff(2003)) by FT-IR. Every hour a sample was recorded. (a) Recorded full spectra, (b) magnified FT-IR spectra of the imide bands, (c) relative imide band intensities, determined using the maximum intensity, in dependency of the reaction time. The kinetic study shows the reaction reaches a plateau after 10 hours meaning the reaction was completed after that time.

The formation of the imide bands at 1655 cm^{-1} (Imide II) and 1695 cm^{-1} (Imide II) was used to track the reaction progression. The C-H vibration band at 2900 cm^{-1} was used as the reference. A plateau of the imide peaks intensity can be already achieved after 10 hours of reaction, decreasing the reaction time by a factor of 3 compared to the non-catalyzed reaction before (see also **Figure 29**). However, the reaction of PTCDA with Jeffamine ED-900 resulted in a somehow inhomogeneous reaction mixture. It seems that the high perylene content in this copolymer lead to undissolved PTCDA which could not be dissolved in hot Jeffamine and therefore could not react properly. This could be observed by residual PTCDA in the final reaction mixture after no reaction occurred anymore. Therefore, the results of the $(AB)_n$ segmented copolymer based on PTCDA with Jeffamine ED-900 will be not discussed in more detail in the upcoming chapters. An overview of the synthesized $(AB)_n$ segmented copolymers is shown in **Table 5**.

Table 5: Overview of synthesized copolymers, their applied weight ratios, and their calculated average molecular weights.

No.	Polymer	PTCDA** [wt-%]	Jeffamine ED-900*** [wt-%]	Jeffamine ED-2003*** [wt-%]	Calculated average molecular weight [g mol ⁻¹]
1b	PTCDI-Jeff(900/2003)-tBPA*	22	24	54	20.334
1c	PTCDI-Jeff(2003)-tBPA	15	-	85	26.526
2a	PTCDI-Jeff(900/2003)-PTCDA*	26	26	48	16.549
2b	PTCDI-Jeff(2003)-PTCDA	18	-	82	21.778

*1:1 molar ratio of Jeffamine ED-900 and Jeffamine ED-2003

** based on the number of repeating units of 10

*** based on the number of repeating units of 11

3.1.2 Thermal characterization of $(AB)_n$ segmented copolymers

The thermal characterization of the $(AB)_n$ segmented copolymers was performed by TGA and DSC measurements. Before characterizing the $(AB)_n$ segmented copolymers the thermal properties of the neat Jeffamines were investigated. **Figure 37** depicts the TGA and DSC curves of the neat Jeffamine ED-900 and Jeffamine ED-2003.

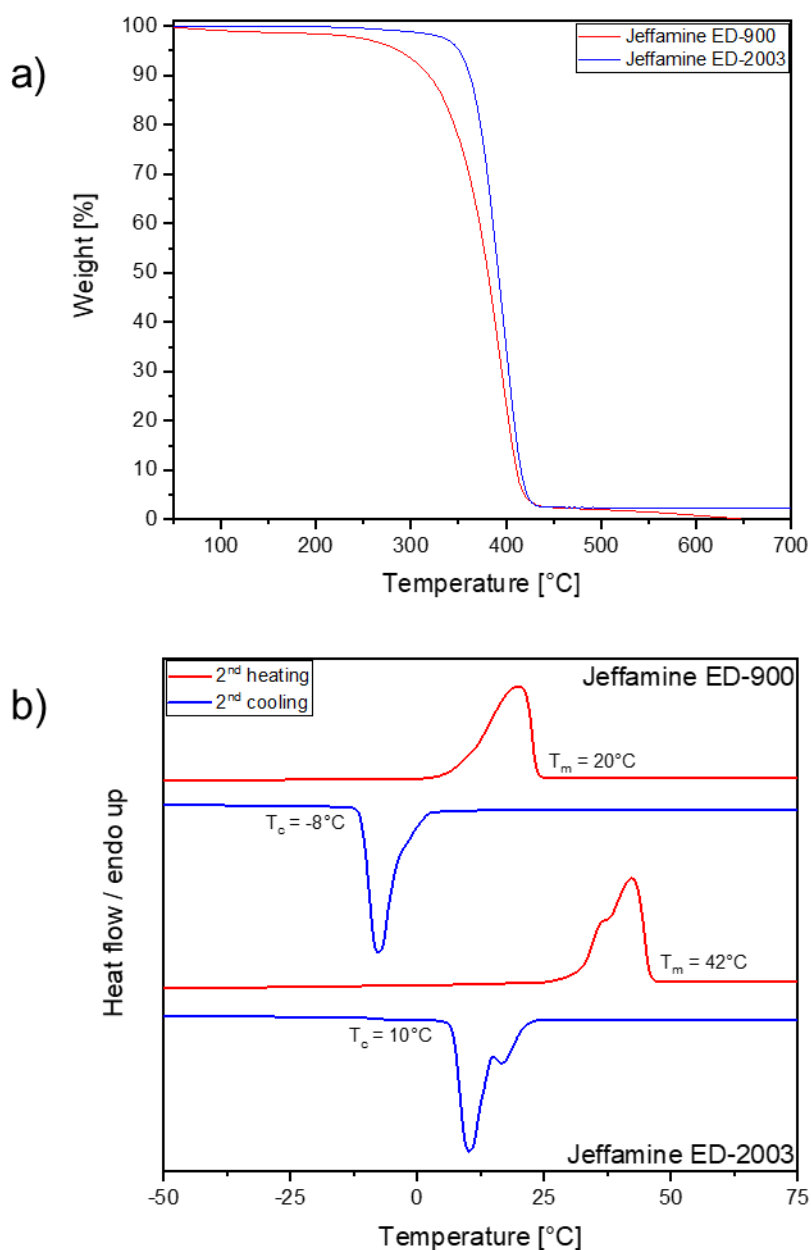


Figure 37: Thermal characterization of neat Jeffamine ED-900 and ED-2003. a) TGA measurements. b) DSC measurements (2nd heating and cooling curves). Both measurements were performed under nitrogen atmosphere and with a heating cooling rate of 10 K min^{-1} , respectively.

The TGA measurements were carried out under nitrogen atmosphere with a heating rate of 10 K min^{-1} . The thermogram of Jeffamine ED-900 (**Figure 37** (a), red) shows an earlier weight loss than those of the Jeffamine ED-2003 ((**Figure 37** (a), blue). This could be attributed to the water absorption of the samples. Both samples were placed in the TGA at the same time, however, the sample of Jeffamine ED-2003 was measured first and the sample of Jeffamine ED-900 was measured afterward and thus was under ambient conditions for longer times. Therefore it could soak more water compared to the sample of Jeffamine ED-2003. However, both Jeffamines are stable up to at least 200°C in an inert atmosphere having a $T_{5\text{wt}\% \text{loss}}$ at 280°C (ED-900) and 360°C (ED-2003), respectively. Because of the

hygroscopic properties of Jeffamines the Jeffamines were dried at 100 °C under a high vacuum for at least 3 hours before using for all following measurements and the melt polycondensation synthesis.

Figure 37 (b) depicts DSC curves of Jeffamine ED-900 and Jeffamine ED-2003. Jeffamine ED-2003 is a solid material at room temperature with a melting range maximum of 42°C, while Jeffamine ED-900 is liquid, with a melting range maximum of 20 °C. The curves show additional shoulders at the melting and crystallization peaks. These shoulders are more distinct for Jeffamine ED-2003 compared to Jeffamine ED-900. This might be attributed to the flanking PPO units on each side of the Jeffamine. The melting temperature increases with increasing molecular weight, which is a common behavior of polymeric materials.

For PTCDA there was neither a transition temperature nor a weight loss detected using DSC and TGA investigations respectively, therefore it was not investigated in more detail.

Thermal characterization of tBPA end-capped (AB)_n segmented copolymers

For the tBPA end-capped copolymers, those samples were selected which showed less or no side reactions indicated by a low melt viscosity. The TGA curves of selected tBPA end-capped (AB)_n segmented copolymers are depicted in **Figure 38**.

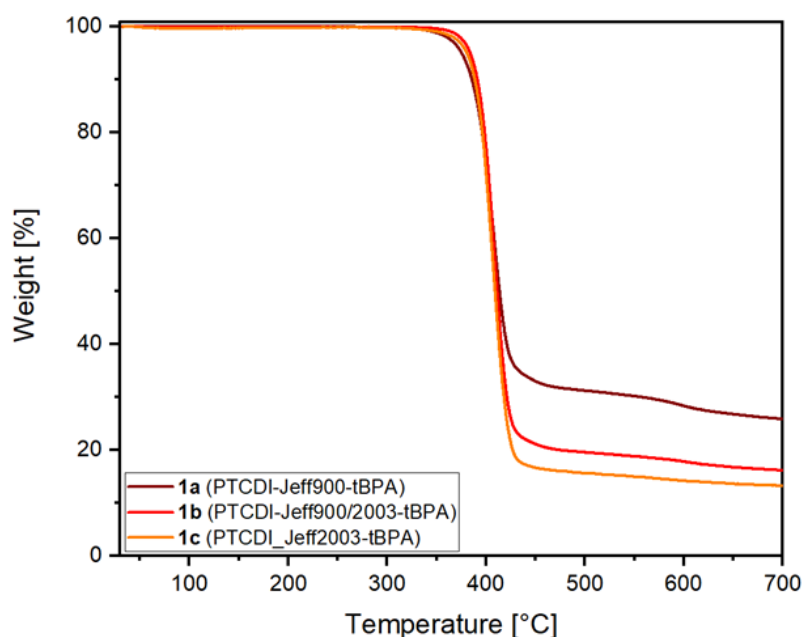


Figure 38: Thermogravimetric analysis of selected tBPA end-capped (AB)_n segmented copolymers. All copolymers are stable up to temperatures around 300 °C. This thermal stability allows processing of the copolymers at very high temperatures without decomposition.

The TGA measurements were performed under an inert atmosphere and applying a heating rate of 10 K min⁻¹. All synthesized tBPA end-capped (AB)_n segmented copolymers showed a similar thermal

gravimetric behavior. They are highly thermally stable up to temperatures of 300 °C. Notably, the copolymers are more stable than the starting Jeffamine monomers. This indicates that thermal degradation occurs due to an unzipping process induced by the amino chain ends. By end-capping the polymers, the unzipping process is more hindered.

In addition to TGA measurements, DSC measurements were performed. The DSC curves for the **1a** (PTCDI-Jeff(900)-*t*BPA) (top) and **1c** (PTCDI-Jeff(2003)-*t*BPA) (bottom) are depicted in **Figure 39**.

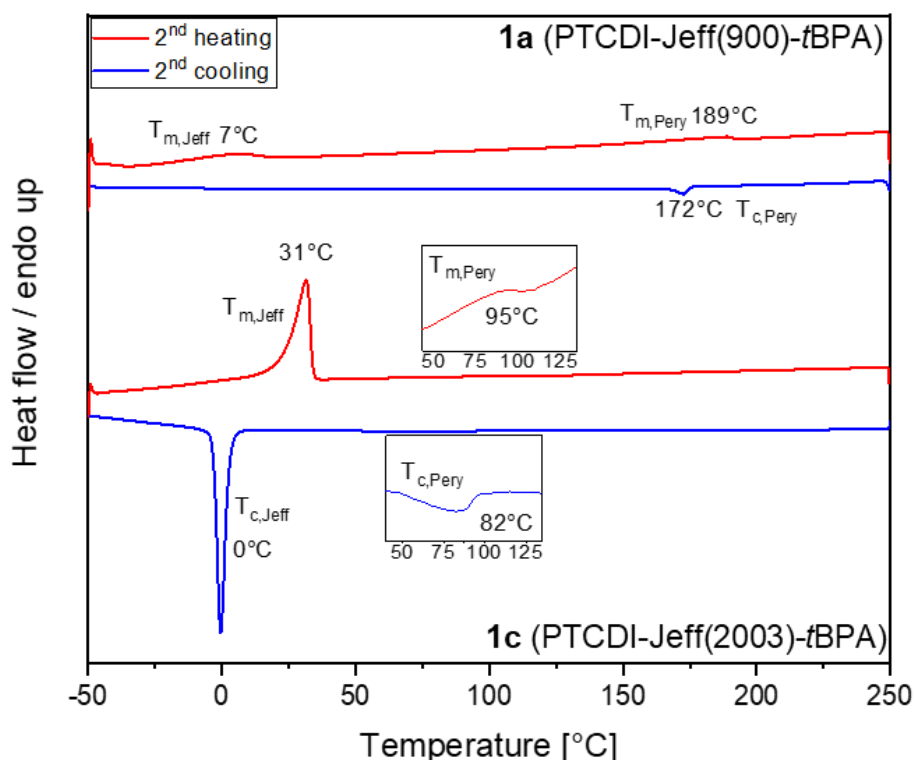


Figure 39: 2nd heating (red) and 2nd cooling (blue) DSC curves of **1a** (PTCDI-Jeff(900)-*t*BPA) (top) and **1c** (PTCDI-Jeff(2003)-*t*BPA) (bottom).

The copolymer **1a** (PTCDI-Jeff(900)-*t*BPA) shows a less intense crystallization peak of the PPO-PEG-PPO units compared to **1c** (PTCDI-Jeff(2003)-*t*BPA). This can be explained by the different molecular weights of the PPO-PEG-PPO segments. PEG-based materials tend to crystallize, starting from a molecular weight of about 1000 g mol⁻¹. Therefore, the copolymer with Jeffamine ED-900 segments, which has a molecular weight slightly below that value, reveals a small melting peak. While the copolymer with Jeffamine ED-2003 segments shows a pronounced melting peak at 31 °C.

The proposed stacking of the perylene segments within the copolymers was proven by DSC measurements by the arising melting peaks at elevated temperatures indicating the assembly of the perylene units. Depending on the installed PPO-PEG-PPO segment and the corresponding relative weight ratio of PPO-PEG-PPO to PTCDI, the melting temperature of the perylene segments varies

between 95 °C and 189 °C. With increasing perylene content in the copolymer, the melting temperature of the perylene segments increases, too. For a more detailed investigation and to tune the melting temperature, copolymers using different ratios of PPO-PEG-PPO to perylene were synthesized. The DSC curves of the copolymer using a 1:1 mixture of Jeffamine ED-900 as well as Jeffamine ED-2003 in combination with PTCDA is shown in **Figure 40**.

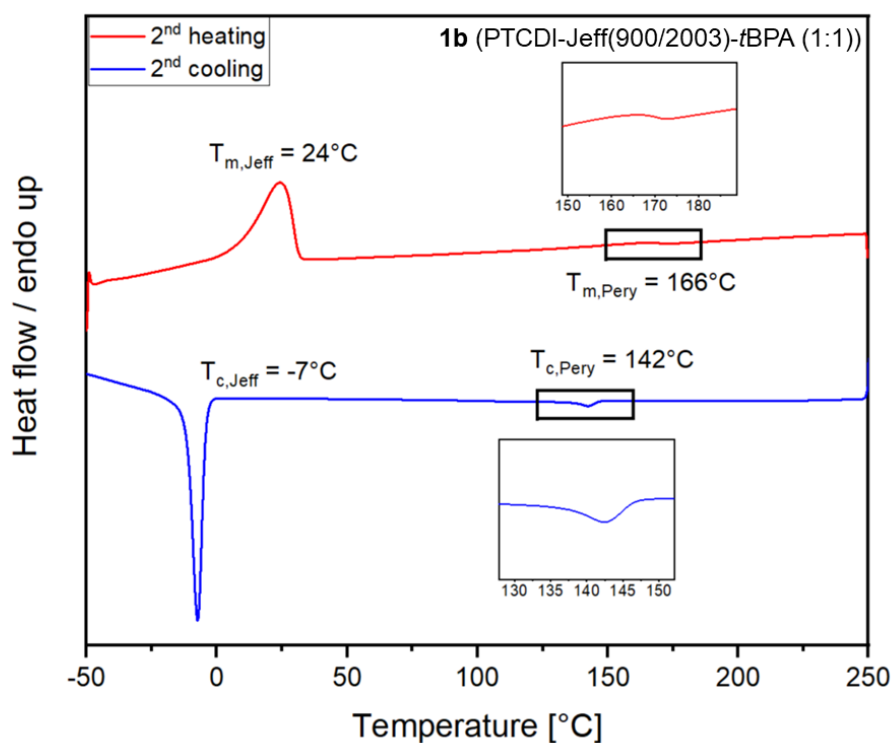


Figure 40: 2nd heating (red) and 2nd cooling (blue) DSC curves of **1b** (PTCDI-Jeff(900/2003)-tBPA [1:1]). The melting range of the PPO-PEG-PPO units as well as the perylene units are in between that of the copolymers containing only one type of PPO-PEG-PPO units.

The melting temperature range of the copolymer **1b** (PTCDI-Jeff(900/2003)-tBPA [1:1]) shows a maximum at 166 °C which is between the melting temperature of the segmented ‘homopolymers’. However, there is no linear trend in the melting behavior of the different synthesized copolymers observable.

Thermal characterization of PTCDA-terminated $(AB)_n$ segmented copolymers

Following the *t*BPA end-capped copolymers, the PTCDA-terminated copolymers were characterized in terms of their thermal behavior. The corresponding TGA curves are depicted in **Figure 41**.

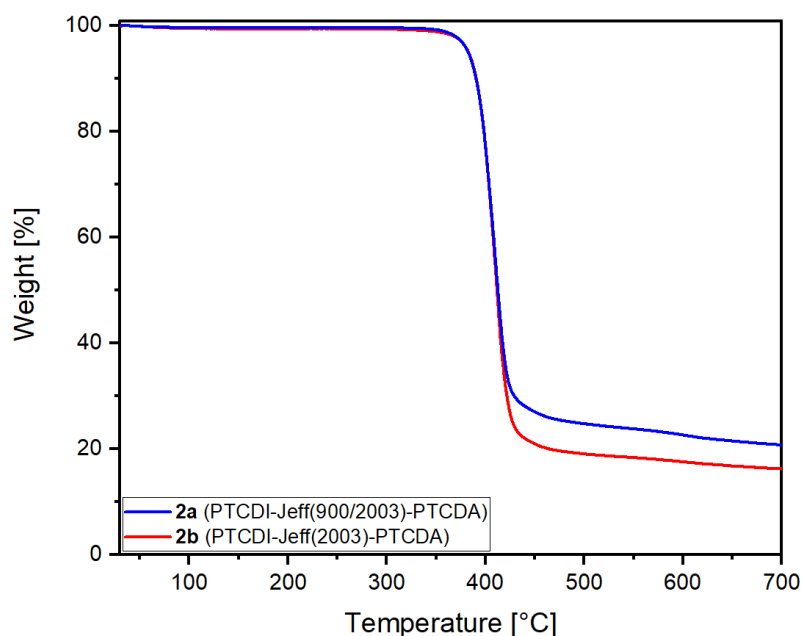


Figure 41: Thermogravimetric analysis of $(AB)_n$ segmented PTCDA-terminated copolymers. All copolymers are thermal stable up to temperatures of around 300 °C. This thermal stability allows the processing of the copolymers at very high temperatures without thermal decomposition.

The TGA measurements were performed under nitrogen and the applied heating rate of 10 K min⁻¹. The thermograms of the PTCDA-terminated copolymers show comparable results to the *t*BPA end-capped copolymers, showing high thermal stability up to temperatures of 300 °C. Additionally, DSC measurements were carried out with these copolymers. The DSC curves are depicted in **Figure 42**.

The DSC measurements were carried out under a nitrogen atmosphere and with a heating and cooling rate of 10 K min⁻¹. Compared to the *t*BPA end-capped copolymer the PTCDA-terminated copolymer reveals a shift in the assembly temperature of the perylene imide units of about 10 K. This phenomenon correlates with the increasing perylene imide content and the polar anhydride group in the PTCDA-terminated copolymers. The higher number may result in larger or differently shaped perylene units assembling, leading to a higher transition temperature in the resulting polymer. Thus, corresponding transition temperatures are shifted to slightly higher temperatures compared to the *t*BPA end-capped counterparts.

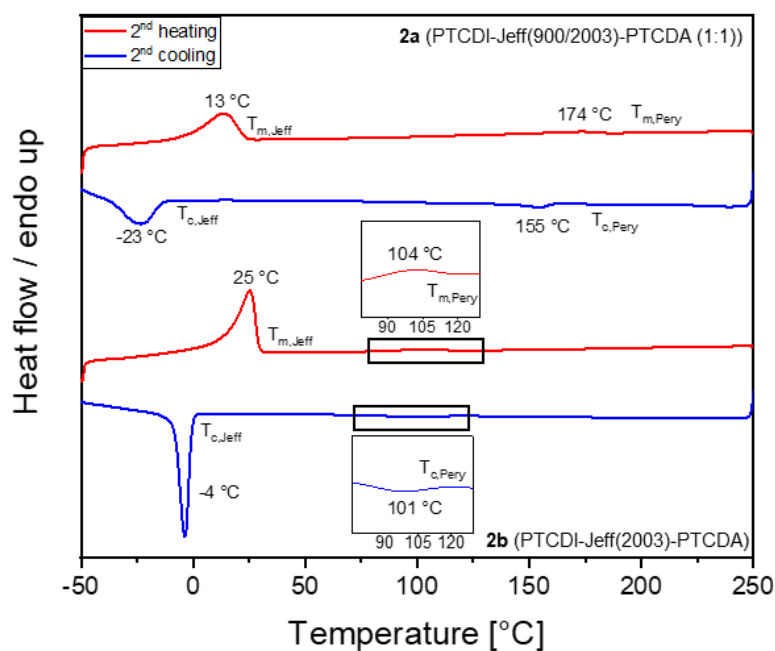


Figure 42: 2nd heating (red) and 2nd cooling (blue) DSC curves of PTCDA-terminated **2a** (PTCDI-Jeff(900/2003)-PTCDA) (top) and **2b** (PTCDI-Jeff(2003)-PTCDA) (bottom). The melting temperatures of the PTCDA-terminated copolymers are slightly higher than those of their *t*BPA end-capped counterparts. This can be expected due to the slightly higher amount of perylene units in the overall copolymer composition.

The DSC curves of all synthesized (AB)_n segmented copolymers indicate a physically crosslinked material due to the π - π stacking of perylene units. In addition, XRD measurements were performed to investigate the π - π stacking in more detail. Therefore, a film of the copolymer **1b** (PTCDI-Jeff(900/2003)-*t*BPA) with a thickness of about 200 μm was prepared by doctor blading onto a silicon wafer.

The thermal reversibility of the stacking was also investigated *via* XRD. The before-mentioned film was heated from 30 $^{\circ}\text{C}$ to 200 $^{\circ}\text{C}$. Every 10 K an isothermal annealing step was performed for 5 min and an XRD pattern recorded. Selected XRD patterns at different temperatures are plotted in **Figure 43**.

The XRD patterns in **Figure 43** show the temperature-dependent evolution of the reflex at $2\Theta = 25^{\circ}$. The reflex at 27° could not be attributed to a specific ordered structure in the measured sample, and therefore was not investigated in more detail. The Θ angle is defined by the Bragg's law:

$$n \lambda = 2 d \sin \theta \quad (8)$$

Here n is the diffraction order, λ the wavelength, d the lattice plane distance and θ the glancing angle.

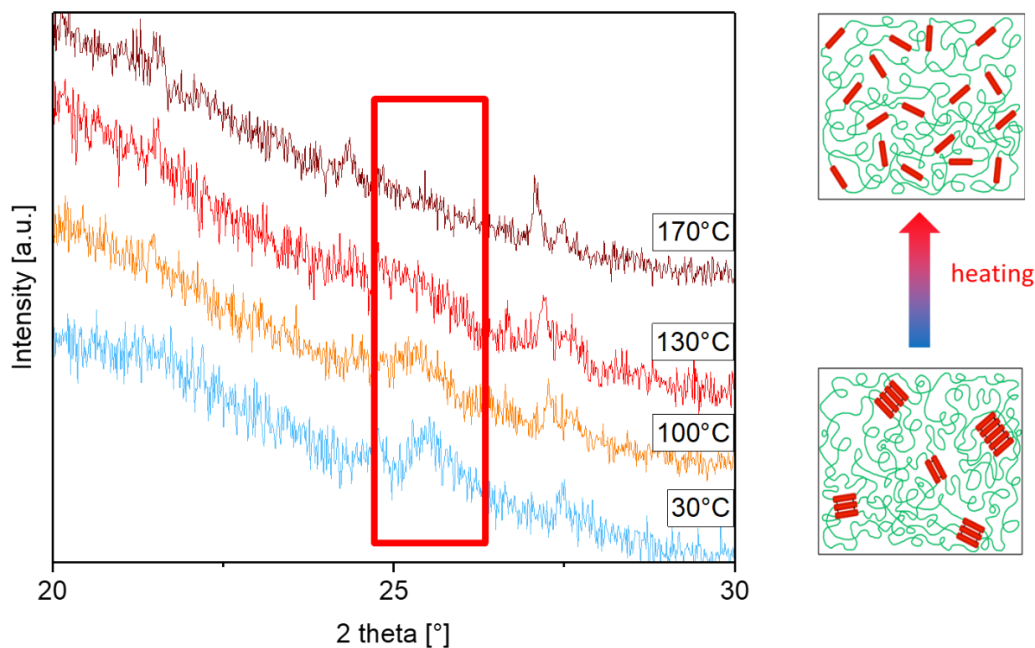


Figure 43: Temperature dependent XRD diffraction spectra of **1b** (PTCDI-Jeff(900/2003)-tBPA). A doctor blade coated film on a silicon wafer was heated up from room temperature respectively 30°C up to 170°C in 10 K steps. In this pattern characteristic measurements were selected. Here the disappearing of the peak resulting from ordered perylene units because of the π - π interactions at roughly 25° [2 Θ] was determined by heating. A clear decrease in intensity can be observed at 130°C before the peak disappears completely at 170°C.

This reflex at 25° indicates the π - π stacking of the perylene units which decreases with increasing temperature. At 170 °C, the reflex disappears completely. This is attributed to the melting of crystals at 166 °C as indicated by DSC measurements. The disassembly of the stacked perylene units starts already above 100 °C indicating different shapes or sizes of the π - π stacking of the perylene units. The isothermal annealing steps of 5 min during the XRD measurement ensures the homogeneous temperature throughout the sample prior to the measurement. To prove the thermal reversibility of this behavior, the analysis was reversed by starting at high temperatures and decreasing the temperature over time and measuring every 10 K. The corresponding XRD patterns are shown in **Figure 44**.

This measurement states the reversibility of the π - π stacking of the perylene units due to the arising of the peak at $2\Theta = 25^\circ$ by decreasing the temperature from 170 °C to 30 °C. At the temperature of 100 °C, the stacking seems to be mostly reestablished. The principle of a thermal reversible crosslinking could be demonstrated by this measurement.

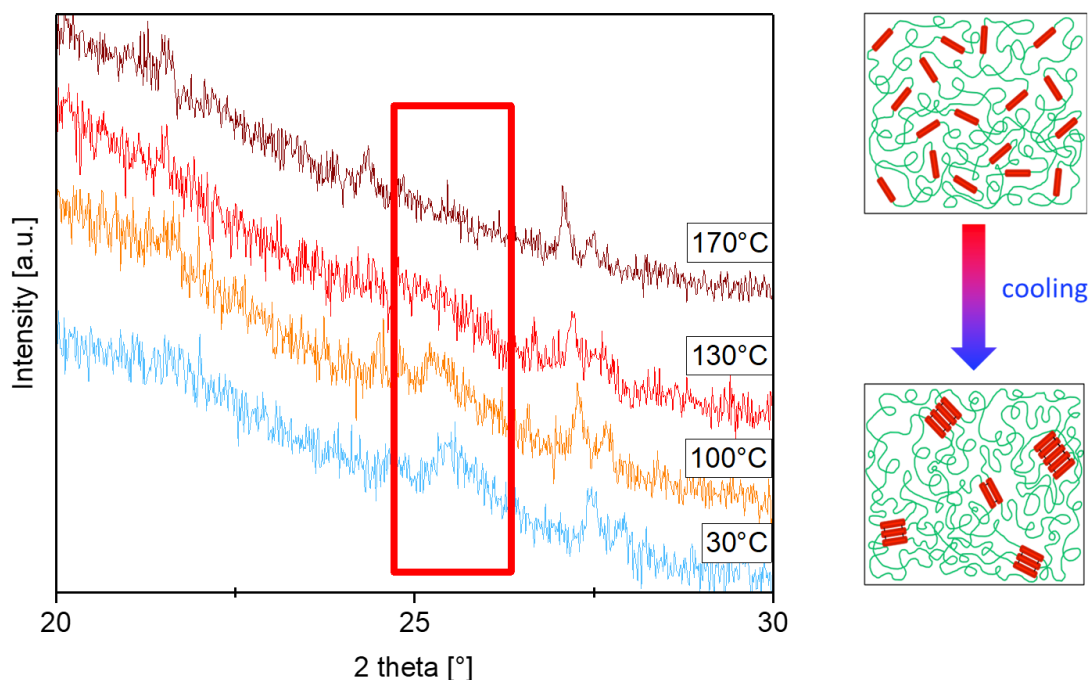


Figure 44: Temperature-dependent XRD diffraction spectra of **1b** (PTCDI-Jeff(900/2003)-*t*BPA). A doctor blade coated film on a silicon wafer was cooled down from 170°C to room temperature in 10 K steps. In this pattern characteristic measurements were selected. Here the development of the peak resulting from the ordered perylene units because of the π - π interactions at roughly 25° [2 Θ] was determined by cooling. The arise of the peak can be determined at about 130 °C before the peak increases further at lower temperatures. This indicates the aggregation of the perylene units in the copolymer material consisting of stacked perylene segments and amorphous PPO-PEG-PPO segments.

In addition to XRD studies, UV/Vis spectra were recorded to further investigate the thermally-induced (dis-)assembly of the perylene units. In many applications, perylene imide derivatives are used as red dye indicating its UV/Vis sensitivity. Depending on the morphology and substitution, the perylene units differ in their absorption of light. There is a shift from the stacked perylene towards the 'single' perylene. For the temperature-dependent investigations on the stacking behavior, a film of **1b** (PTCDI-Jeff(900/2003)-*t*BPA) was spin-coated on a glass substrate, using a 2 wt-% solution of **1b** (PTCDI-Jeff(900/2003)-*t*BPA) in THF. The obtained film showed a layer thickness of about 200 nm. The film was heated in the UV/Vis heating cell under inert atmosphere from 25 °C to 200 °C, in 20 K steps and annealed at each temperature for 5 minutes. For the measurement the scan speed was held at 1000 nm min⁻¹ while heating with 5 K min⁻¹. To demonstrate the thermal reversibility of this physical crosslinking, the sample was subsequently cooled down again measuring every 10 K under analogous conditions. The obtained spectra are shown in **Figure 45**.

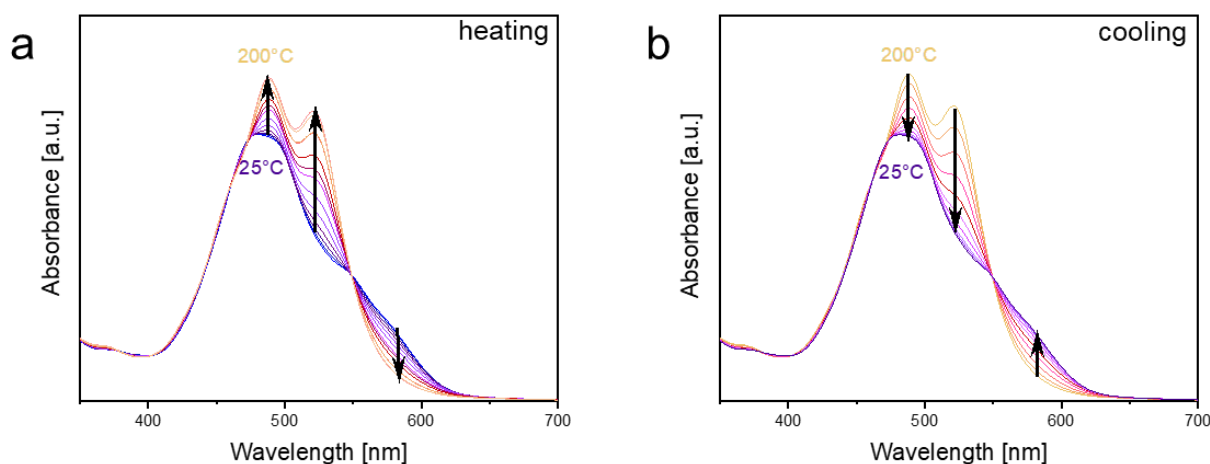


Figure 45: UV/Vis investigation to determine the thermal reversibility of the π - π interactions of the perylene units in the polymer **1b** (PTCDI-Jeff(900/2003)-*t*BPA). For that purpose, a thin film of 200nm was spin coated on a glass substrate. This film was investigated via UV/Vis by heating (a) the film from room temperature up to 200 °C and cooling down (b) afterwards back to room temperature. Every 20 °C the sample was kept at the corresponding temperature for 5 min, and at the end of each temperature step the measurement carried out. The increase of the band at 487nm respectively at 520nm demonstrates the disappearance of the π - π interactions of the perylene units. While cooling down the bands decrease again, which indicates the reforming of the π - π interactions and thus demonstrates that the physical crosslinking is thermally reversible.

In addition to the XRD analysis, the UV/Vis investigations demonstrate the thermal reversibility of the π - π stacking of the perylene units. In **Figure 45** (a) the sample was heated from 25 °C to 200 °C. The increase of the bands at 487 nm and at 520 nm, respectively, as well as the decrease of the band at 580 nm indicate the disassembly of the perylene units. This is in accordance with studies in literature^[93]. The shoulder of the main peak at 520 nm appears only for 'single' perylene units. In this way, this analysis demonstrates the thermal reversibility of the stacking of the perylene units forming a physical crosslink.

3.1.3 Mechanical characterization

After investigating the thermal reversibility of the π - π stacking of the perylene units, investigations on the thermal shape stability were performed. Therefore, small sticks of pure Jeffamine ED-2003 as well as **2b** (PTCDI-Jeff(2003)-PTCDA) were prepared and placed on a heatable aluminum plate. The samples were heated up from room temperature (**Figure 46** (a)) to 100 °C (**Figure 46** (b)). Images at selected temperatures are shown in **Figure 46**.

The sample of the pure Jeffamine® ED-900 stick, without perylene units, is completely molten after heating the samples at 100 °C while the copolymer of **2b** (PTCDI-Jeff(2003)-PTCDA) is still stable in shape and does not show any change of shape during temperature increase. This investigation indicates a clear impact of the formed π - π stacking of the perylene units on the mechanical stability of the copolymer material.

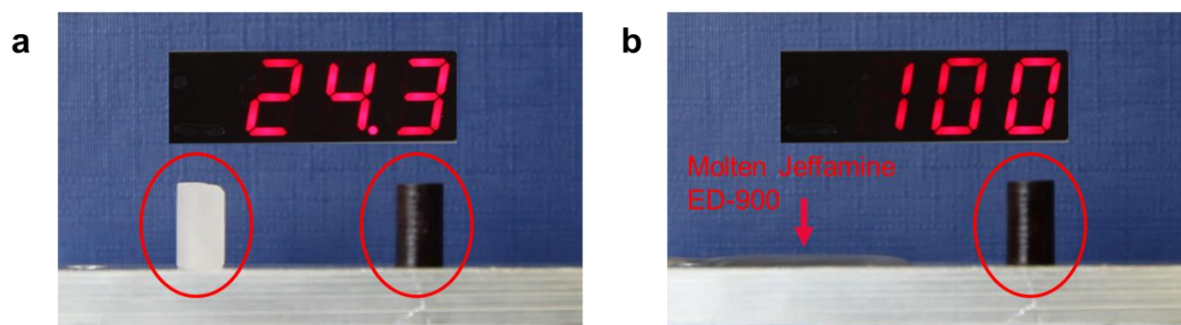


Figure 46: Thermal shape stability investigation to demonstrate the influence of the copolymerized perylene units. In picture (a) there are two cylindrical specimens (left: neat Jeffamine[®] ED-900; right: copolymer **2b** (PTCDI-Jeff(2003)-PTCDA) at room temperature. Both specimens are mechanically stable and stable in shape. In picture (b) the samples are heated at 100 °C. The neat Jeffamine[®] ED-900 is completely molten, while the copolymer **2b** (PTCDI-Jeff(2003)-PTCDA) is still in shape and did not melt.

3.1.4 Melt-processing of (AB)_n segmented copolymers

(AB)_n segmented copolymers with a thermally reversible physical network can be processed *via* melt-processing techniques. Here, the (AB)_n segmented copolymers were processed via extrusion-based 3D printing. For that, filaments were prepared *via* injection molding. The processing procedure is schematically shown in **Figure 47**.

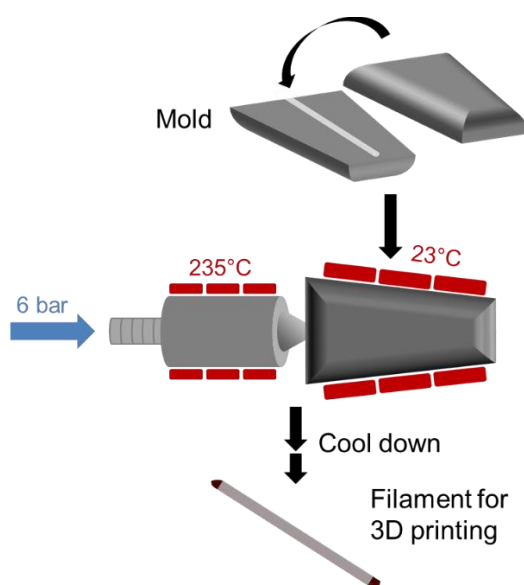


Figure 47: Schematic illustration of the preparation process of filament rods *via* injection molding used for 3D printing. The melt temperature was set to 235 °C and the mold temperature to 23 °C. Injection molding was performed with an injection/holding pressure of 6 bar for 5s.

A special mold designed for the filament rod preparation was used. In addition to the mold, a Teflon[®] tube, with an inner diameter of 3 mm and a length of 140 mm which fits perfectly into the mold, was put inside the mold. The inner diameter of the tube defines the size of the obtained filament rods,

ensures that the $(AB)_n$ segmented copolymer does not adhere to the mold, and guarantees a scarless filament rod. Prior thermal characterizations indicated an optimal melt processing temperature above 200 °C since all synthesized $(AB)_n$ segmented copolymers are in liquid state at this temperature (cf. chapter 3.1.2). Hence, the $(AB)_n$ segmented copolymer was heated to 235 °C and injected into the filament rod mold with a pressure of 6 bar and the pressure was hold for 5s. The mold was kept at 23 °C. After cooling down, the filament was removed from the Teflon® tube by cutting the tube with a sharp razor blade from one end to the other. The filament ends were cut off vertically and the obtained filaments pieces with a length of about 140 mm used for the extrusion-based 3D printing. The 3D printing process and used setup is illustrated in **Figure 48**.

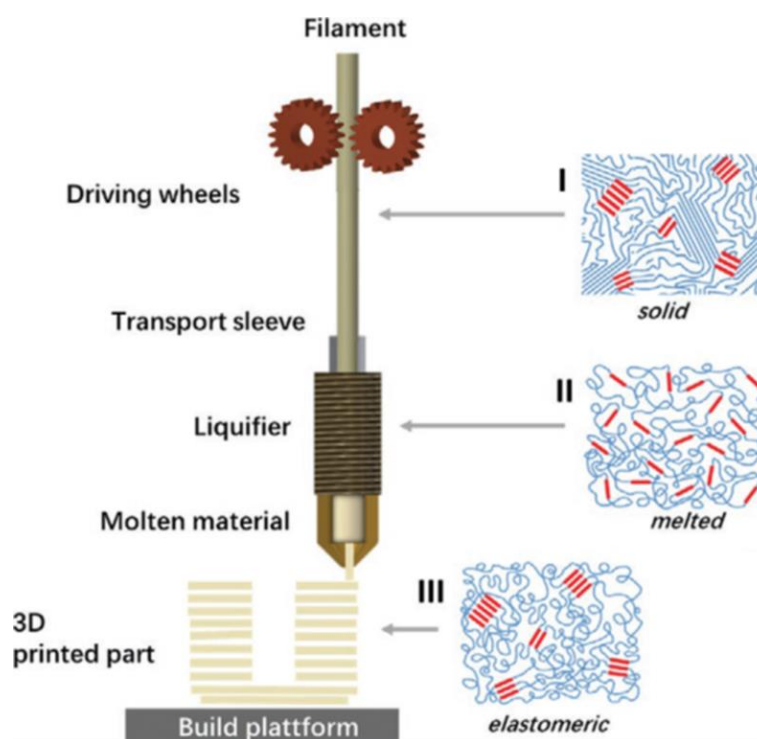


Figure 48: Schematic representation of extrusion-based additive manufacturing process and the different stages of the macromolecular arrangement (I–IV) of investigated $(AB)_n$ segmented copolymers within filament feeding system (solid), liquefier (melt), and in printing of a 3D printed part (elastomeric). Adapted from ^[88].

The $(AB)_n$ segmented copolymer is solid and shows a certain flexibility in the filament state. In the liquefier, the copolymer melts at a temperature above the aggregation temperature of the perylene units. The liquid copolymer can be 3D printed on the substrate in the desired shape programmed by a CAD model. After the movement of the nozzle, the copolymer cools down at the surface of the substrate or before printed part. The copolymer solidifies and forms layer by layer the final 3D printed part. The extrusion-based 3D printing of $(AB)_n$ segmented copolymers does not only allow 3D printing with this copolymer, also 4D printing is demonstrated^[88].

3.1.5 Conclusion of the chapter

In this first chapter, the synthesis of physically crosslinked $(AB)_n$ segmented copolymers with desired thermal and rheological properties *via* solvent-free melt-polycondensation was described. The copolymer consists of two segments: hard segments given by aggregated perylene units and soft segments given by PPO-PEG-PPO units. The perylene units ensure a higher shape stability due to the formation of a physically crosslinked network *via* π - π interactions. The PPO-PEG-PPO units ensure an elastic behavior over a broad temperature range and ensure the lithium ion conductivity necessary for lithium ion battery applications. The synthetic procedure was optimized with respect to reaction temperature and time. Also, the reaction setup was optimized to upscale the synthesis of the copolymers to a multiple gram scale. The thermally-induced reversible stacking behaviors of the perylene units within synthesized copolymers were analyzed. Due to the reversibility of the hardening process, melt-processing of the $(AB)_n$ segmented copolymers is possible. Therefore, the melt-processing parameters were optimized and the melt-processing *via* extrusion-based 3D printing demonstrated. In conclusion, the synthesized $(AB)_n$ segmented copolymers have promising thermal and mechanical properties (c.f. chapter 3.1.3), and hence are suitable candidates as matrix and binder material for lithium ion battery applications.

3.2 Melt-processable solvent-free solid-state electrolyte materials

Lithium ion batteries consist of three major components: anode, electrolyte, and cathode. The sandwich formed thereby is covered by current collectors on both sides which ensure a smooth transport of electrons from one electrode to the other through an external circuit. A schematic setup of a lithium ion battery was presented previously (cf. **Figure 1**).

3.2.1 Thermal characterization of electrolyte material

Before preparing the electrolyte material, the lithium salt (in this work LiTFSI) was investigated in more detail. LiTFSI is a highly hygroscopic material. The water uptake is a big concern for the preparation of lithium ion batteries because water can lead to side reactions in the cell. This can cause safety hazards due to swelling of the battery caused by gas formation. Therefore, the water uptake from LiTFSI was investigated in more detail. LiTFSI salt was kept at 40 °C and at ambient atmosphere. 40 °C was the lowest temperature available while monitoring the water uptake of the material. The weight increase was recorded over time for 90 min and assigned to the water uptake of the specimen. After taking up water, the specimen was heated again with a heating rate of 10 K min⁻¹. The corresponding graph of the water uptake at 40 °C and the graph of the heated specimen afterward are depicted in **Figure 49**.

In **Figure 49 (left)** the weight increase due to water uptake at 40 °C is recorded over time. After 90 min the linear weight increase assigned to the water absorption was measured to be 17%. Remarkably, after 90 minutes of measuring time the maximum water uptake was not reached yet, showing a linear increase up to 90 min. After the measurement time of 90 min, the measurement was stopped. LiTFSI appeared to be completely dissolved after that time, making the immense water uptake visible. After the water uptake measurement, the LiTFSI sample was placed in a TGA crucible and heated with a heating rate of 10 K min⁻¹ up to a temperature of 700 °C (see **Figure 49 (right)**). The first step in the TGA curves can be assigned to the loss of water. The weight loss of this step is roughly 20% which correlates with the weight increase before. At about 400 °C there is a second step correlating with the decomposition of LiTFSI. This thermal analysis shows, that it is beneficial to process LiTFSI at higher temperatures or in a dry atmosphere to avoid water absorption and thus avoid safety issues in the cell.

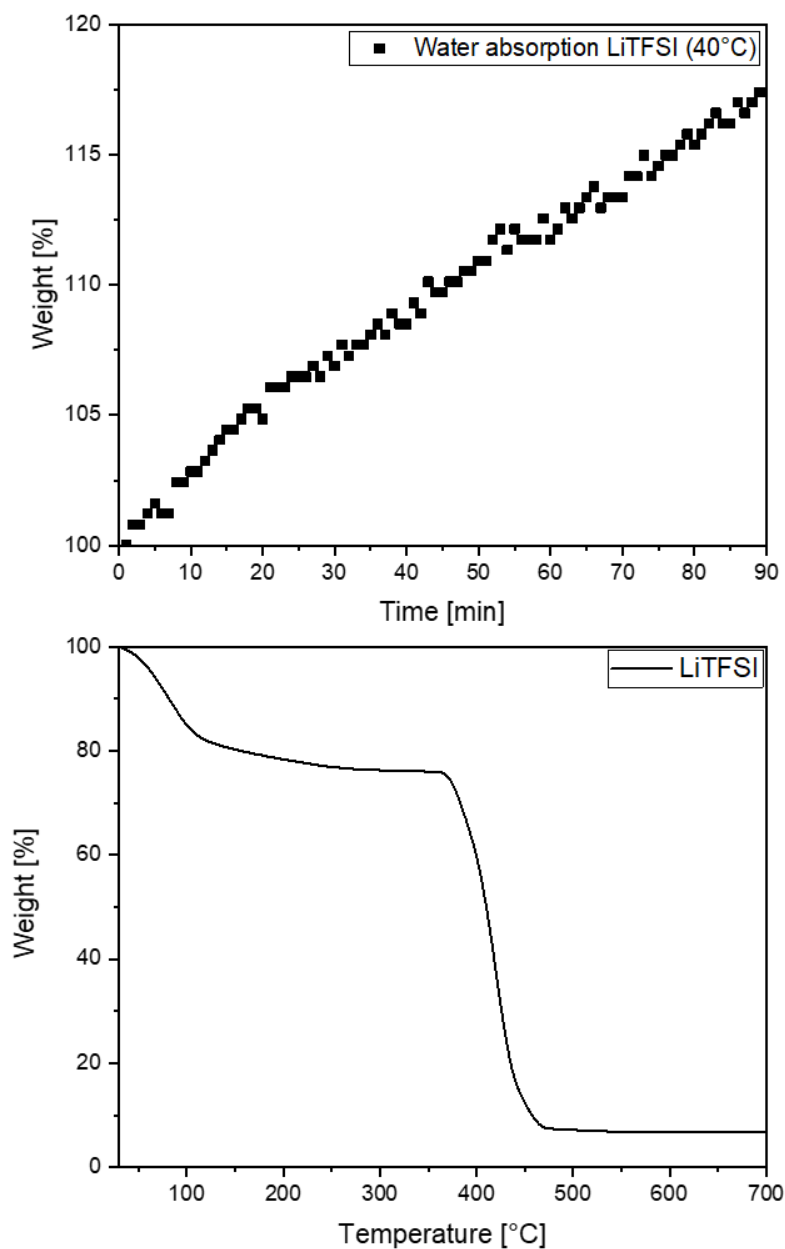


Figure 49: Water uptake (left) and water loss (right) of LiTFSI. After the maximum of measure time, LiTFSI still took up water showing highly hygroscopic behavior. By increasing the temperature, the water can be lost completely. This investigation shows the importance to work at an elevated temperature when using LiTFSI to avoid water uptake in the electrolyte material.

To get a better understanding of the behavior of LiTFSI, the melting point of LiTFSI was measured by DSC. The correlating DSC curves are depicted in **Figure 50**.

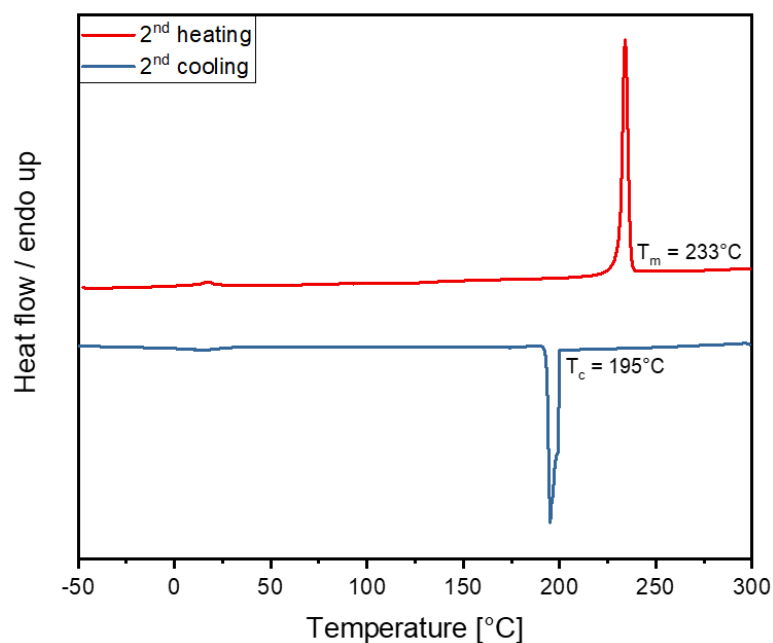


Figure 50: DSC measurement of LiTFSI with heating and cooling rate of 10 K min^{-1} . LiTFSI melts at $233\text{ }^\circ\text{C}$ while it recrystallizes at $195\text{ }^\circ\text{C}$.

LiTFSI melts at $233\text{ }^\circ\text{C}$ and recrystallizes at $195\text{ }^\circ\text{C}$. Based on the DSC measurement and the thermal stability measurements of the neat $(\text{AB})_n$ segmented copolymers (cf. chapter 3.1.2), the preparation and processing parameters of the electrolyte material could be established, allowing a processing of $200\text{ }^\circ\text{C}$. The temperature of $200\text{ }^\circ\text{C}$ was chosen based on the highest melting point of the synthesized $(\text{AB})_n$ segmented copolymer **1a** (PTCDI-Jeff(900)-tBPA) with a melting point of $189\text{ }^\circ\text{C}$ to ensure they are completely molten (cf. **Figure 39**). The thermal stability of LiTFSI allows to be dissolved in the $(\text{AB})_n$ segmented copolymers without risking decomposition.

After analyzing the lithium salt LiTFSI, the electrolyte materials were prepared by mixing the $(\text{AB})_n$ segmented copolymers as matrix material with corresponding amounts of LiTFSI.

As described in Chapter 3.1 $(\text{AB})_n$ segmented copolymers show very good thermal and mechanical properties which makes them suitable materials as matrix materials for solid-state electrolyte materials. The preparation of the electrolyte material mixture was carried out in a Teflon vessel with mechanical stirring under inert conditions. A schematic setup is shown in **Figure 51**.

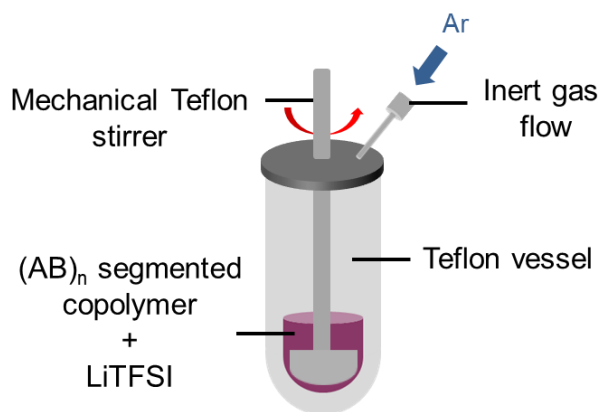


Figure 51: Schematic setup of the mixing vessel used for the electrolyte material preparation. The preparation was carried out under inert conditions using a Teflon vessel with mechanical stirring at 200 °C.

The electrolyte material was stirred for two hours at 200 °C to ensure a homogenous mixture of the (AB)_n-segmented copolymer with the lithium salt. By choosing such an elevated temperature during the electrolyte material preparation, water taken up while setting up the vessel could evaporate out of the electrolyte. Different electrolyte materials with selected lithium salt content were prepared. Hereby, the ratio of oxygen to lithium was varied. The oxygen-to-lithium ratio correlates to the molar ratio of the lithium ions in the salt and the number of ether oxygen atoms in the polymer chain. In the case of Jeffamine-based materials, the number of oxygen atoms correlates with the number of ethylene oxide (EO) units and propylene oxide (PO) units in the copolymer. EO and PO both have one oxygen per unit. The number of lithium atoms per LiTFSI is one, too. The calculation of the [O:Li] ratio is exemplarily shown for **1a** (PTCDI-Jeff(900)-tBPA):

$$[O:Li] = \frac{n_{Copo}}{n_{LiTFSI}} \cdot x \cdot [(y \cdot 1) + (z \cdot 1)] = \frac{n_{Copo}}{n_{LiTFSI}} \cdot 10 \cdot [(6 \cdot 1) + (12,5 \cdot 1)]. \quad (9)$$

x = number of PPO-PEG-PPO repeating units in the copolymer (according to ¹H-NMR); y = number of PO units in Jeffamine ED-900; z = number of EO units in Jeffamine ED-900.

The electrolyte material was used as received, after the mixing procedure, for further measurements and processing steps.

The thermal stability of the electrolyte material was investigated *via* TGA measurements. For lithium ion battery applications, the thermal stability of the materials must be above the working temperature of the battery to ensure safety. A typical maximum working temperature of lithium ion batteries is 60 °C^[95]. In addition to the working temperature of the resulting lithium ion battery, the processing temperature needs to be considered. The thermal stability must exceed the temperatures of the processing steps. Thus, the processing parameters have to be tailored for the corresponding material.

First, the *t*BPA end-capped copolymers were investigated. The corresponding spectra in comparison with the neat (AB)_n segmented copolymer, in this case PTCDI-Jeff(900)-*t*BPA, is shown in **Figure 52**.

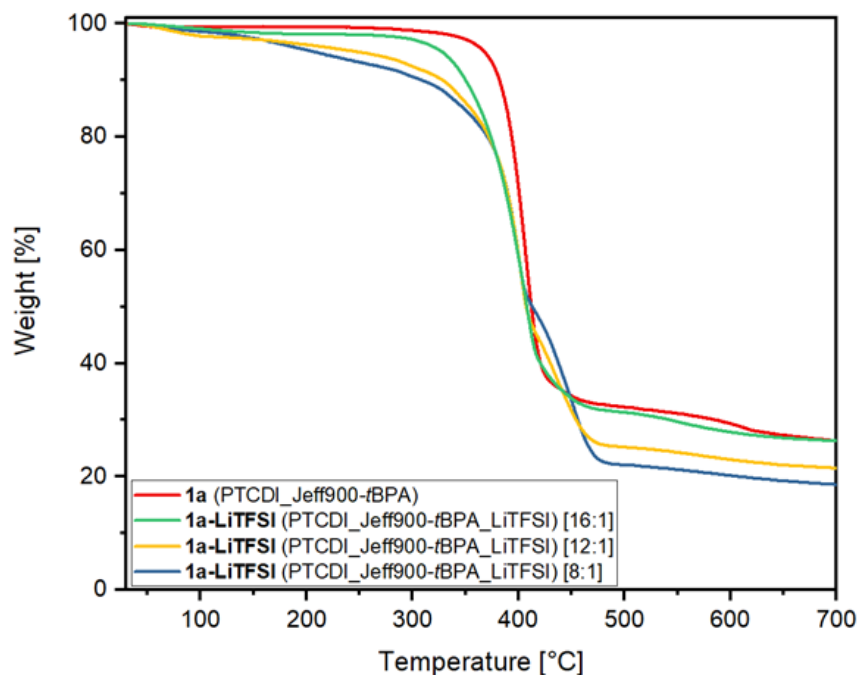


Figure 52: TGA analysis of electrolyte materials based on **1a** (PTCDI-Jeff(900)-*t*BPA). The thermal stabilities of selected mixtures of lithium salt and polymer were investigated. Due to the highly hygroscopic nature of LiTFSI, the electrolyte materials lose water above 100 °C. The decomposition of the electrolyte materials starts at about 350 °C and thus the electrolyte materials show a very high thermal stability.

Figure 52 shows that the electrolyte material is stable to temperatures higher than 200 °C. From about 100 °C until the decomposition temperature of the material at about 350 °C is reached, the electrolyte materials lose weight over time. Recognizably, the slope increases with decreasing [O:Li] ratio. The lower the [O:Li] ratio is, the higher the amount of LiTFSI in the sample. The weight decrease can hereby be explained by the loss of water which the sample taken up until the sample preparation and TGA measurement starting. This phenomenon was already investigated in more detail at the beginning of this chapter.

When the electrolyte material reaches roughly 350 °C the materials start to decompose. Even at 700 °C there is still a char yield remaining. The amount of remaining material decreases with an increasing amount of LiTFSI. This can be explained by the material composition of the electrolyte. The overall mass of perylene decreases when the amount of LiTFSI increases. Therefore, the remaining mass can be mainly assigned to the perylene units. The mass percentage of the remaining mass correlates nicely to the calculated mass of perylene in the electrolyte material. In general, the electrolyte materials are thermally stable until roughly 400 °C without showing any shift, regardless of the LiTFSI content.

To have a closer look at the transition temperatures of the electrolyte materials, dynamic scanning calorimetry (DSC) measurements were conducted. Here, the neat material **1a** (PTCDI-Jeff(900)-*t*BPA) was compared with its corresponding electrolyte material, using a [O:Li] ratio of 12:1. The resulting graph is depicted in **Figure 53**.

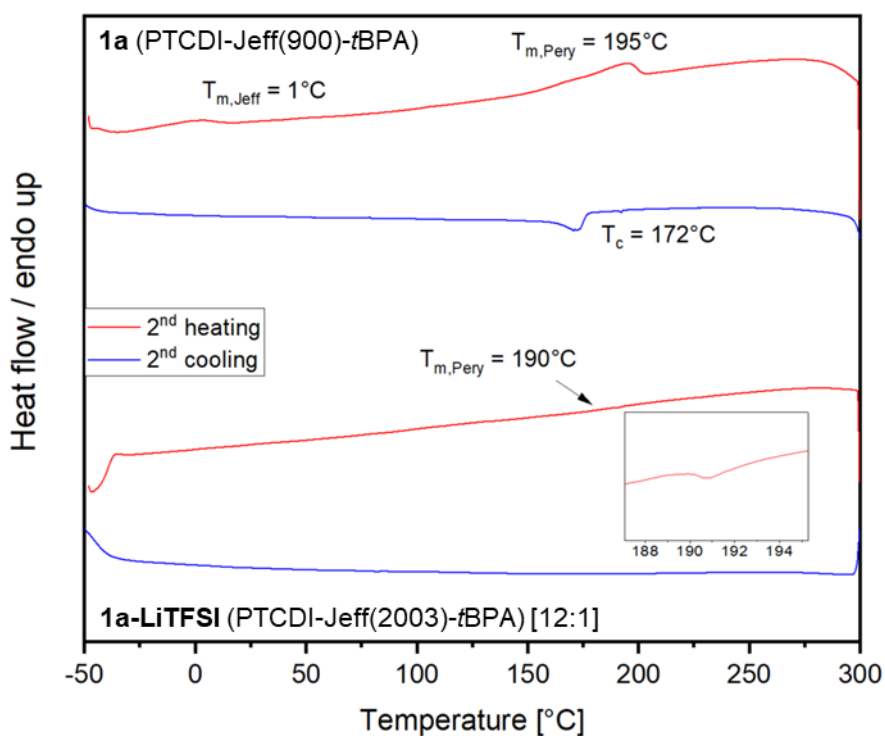


Figure 53: DSC measurement of the neat copolymer **1a** (PTCDI-Jeff(900)-*t*BPA) (top) and the corresponding electrolyte material (bottom). There is a slight shift of the melting temperature of the perylenes towards a lower temperature from the neat copolymer to the electrolyte material. The melting transition temperature during heating and recrystallization temperature during cooling are less visible for the electrolyte material than for the neat copolymer.

Comparing the neat $(\text{AB})_n$ segmented copolymer with the electrolyte material, there is a slight shift of the disaggregation temperature of the perylene units to about 190°C . Notably, the melting peak of the PPO-PEG-PPO segment is vanished completely due to the addition of LiTFSI which acts as plasticizer and suppresses the crystallization of the PPO-PEG-PPO units. Therefore, no melting peak is visible during heating. Above the disaggregation temperature of the perylene units the electrolyte material is in a completely molten state. The DSC characterization was done for the other synthesized *t*BPA-endcapped $(\text{AB})_n$ segmented copolymers accordingly.

After measuring the *t*BPA-endcapped $(\text{AB})_n$ segmented copolymer, the PTCDI-terminated copolymers were characterized *via* DSC measurements as well. Here **2b** (PTCDI-Jeff(2003)-PTCDA) was chosen since this copolymer seemed to be the most promising of the PTCDI-terminated copolymers as electrolyte material given by the melting temperature at about 100°C of the neat copolymer (not

shown here). Secondly, the copolymers based on shorter PPO-PEG-PPO segments could not be synthesized homogeneously since the relative amount of perylene was too high to be able to be dissolved in the corresponding Jeffamine comonomer. Therefore, only the PTCDA-terminated $(AB)_n$ segmented copolymer **2b** (PTCDI-Jeff(2003)-PTCDA) could be synthesized with a homogeneous reaction mixture. The electrolyte material was prepared by adding LiTFSI to the copolymer, as described above. The DSC measurement of the resulting electrolyte material is shown in **Figure 54**.

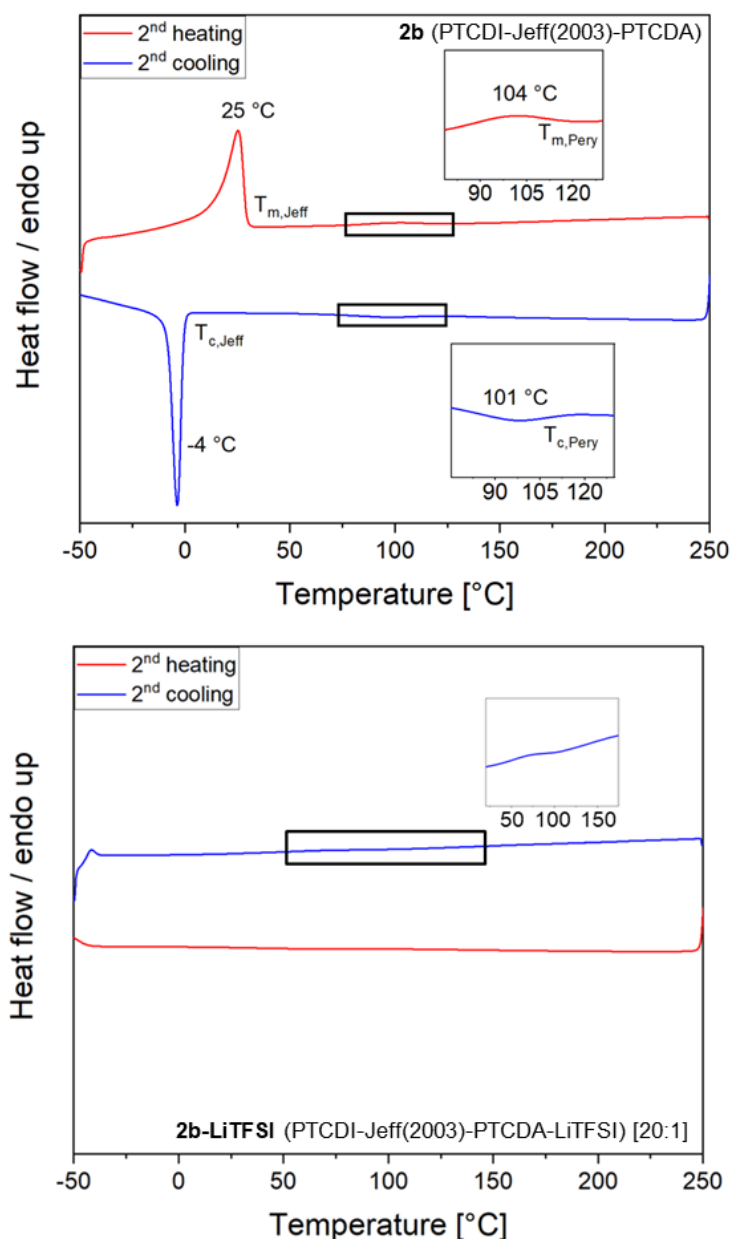


Figure 54: DSC measurement of the neat $(AB)_n$ segmented copolymer **2b** (PTCDI-Jeff(2003)-PTCDA) (left) as well as the electrolyte material **2b-LiTFSI** (PTCDI-Jeff(2003)-PTCDA-LiTFSI) [20:1] (right). For the electrolyte material a transition temperature is hardly visible. By zooming in, the melting temperature of the electrolyte material can be determined at about 77 °C. A crystallization peak of the electrolyte material was not visible in this DSC measurement.

The DSC measurement of **2b-LiTFSI** (PTCDI-Jeff(2003)-PTCDA-LiTFSI) [20:1] displays the effect of the addition of the lithium salt LiTFSI to the neat $(AB)_n$ segmented copolymer, causing the decrease in pronunciation of the crystallization peak, thus suppressing crystallization. The melting temperature of this electrolyte material is hardly visible while it still appears as solid material at room temperature. The perylene disaggregation temperature of the neat copolymer **2b** (PTCDI-Jeff(2003)-PTCDA) sample shifted from 104 °C to 77 °C upon addition of LiTFSI in a 20:1 ratio (**Figure 54**). This shift of 27 °C is larger than for the **1a** (PTCDI-Jeff(900)-*t*PBA) system measured before, where the difference between the **1a** (PTCDI-Jeff(900)-*t*PBA) ($T_{m,pery} = 195$ °C) and the electrolyte **1a-LiTFSI** (PTCDI-Jeff(900)-*t*PBA-LiTFSI) [12:1] ($T_{m,pery} = 190$ °C) was only 5 °C (see **Figure 53**). This can be explained by differences of the matrix material. The relative amount of perylene units of PTCDA-terminated copolymers differs compared to the electrolyte materials based on *t*PBA-encapped copolymers, measured before. This effect of LiTFSI resulting in the suppression of the crystallization seems to be stronger in electrolyte materials based on PTCDA-terminated $(AB)_n$ segmented copolymers. However, a melting point of 77 °C is still sufficient to be used as electrolyte material for all-solid lithium ion batteries. All neat copolymers show a melting temperature of the PPO-PEG-PPO segment. By adding LiTFSI the crystallization of the PPO-PEG-PPO segments are suppressed. In addition to the vanishing of the melting temperature of the PPO-PEG-PPO segment, the melting temperature of the perylene units, which can be so associated with the disaggregation of the stacked perylene units, shifts slightly towards lower temperatures. This can also be assigned to the plasticizing effect of the LiTFSI. An overview of measured thermal transition temperatures by DSC measurements is shown in **Table 6**.

Table 6: Overview of thermal transition temperatures of the synthesized copolymers and corresponding electrolytes.

No.	Polymer	[O:Li]	T _{m,Jeffamine} [°C]	T _{m,Perylene imide} [°C]	T _{c,Perylene imide} [°C]
1a	PTCDI-Jeff(900)- <i>t</i> BPA		1	195	172
1a-LiTFSI	PTCDI-Jeff(900)- <i>t</i> BPA- LiTFSI	[12:1]	-	190	175
1b	PTCDI-Jeff(900/2003)- <i>t</i> BPA ¹		24	166	142
1b-LiTFSI	PTCDI-Jeff(900/2003)- <i>t</i> BPA ¹ -LiTFSI	[12:1]	-	159	119
1c	PTCDI-Jeff(2003)- <i>t</i> BPA		31	95	90
1c-LiTFSI	PTCDI-Jeff(2003)- <i>t</i> BPA- LiTFSI	[12:1]	-	-	-
2b	PTCDI-Jeff(2003)-PCTDA		25	104	101
2b-LiTFSI	PTCDI-Jeff(2003)-PCTDA- LiTFSI	[20:1]	-	77	-

*molar ratio [1:1]

For a more detailed thermal characterization, in addition to the TGA and DSC measurements, dynamic mechanical analysis (DMA) measurements were conducted. In **Figure 55** the DMA curve of the neat (AB)_n segmented copolymer **1a** (PTCDI-Jeff(900)-*t*BPA) is compared to the corresponding electrolyte material. The thermal transition can be detected by plotting the Young's modulus (*E'*) vs the temperature. However, the thermal transition temperatures become more visible by plotting tan(δ) vs temperature as tan(δ) is the derivation of the Young's modulus and therefore the maxima are easier to detect than the inflection points of the Young's modulus. The measurement was conducted using a

frequency of 1 Hz and a heating rate of 2 K min⁻¹. In **Figure 55**, both, the Young's modulus as well as tan(δ) are plotted vs the temperature.

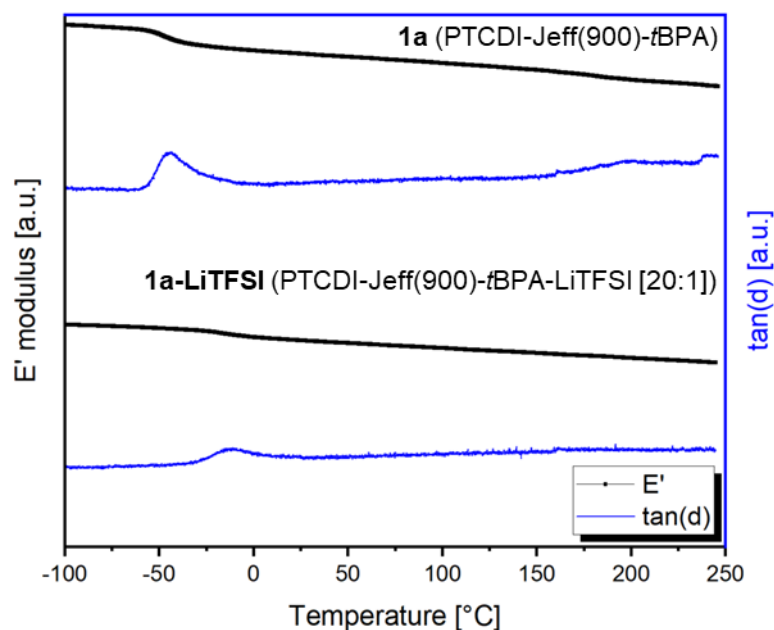


Figure 55: Dynamic mechanical analysis of the neat copolymer **1a** (PTCDI-Jeff(900)-tBPA) and the corresponding electrolyte material using a O:Li ratio of 12:1. While the melting temperature of the neat copolymer is clearly visible, the melting temperature of the electrolyte material is difficult to detect. The glass transition temperature of the PPO-PEG-PPO segments increases due to the coordination of the ether oxygen towards the lithium ions.

The measurement parameters of 1 Hz and 2 K min⁻¹ were used since earlier measurements proved, that these parameters allow a smooth comparison of the DMA temperature values with the DSC temperature values. As shown in **Figure 53**, the disaggregation temperature of the perylene units can be seen at 198 °C for the neat (AB)_n segmented copolymer. However, for the corresponding electrolyte material, there is no transition visible anymore. Since the peak is already hardly visible for the neat copolymer it is expected for the electrolyte material to be less in accordance with the DSC measurements. What can be seen in the DMA measurements compared to the DSC measurements is the T_g of the PPO-PEG-PPO segments in the neat copolymer as well as the electrolyte material. There is a significant difference between the T_g of the PPO-PEG-PPO segments from the neat polymer to the electrolyte material as T_g shifts from -44 °C to -11 °C. This phenomenon can be explained by the coordination of the lithium ions by the PPO-PEG-PPO segments. The coordination of the lithium ions seems to decrease the chain mobility of the PPO-PEG-PPO segments and therefore increases the T_g of the electrolyte material.

3.2.2 Melt-processing of electrolyte materials

In this work, the aforementioned (AB)_n segmented copolymer of Jeffamine and PTCDa, **2b** (PTCDI-Jeff(2003)-PTCDA), was used as matrix material and LiTFSI as lithium salt since it showed good thermal properties being thermally stable up to elevated temperatures higher than 200 °C (cf. chapter 3.2.1). In addition, since the PPO-PEG-PPO segment is responsible for the coordination and transport of the lithium ions it can be assumed, that the higher the relative amount of PPO-PEG-PPO segment in the (AB)_n segmented copolymer the higher the ionic conductivity of the resulting electrolyte material.

Different compositions of the electrolyte materials were prepared by varying the LiTFSI content as well as using different (AB)_n segmented copolymers. An overview of the prepared electrolyte materials is shown in **Table 7**.

Table 7: Overview of the weight percentages of perylene imide units and PPO-PEG-PPO units as well as the lithium salt LiTFSI of the synthesized (AB)_n segmented copolymers.

No.	Polymer [O:Li]	[O:Li]	wt-% [Perylene imides]	wt-% [PPO-PEG-PPO]	wt-% [LiTFSI]
1a-LiTFSI	PTCDI-Jeff(900)-tBPA-LiTFSI	[8:1]	18	46	35
1a-LiTFSI	PTCDI-Jeff(900)-tBPA-LiTFSI	[12:1]	21	53	27
1a-LiTFSI	PTCDI-Jeff(900)-tBPA-LiTFSI	[16:1]	22	56	21
1a-LiTFSI	PTCDI-Jeff(2003)-tBPA-LiTFSI	[8:1]	9	50	41
1a-LiTFSI	PTCDI-Jeff(2003)-tBPA-LiTFSI	[12:1]	10	58	32
1a-LiTFSI	PTCDI-Jeff(2003)-tBPA-LiTFSI	[16:1]	11	63	26
1a-LiTFSI	PTCDI-Jeff(2003)-PTCDA-LiTFSI	[20:1]	15	65	20

Afterwards, the mixture was transferred to either a compression mold or an injection mold setup. Here, the polymer melt was formed into the desired shape for further processing.

For the first investigations of the electrolyte material, compression molding was used, due to its easier handling and quicker sample preparation (see **Figure 56**). Therefore, the hot melt was pressed in-between two perfluoro alkoxy alkane (PFA) films. In-between those films a Teflon spacer with the

desired thickness, which was 500 microns for the first investigations, was put to set the thickness of the pressed electrolyte film. Therefore, the electrolyte material was put in the cavity of this Teflon film. This sandwich was transferred in between two heated plates and pressed for one minute, with minimum pressure, only assuring contact with the outer films and assure the complete melting of the system. Afterward, the film was pressed for four minutes at 200 °C with a pressure of 3 tons. After that, the sandwich was transferred into a cold press allowing it to cool down to room temperature, keeping up a pressure of 7 tons throughout the cooling process. After cooling down the PFA films were fused together to ensure no air contact until they could be transferred into the glove box, where the sample preparation was taken place.

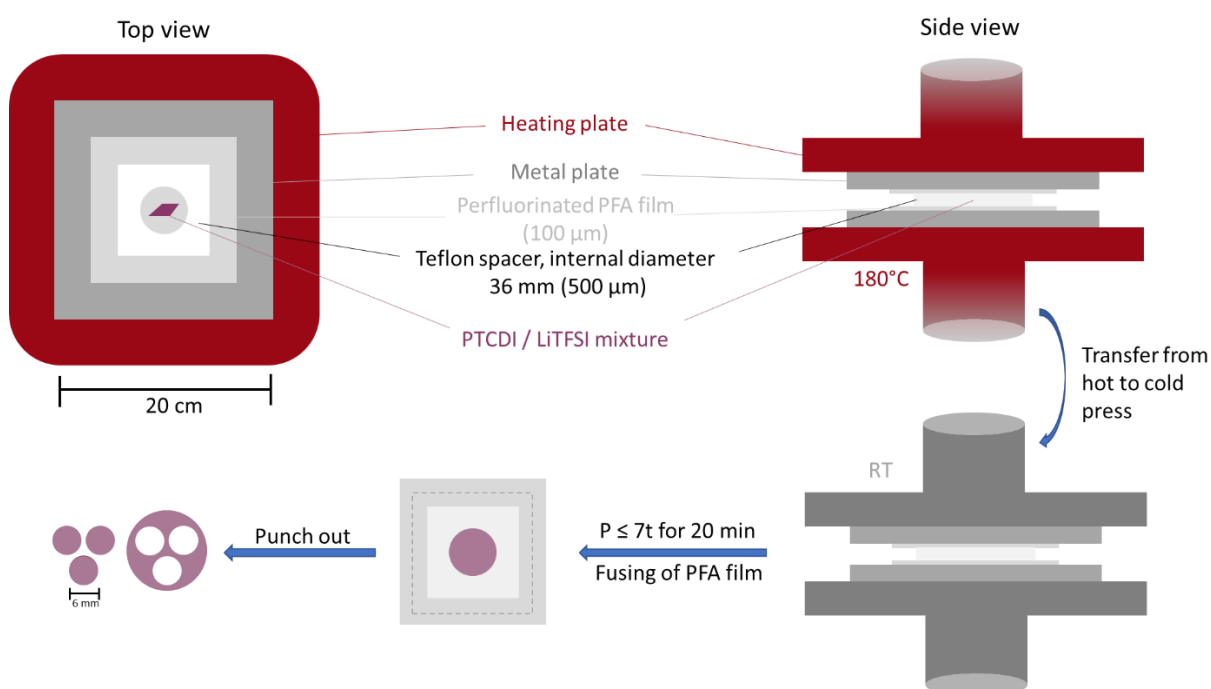


Figure 56: Schematic illustration of the compression film processing used for the characterization of the electrolyte materials. The polymer, mixed with LiTFSI, was processed *via* hot pressing in-between two hot plates. The pressing is shown on the right side. The polymer was inside a round cavity with a diameter of 36 mm and a height of 500 microns realized by a Teflon® spacer between a sandwich of two PFA films of a thickness of 100 microns each. This stack was positioned in-between two metal plates and the sandwich was put into a hot press at temperatures between 180 and 200°C depending on the used polymer. After 5 min, ensuring the polymer was molten, this sandwich was then transferred into a cold press where it was allowed to cool down under pressure to ensure the polymer film keeps its shape. After cooling to about 60 °C the PFA film was fused together to encapsulate the polymer and to ensure no air contact while transferring it to the glove box. There, typically three pieces of the film size needed for the coin cell investigations were punched out of one hot-pressed film.

Inside the glove box, the sample preparation was done the following way. The desired film sizes were punched out of the before-pressed electrolyte film. Afterward, the film was transferred into the corresponding measurement setup correlating to the corresponding cell.

As another method to process the electrolyte material, extrusion-based additive manufacturing or rather 3D printing was chosen. First of all, filaments for 3D printing had to be prepared. Therefore, the $(AB)_n$ segmented copolymer and LiTFSI were mixed in a Teflon mixer for 2 h at 200 °C under a steady argon flow, resulting in a homogenous mixture. The hot melt of the electrolyte material was transferred into a plunger-type injection molding setup. Here the material was formed into filament rods with a diameter of 3 mm and a length of roughly 140 mm. This was accomplished by adding a Teflon tube into the mold with the desired size to ensure smooth removal of the material from the mold, as well as making sure, that the cooled-down sample does not absorb water due to the hygroscopic behavior of the LiTFSI. A mold temperature of 50 °C was selected and the melt was heated up to 130 °C. The optimal pressure during the injection was investigated to be 7 bar. The setup was the same as for the filament processing of the neat $(AB)_n$ segmented copolymers (cf. **Figure 47**)

The resulting filament rods received from the injection molding process were used for the extrusion-based 3D printing process of the electrolyte material. First, the optimal printing parameters needed to be figured out to be able to achieve a homogeneous, thin, well-shaped electrolyte film. The filament feeding was controlled *via* driving wheel controlling the movement speed of the filament, while the transport sleeve ensured a smooth transfer into the liquefier. Investigations showed that the optimal nozzle temperature was 130 °C, allowing a controlled printing of the electrolyte material. At this temperature, the perylene units were not stacked anymore and the material is in the liquid state. This allows the 3D printing of the electrolyte material.

The bed temperature was set to 110 °C, allowing the electrolyte material to cool down slowly. A slow cooling rate allows the perylene units to reassemble efficiently and thus to form strong physical crosslinks. Due to these crosslinks, the material solidifies as elastomeric electrolyte material. By applying at temperature higher than the disaggregation temperature of **2b-LiTFSI** (PTCDI-Jeff(2003)-PTCDA-LiTFSI) [20:1] (cf. **Figure 54**), the polymer did not solidify immediately, allowing the 3D printed surface to become more uniform. In addition, the electrolyte material showed a self-healing effect at the applied temperature ensuring defect-free electrolyte film (see **Figure 57**).

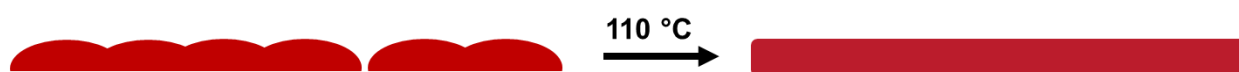


Figure 57: Schematic illustration of the self-healing effect of the 3D printed electrolyte film out of **2b-LiTFSI** (PTCDI-Jeff(2003)-PTCDA-LiTFSI) [20:1].

3.2.3 Electrochemical characterization of electrolyte materials

The electrochemical characterization was realized using a coin cell CR 2032 configuration. For this electrochemical characterization, first the previously prepared electrolytes *via* compression molding based on *t*BPA endcapped (AB)_n segmented copolymers were used. The film was transferred to the glove box and round film pieces were punched out with a diameter of 6 mm and then transferred into the cell setup. The cell setup for ionic conductivity measurements is shown in **Figure 58**.

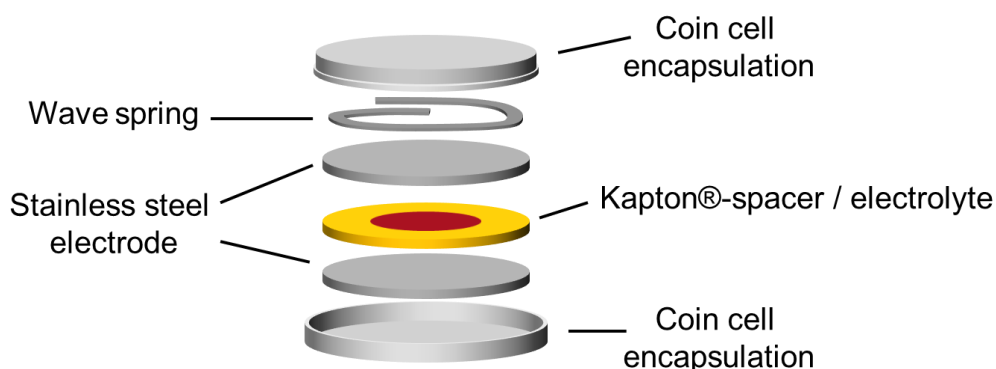


Figure 58: Setup for the ionic conductivity measurement. As electrodes, two stainless steel electrodes are used. In-between there is a Kapton spacer to ensure the thickness of the measured electrolyte to avoid measurement errors. The polymer film fits in the cavity inside the Kapton spacer. After adding a wave spring, the coin cell was encapsulated.

The previously punched-out electrolyte film was put in the cavity of a Kapton spacer. This spacer on the one hand ensures that there is no short circuit of the cell and on the other hand, less material is needed for the characterization steps. The electrolyte was placed in-between two stainless steel electrodes. To ensure there is enough pressure inside the cell, necessary for good contact with the single materials, there is a wave spring included in the cell setup. The whole coin cell setup was encapsulated afterwards using a crimping setup.

The resulting cell was used for potentiostatic electrochemical impedance spectroscopy (PEIS) measurements. Therefore, the imaginary, as well as the real part of the impedance of the cell, was measured at different temperatures from 25 °C to 80 °C. The resulting temperature-dependent Nyquist plot, the imaginary part of the impedance vs the real part of the impedance, is depicted in **Figure 59**.

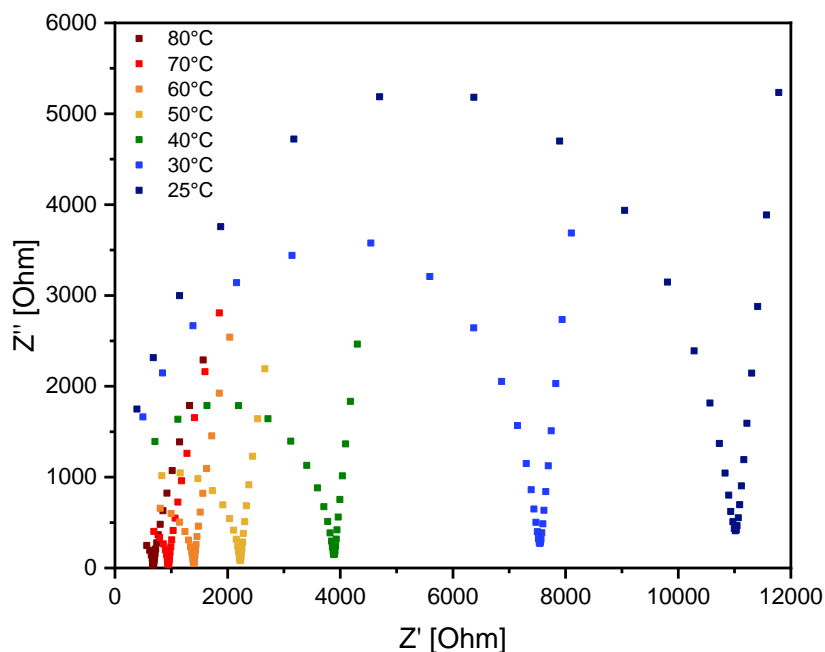


Figure 59: Nyquist plot, the imaginary part of the impedance vs the real part, of the potentiostatic electrochemical impedance spectroscopy (PEIS) measurements of **1b-LiTFSI** (PTCDI-Jeff(900/2003)-tBPA-LiTFSI) [12:1]. From left to right the temperature decreases from 80 °C to 25 °C.

Figure 59 shows the Nyquist plot of 3D printed electrolyte material. From right to left the temperature increases from 25 °C to 80 °C. The maximum of 80 °C was according to commercial solid-state lithium ion battery temperature conditions. The ionic conductivity of the electrolyte material can be calculated as described in Chapter 1, using the values of the real part of impedance at the minima of the imaginary part shown in the Nyquist plot, according to the following equation:

$$\sigma = \frac{d}{A * R_{\Omega}} \quad (10)$$

Here, σ is the ionic conductivity of the electrolyte [S/cm], d the thickness of the electrolyte film [cm], A the contact area of the electrolyte with the corresponding electrodes [cm²] and R_{Ω} the value of the real part at the minimum of the imaginary part of impedance [S⁻¹] taken from the Nyquist plot. PEIS was measured first for all prepared electrolyte materials based on tBPA end-capped (AB)_n segmented copolymers as shown in previous chapters. For the measurements, an oxygen to lithium ratio of 12:1 was used. Based on the PEIS measurements, the ionic conductivities of the electrolyte materials were calculated according to the equation above. The resulting ionic conductivities *versus* the temperatures are shown in **Figure 60**.

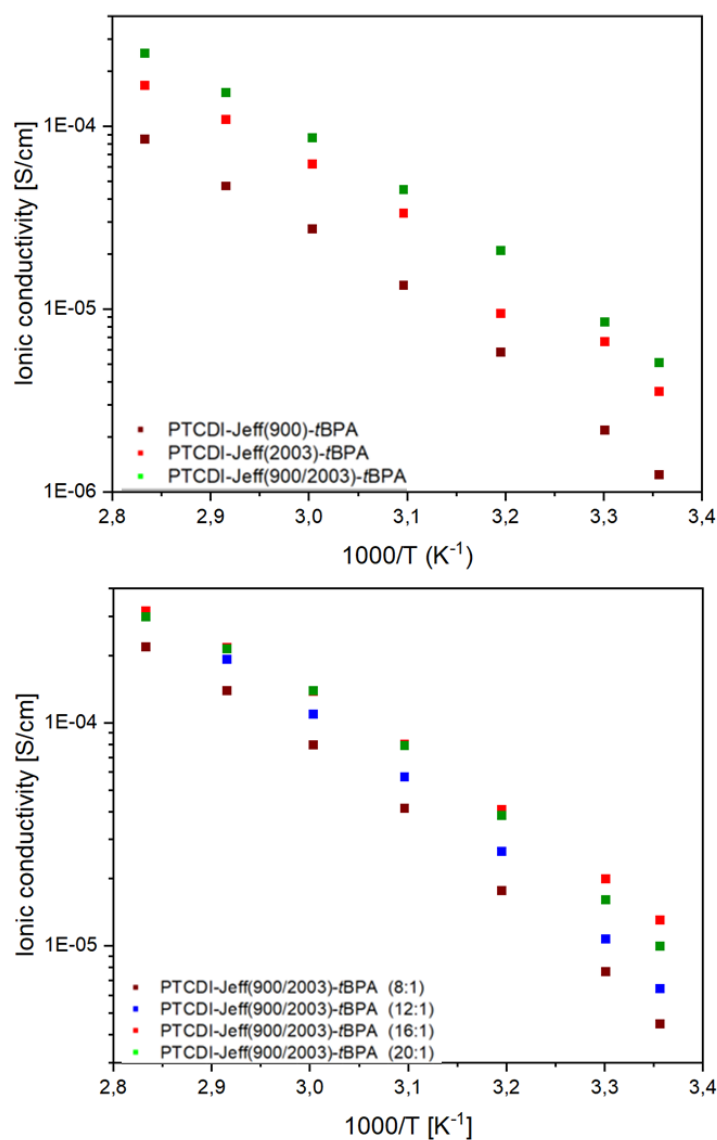


Figure 60: Ionic conductivity measurements. A comparison of the ionic conductivities of the different copolymers (top) and comparing different amounts of lithium salts (bottom). Both graphs show the average value of 3 measurements.

As shown in **Figure 60** (left) the electrolyte materials show slight deviations depending on the $(AB)_n$ segmented copolymer that was used for the preparation. The electrolyte material based on the $(AB)_n$ segmented copolymer based on the 1:1 molar ratio of Jeffamine ED-900 and Jeffamine ED-2003 shows the highest conductivity values (green squares). The mixture of the Jeffamines seems to be beneficial for the lithium ion transport in the resulting electrolyte material. The use of two kinds of chain length might result in less crystals in the electrolyte material and an increased relative amount of amorphous material which improves the ion transport of the electrolyte. Based on the comparison of the different electrolyte materials, the best material was used to investigate the influence of the oxygen to lithium ratio on the ionic conductivity. Therefore, the electrolyte was mixed with different O:Li ratios: 8:1, 12:1, 16:1, and 20:1. The resulting ionic conductivities are shown in **Figure 60** (right). More lithium ions

in the electrolyte material do not mean there is a better lithium ion conductivity. With the increasing amount of Li salt, the material mixture tends to form salt microcrystals which prevent the lithium ion from moving throughout the electrolyte. The measurements showed that the electrolyte materials with an O:Li ratio of 16:1 and 20:1, and with that the lowest amounts of lithium salts, show beneficial ionic conductivities compared to the electrolyte materials with higher amounts of lithium salt.

After initial investigations using electrolyte materials based on *t*BPA end-capped (AB)_n segmented copolymers, the same investigations were made with the PTCD A-terminated (AB)_n segmented copolymer-based electrolyte materials. These electrolyte materials were not prepared *via* compression molding but using extrusion-based 3D printing. However, as described before only the electrolyte based on **2b-LiTFSI** (PTCDI-Jeff(2003)-PTCD A-LiTFSI) [20:1] could be prepared showing a homogeneous mixture of the electrolyte. Since the relative amount of perylene units increases by using PPO-PEG-PPO units with a shorter chain length the solubility of the lithium salt in the (AB)_n segmented copolymers decreases since the PPO-PEG-PPO units are the solubilizing species. As shown in **Figure 60**, the electrolyte materials with an O:Li ratio of 20:1 show promising ionic conductivities using less Li salt than the other investigated electrolyte materials. Therefore, for the PTCD A-terminated copolymer the same O:Li ratio of 20:1 was used to prepare the electrolyte material. A comparison of the electrolyte materials based on *t*BPA end-capped copolymers and the PTCD A-terminated copolymers is shown in **Figure 61**.

2b-LiTFSI (PTCDI-Jeff(2003)-PTCD A-LiTFSI) [20:1] shows improved conductivity at a lower temperature while both electrolyte materials show similar behavior at higher temperatures. However, the reproducibility in the synthesis of the (AB)_n segmented copolymer as well as the electrolyte material preparation of **2b** (PTCDI-Jeff(2003)-PTCD A) is much higher than that of **1b** (PTCDI-Jeff(900/2003)-*t*BPA) since for **2b** (PTCDI-Jeff(2003)-PTCD A) there was no side reaction during the synthesis of the copolymer detectable.

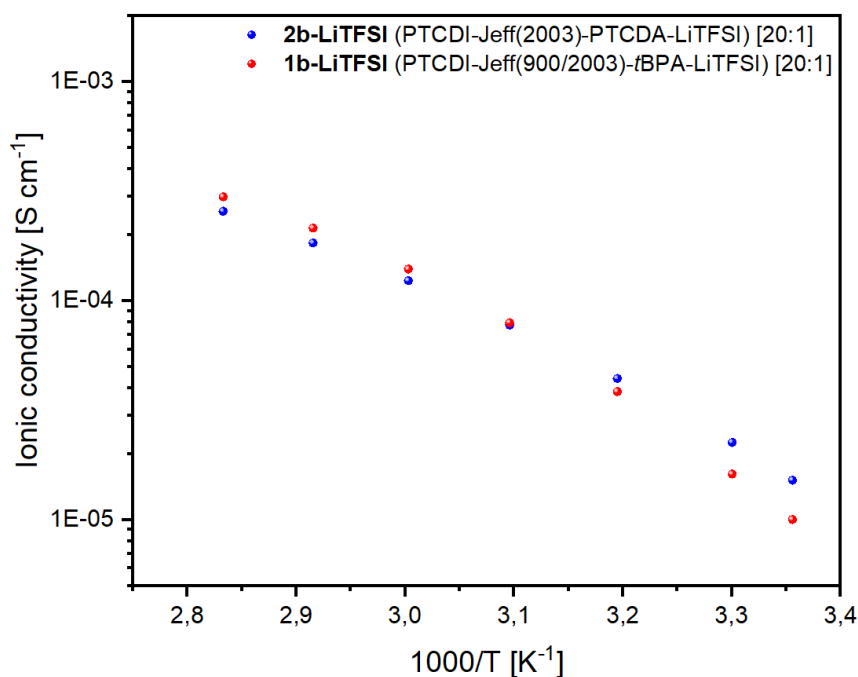


Figure 61: Comparison of the ionic conductivity of the *t*BPA endcapped copolymers with the PTCD A-terminated copolymers. The copolymers were selected due to their similar relative amount of perylene imide units in the overall copolymer.

In addition to the ionic conductivity of the electrolyte material, their electrochemical stability is a major factor for their usability in full lithium ion battery cells. For this purpose, cyclic voltammetry (CV) measurements were conducted. The schematic setup for CV measurements is shown in **Figure 62**.

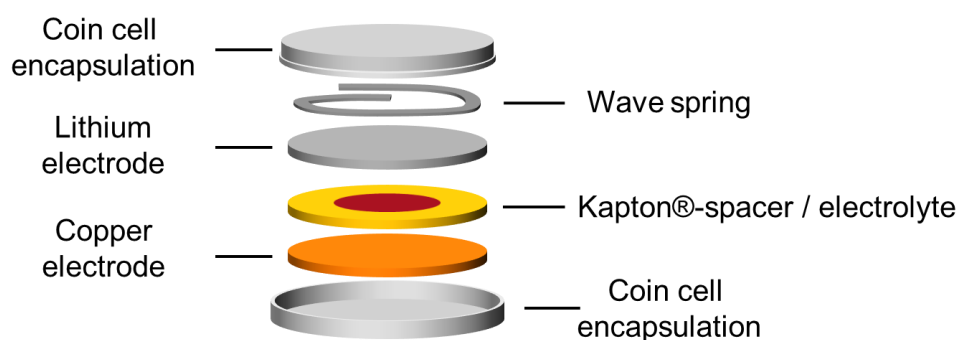


Figure 62: Setup for the cyclic voltammetry measurement. As electrodes lithium and copper are used. In-between there is a Kapton spacer to ensure the thickness of the measured electrolyte to avoid measurement errors. The electrolyte film is placed in the cavity of the Kapton spacer. To ensure contact between the electrodes and the electrolyte a wave spring is added before encapsulation.

The punched-out film was transferred into a Kapton spacer ensuring that there is no short circuit in the system and less material is needed to make more cells for material screening. As electrodes copper and lithium were chosen as they are standard materials in lithium ion batteries because of their redox potentials. Prior to the CV measurement, an open circuit voltage (OCV) measurement was conducted

to verify whether the cell is working. The cell potential there should be around 2.7 V according to the redox potential difference of the selected lithium metal and copper metal electrodes. The prepared cells were measured in the range from -0.5 to 3.7 V. The upper limit was determined by previous test measurements showing a decomposition of the PEG/LiTFSI based compositions starting at voltages higher than 4.0 V. The measurement temperature was set to 70°C to be able to compare values to literature using 70°C as well. The corresponding voltammograms for **1b-LiTFSI** (PTCDI-Jeff(900/2003)-*t*BPA-LiTFSI) [20:1], with the current density on the y-axis and the potential E vs Li/Li⁺ at the x-axis, are shown in **Figure 63**.

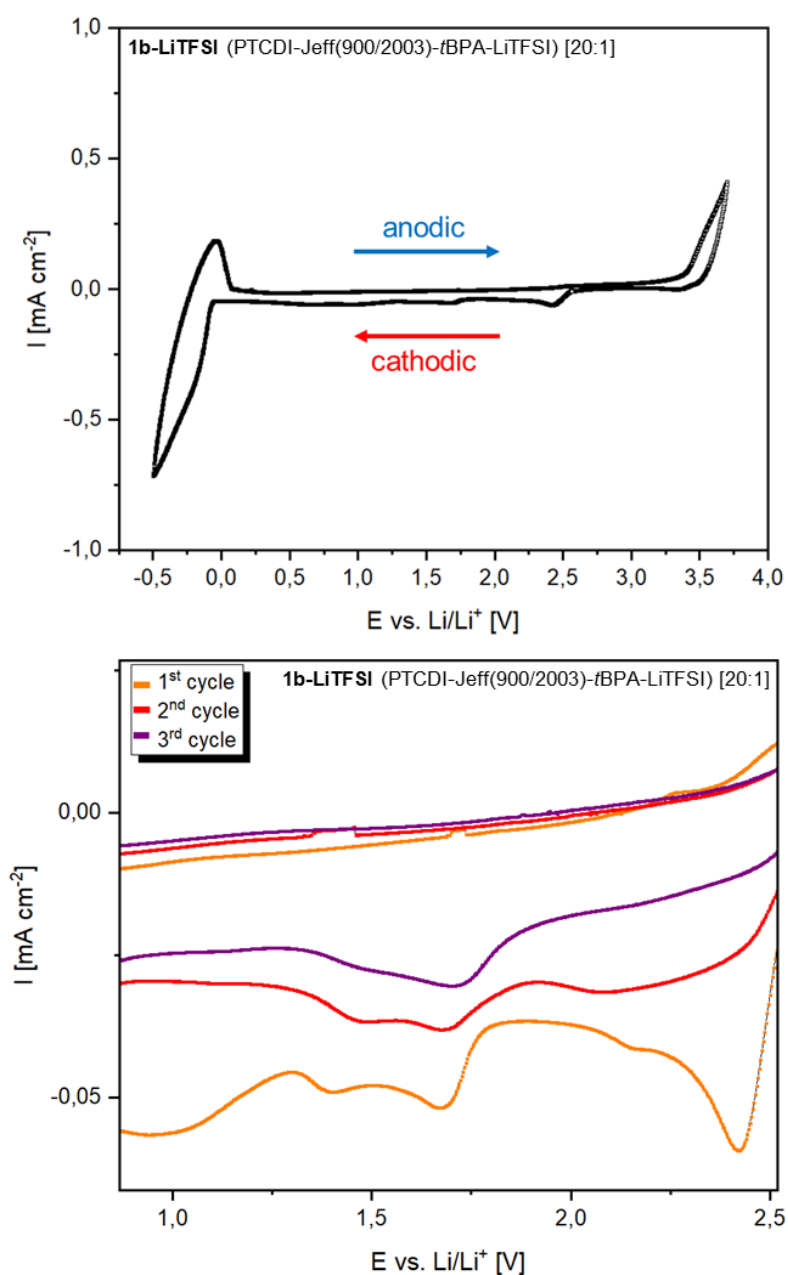


Figure 63: Cyclic voltammetry measurements of **1b-LiTFSI** (PTCDI-Jeff(900/2003)-*t*BPA-LiTFSI) [20:1] using a scan rate of 0.2 mV s⁻¹. On the left the first complete cycle, on the right the development of the first 3 cycles are shown.

The CV voltammogram can be divided into two parts, the anodic part (oxidation process) and the cathodic part (reduction process). The anodic part describes the curve during the charging process (marked in blue), in this case from -0.5 V to 3.7 V. The cathodic part describes the curve during the discharging process (marked in red), in this case from 3.7 V to -0.5 V. At zero potential, the plating and stripping process can be observed. During the negative current, the plating process occurs as lithium ions from the electrolyte are reduced and deposited as Li metal. During the positive current, the stripping process occurs as oxidation takes place and lithium ions are taken up by the electrolyte. The reversibility of this process indicates the lithium ion conductivity of the electrolyte material. Having a closer look between 1 V and 2.5 V potential there is an irreversible reduction peak arising. Therefore, an electrolyte with LiTFSI based on **1b-LiTFSI** (PTCDI-Jeff(900/2003)-*t*BPA-LiTFSI) [20:1] was compared to one based on PEG with a chain length of 2000. The resulting CV curves are depicted in **Figure 64**.

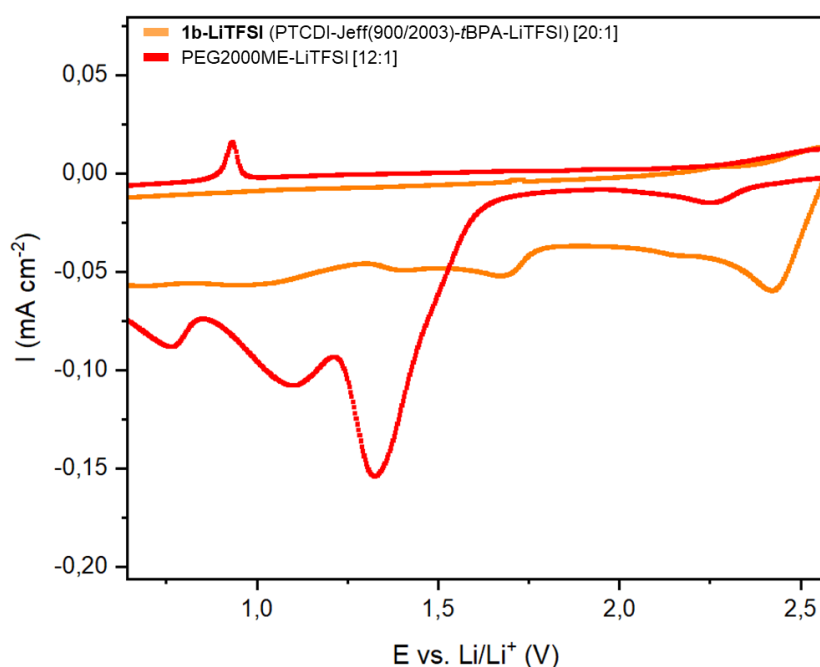


Figure 64: Comparison of cyclic voltammetry measurements of LiTFSI electrolytes based on **1b-LiTFSI** (PTCDI-Jeff(900/2003)-*t*BPA-LiTFSI) [20:1] (orange) and PEG2000ME [12:1] (red).

The copolymer-based electrolyte does not show the irreversible reduction peaks, indicating improved electrochemical stability in this potential range. The smaller reduction peak might therefore arise from the reduction of the perylene imide unit^[92,94].

After the characterization of the *t*BPA endcapped copolymer, the electrolyte material based on the PTCDA-terminated **2b-LiTFSI** (PTCDI-Jeff(2003)-PTCDA-LiTFSI) [20:1] was investigated via CV as well. The full potential range of the measurement comparing the development throughout the first cycles is depicted in **Figure 65**.

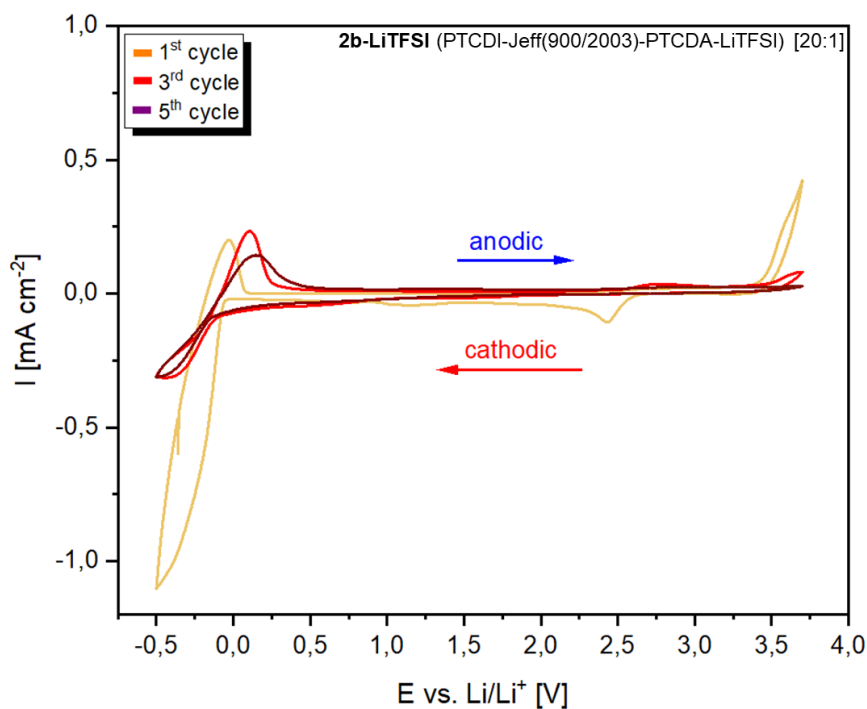


Figure 65: Cyclic voltammetry measurement of the electrolyte material based on LiTFSI and **2b-LiTFSI** (PTCDI-Jeff(900/2003)-PTCDA-LiTFSI) [20:1]. The development of the cyclic voltammetric behavior is shown with an increasing number of cycles. The reduction peak at about 2.5V vanishes with an increasing number of cycles.

The CV measurement of **2b-LiTFSI** (PTCDI-Jeff(2003)-PTCDA-LiTFSI) [20:1] shows a similar behavior as its *t*BPA endcapped polymer. At about 0 V the lithium plating and stripping process enabled by the electrolyte material is clearly visible. The reversibility of this process proves that the electrolyte material is capable of lithium ion transport. During the first cycle, there is a reduction peak at about 2.5 V visible. A more detailed visualization of this reduction peak is shown in **Figure 66**.

With an increasing number of cycles, the reduction peak vanishes, showing that there is no side reaction detectable after the first 5 cycles. Thus, this experiment could prove the electrochemical stability of the electrolyte material making it a suitable candidate as electrolyte material in lithium ion battery applications.

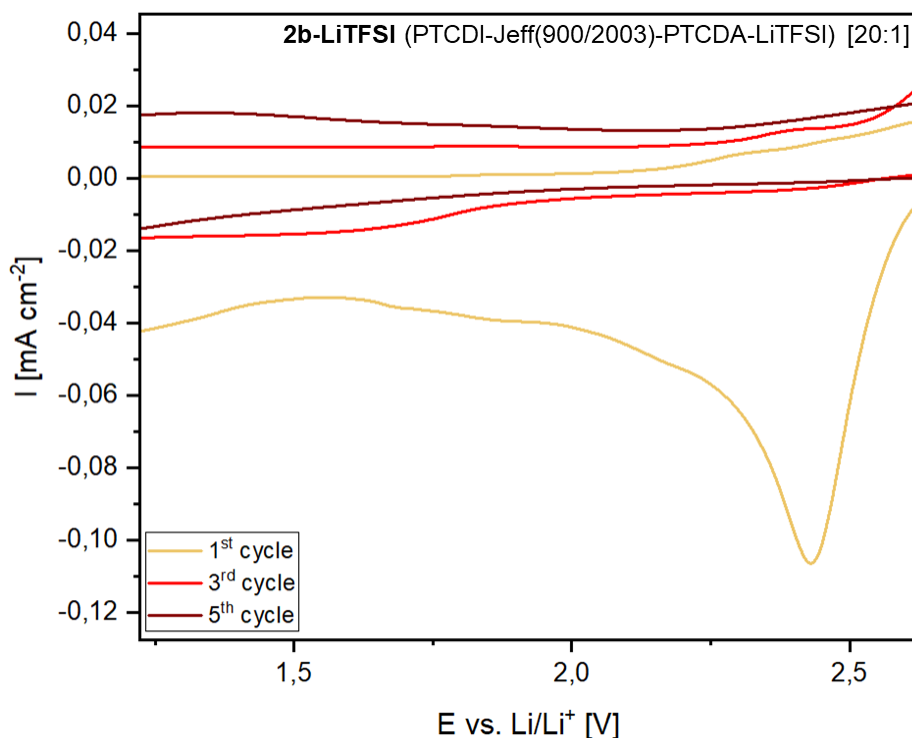


Figure 66: Zoom-in of the CV measurement of the electrolyte material based on LiTFSI and **2b-LiTFSI** (PTCDI-Jeff(2003)-PTCDA-LiTFSI) [20:1]. The development of the cyclic voltammetric behavior is shown with an increasing number of cycles. The reduction peak at about 2.5V vanishes with an increasing number of cycles.

The before-mentioned plating/stripping process is a very important process in a lithium metal battery which is why further investigations were made to look into this process. For this purpose, symmetric lithium cells with the electrolyte in-between two lithium electrodes were prepared to investigate this behavior. The schematic cell setup is shown in **Figure 67**.

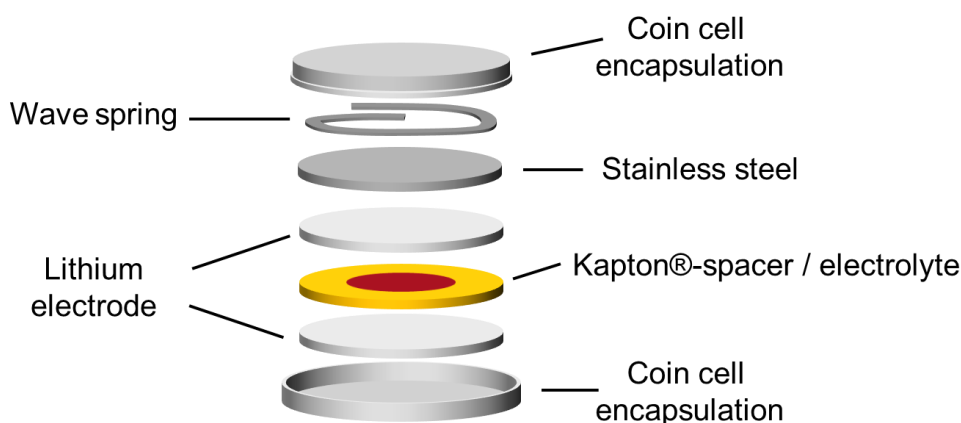


Figure 67: Setup used for lithium plating/stripping investigations. As electrodes lithium was used on both sides of the electrolyte. In-between, there is a Kapton spacer to ensure the thickness of the measured electrolyte to avoid measurement errors. The electrolyte film is placed in the cavity of the Kapton spacer. To ensure contact between the electrodes and the electrolyte a wave spring is added before encapsulation.

To further investigate the plating/stripping process the symmetric cells were cycled around the zero potential, to enforce the plating/stripping process as described in the CV measurements above. Changes over time or cycles can indicate changes in the material itself or its environment. For the first investigations, a 130 μm thick film of **1b-LiTFSI** (PTCDI-Jeff(900/2003)-tBPA-LiTFSI) [20:1] was prepared *via* compression molding and used to measure plating/stripping experiments. These cells were measured using a constant current density of 0.1 mA cm^{-2} while recording the voltage over time. Every 5 cycles a PEIS measurement was conducted to investigate the change of impedance throughout the plating/stripping experiment. The potential E vs the number of cycles for the plating/stripping measurement is plotted in **Figure 68**.

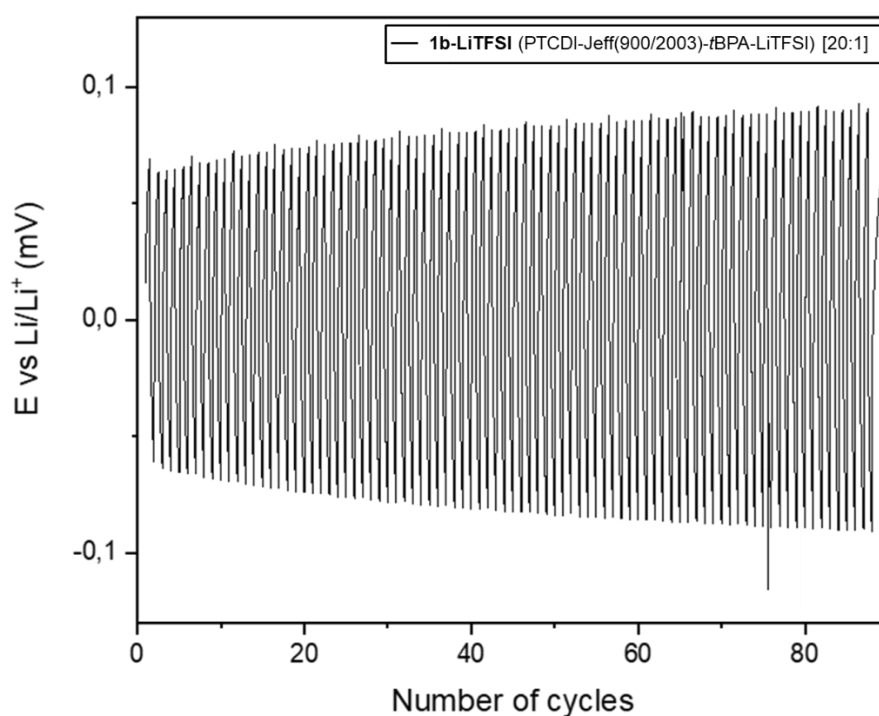


Figure 68: Plating and stripping process investigations of the electrolyte based on LiTFSI and **1b-LiTFSI** (PTCDI-Jeff(900/2003)-tBPA-LiTFSI) [20:1] measured at $70 \text{ }^\circ\text{C}$. The potential is plotted over the number of cycles. The observed overpotential can be assigned to the formation of the SEI.

Figure 68 shows the plating and stripping process of the electrolyte material based on LiTFSI and **1b-LiTFSI** (PTCDI-Jeff(900/2003)-tBPA-LiTFSI) [20:1]. For easier visualization of the potential measured with an increasing number of cycles, the maximum of the potential was plotted versus the number of cycles in **Figure 69**.

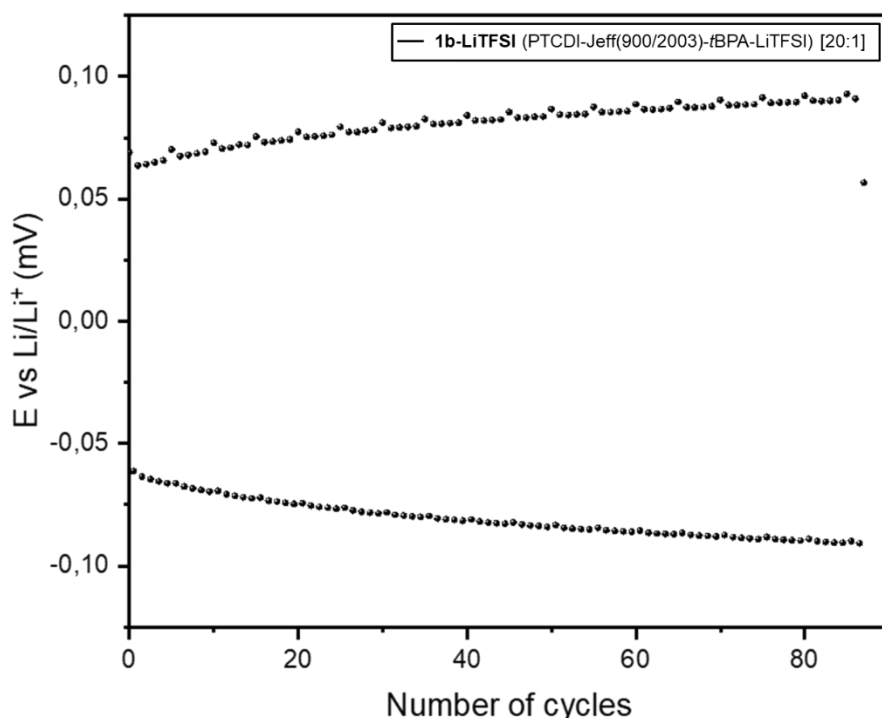


Figure 69: Plating and stripping process investigations of the electrolyte material **1b-LiTFSI** (PTCDI-Jeff(900/2003)-tBPA-LiTFSI) [20:1] measured at 70 °C. The maxima of the potential of each cycle is plotted over the total number of cycles. The overpotential, the increase of potential with increasing number of cycles, can be assigned to the formation of the SEI.

The overpotential increases with the number of cycles. This can be ascribed to the formation of the solid-electrolyte interface (SEI), which results from the decomposition of the electrolyte material at a certain potential, a common phenomenon in electrolyte research^[96]. The SEI forms a thin layer on the electrode surface which increases the resistance of the electrode towards lithium ion transport, reflected by the increase of the overpotential. However, after several cycles, the increase of the potential reaches a plateau where the electrolyte stays stable over time. Every cycle equals 10h each of charge and discharge. So, the electrolyte is stable for at least 85. In this experiment, the electrolyte film from the compression molding process was used, with a thickness of about 150 microns. However, the aim is to achieve as thin electrolyte films as possible while fulfilling the mechanical, thermal, and electrochemical requirements. Thus, the plating and stripping measurement was repeated with a 3D printed film whose thickness could be set to 50 microns.

For this purpose, the optimal scenario would be to print the electrolyte material directly on top of the lithium electrode. However, pure lithium is not a suitable 3D printing build surface because it is highly reactive with air and moisture, and therefore not suitable for applications outside of an inert atmosphere. To be able to transfer a thin electrolyte film from the 3D printing setup into the glove box for further preparation a suitable transfer process had to be established. The electrolyte film was printed onto a PTFE film but it turned out too thin to be removed from the carrier substrate, impeding

the reproducibility of the process. In an improved approach, a PFA film as support material was prepared by punching out a film with an inner diameter of 14 mm and an outer diameter of 16 mm. This support substrate was placed around the glass fiber reinforced PTFE foil. The electrolyte was now printed with a diameter of 15 mm partially covering the PFA support structure. The setup before and after the 3D printing process is schematically depicted in **Figure 70**.

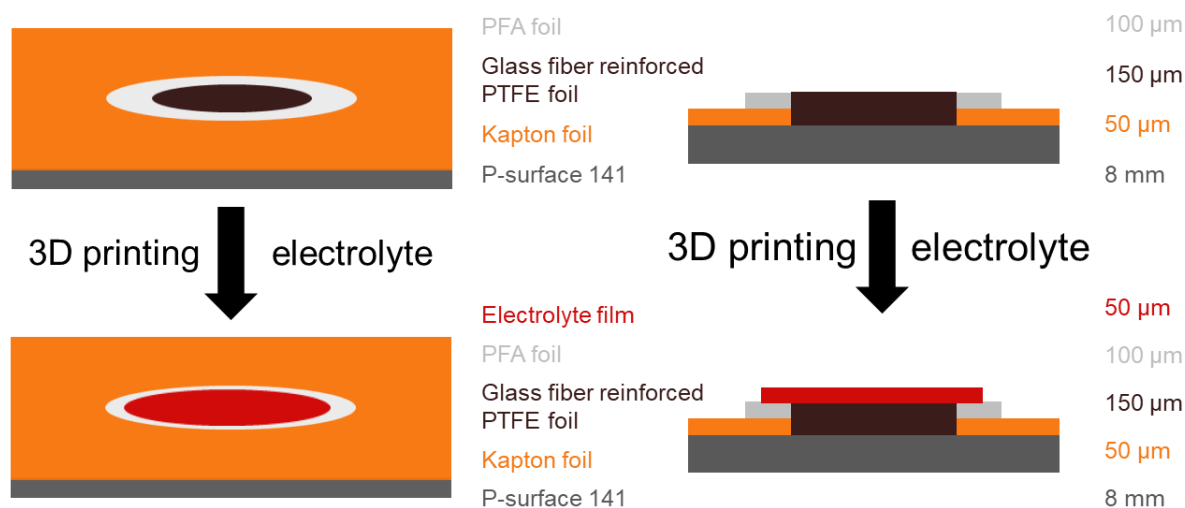


Figure 70: Schematic drawing of the extrusion-based 3D printing process of the electrolyte material and the corresponding thicknesses. Because of the self-adhesive properties of P-surface 141, the Kapton foil and glass fiber reinforced PTFE foil was placed on it. The punched-out opening in the center of the Kapton foil marked the exact position. A PFA foil was added around this opening in the Kapton foil. On top of the glass fiber reinforced PTFE foil the electrolyte was 3D printed with a diameter increased to 1.05 mm. After 3D printing, the electrolyte film was lifted off together with the glass fiber reinforced PTFE foil and the PFA foil. The PTFE foil served as transfer layer and the PFA foil served as supporting layer during the transfer from the PTFE foil onto the desired substrate.

Figure 70 illustrates the setup before the printing (top) and including the final electrolyte film (bottom). The electrolyte film was able to be transferred with the outer PFA foil ring and the PTFE foil below the electrolyte as support structures. In the glove box, the PTFE foil was removed leaving the PFA foil as a support substrate. This procedure allowed the transfer of the film to any kind of substrate with a diameter of 14 mm or below. After transferring the electrolyte film onto the lithium foil, the PFA support structure can be easily removed leaving the electrolyte on the lithium foil. On top of the electrolyte film, the second electrode can be easily placed, in the case of the plating/stripping process another lithium foil. This way the measurement of thin films was enabled and the following measurement cells were prepared *via* this processing route. The resulting cells were used to investigate the plating and stripping behavior of the 3D printed electrolyte material **2b-LiTFSI** (PTCDI-Jeff(2003)-PTCDA-LiTFSI) [20:1]. **2b-LiTFSI** (PTCDI-Jeff(2003)-PTCDA-LiTFSI) [20:1] was used instead of **1b-LiTFSI** (PTCDI-Jeff(900/2003)-tBPA-LiTFSI) [20:1] because of the improved synthesis of the $(\text{AB})_n$

segmented copolymer (cf. Chapter 3.1.1) as well as electrochemical properties (cf. Chapter 3.2.3). The resulting graph of **2b-LiTFSI** (PTCDI-Jeff(2003)-PTCDA-LiTFSI) [20:1] is shown in **Figure 71**.

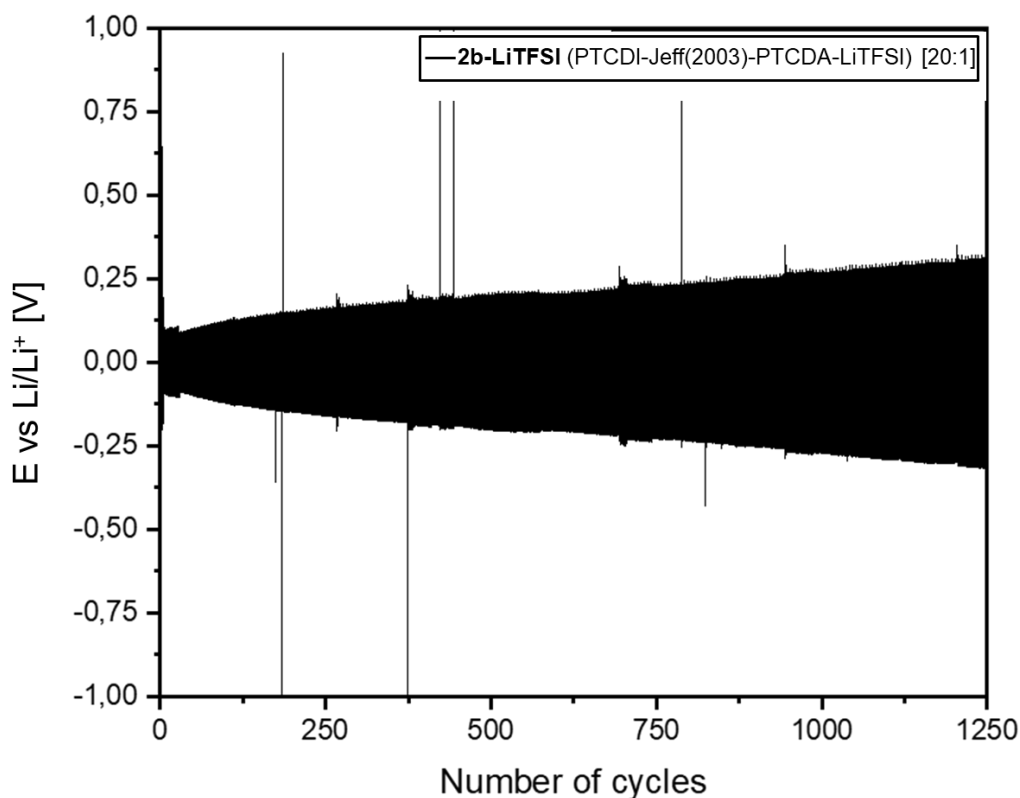


Figure 71: Plating and stripping process investigations based on **2b-LiTFSI** (PTCDI-Jeff(2003)-PTCDA-LiTFSI) [20:1] with a thickness of 50 microns measured at 70°C. The potential of the coin cells was measured over the number of cycles. The increase of the overpotential for the first cycles can be assigned to the formation of the SEI, and the spikes of the potential can be assigned to soft short circuits, however without short circuiting the cell. Over a large number of cycles, the internal resistance of the coin cell slightly increases which is a normal behavior in the field of lithium ion batteries.

The lithium plating and stripping measurement of **2b-LiTFSI** (PTCDI-Jeff(2003)-PTCDA-LiTFSI) [20:1] shows a thermal, mechanical and electrochemical stability of the electrolyte material for more than 1200 cycles. The increase of the potential with an increasing number of cycles can be assigned to an increase in internal resistance and the potential spikes during the measurement can be assigned to soft short circuits. However, no short circuiting of the cell could be observed. The stability of the electrolyte material for more than 1230 cycles at 70 °C demonstrates the outstanding performance of this solid-state lithium ion battery electrolyte material. This number of cycles in addition to the used temperature of 70 °C is already in the range of industrially used lithium ion batteries. This outstanding performance proves that the solid-state electrolyte material based on $(AB)_n$ segmented copolymer can prevent the formation of dendrites respectively ensure no short-circuiting of the cell for at least 1250 cycles, which is a very promising value in the uprising field of all-solid lithium ion batteries.

3.2.4 Conclusion of the chapter

This chapter focused on the preparation and processing of novel solvent-free solid-state lithium ion battery electrolytes. These electrolytes are easily processable using common melt-processing techniques like compression molding or extrusion-based 3D printing. The thermal and electrochemical stability allows the use in common lithium ion batteries. The lithium ion conductivity was measured *via* PEIS investigations leading to a maximum ionic conductivity of $2 \cdot 10^{-4} \text{ S cm}^{-1}$ (80 °C). The mechanical stability of the electrolyte material allows a new setup for lithium ion batteries, enabling the use of pure lithium metal as anode material by impeding cell failure during plating and stripping experiments. The measurement reached 1250 cycles which is a promising number, making this material interesting for industrial all-solid-state lithium ion battery applications. Nowadays commercially used full lithium ion batteries are usually used for 1000 cycles depending on the electrode materials. This promising performance in terms of mechanical, thermal, and electrochemical stability in addition to the easy processing could enable new ways in lithium ion battery fabrication processes.

3.3 Melt-processable solid-state cathode materials

After the preparation, processing, and optimization of the electrolyte material, a suitable cathode material was developed. A composite cathode consists of three major components to be able to be used in a lithium ion battery setup cf. **Figure 72**.

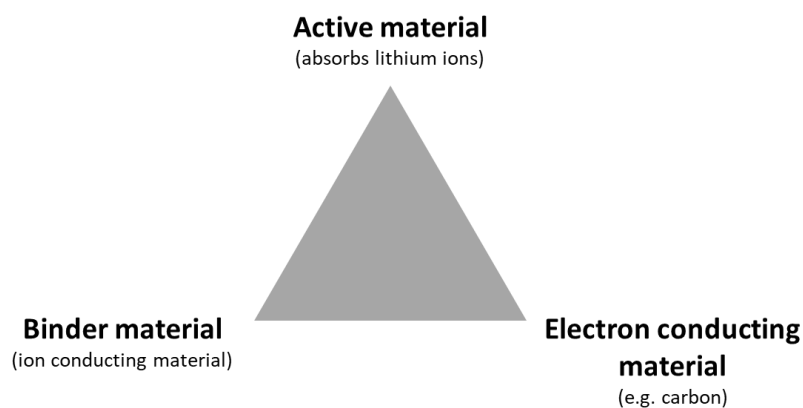


Figure 72: Chemical triangle of components necessary for a composite cathode for use in lithium ion battery applications.

The most important material component is the active material which is responsible for the absorption and desorption of lithium ions. Common cathode active materials are lithium intercalating materials such as transition metal oxides e.g. LCO where lithium ions get intercalated into the lattice. A cheaper alternative can be LFP because iron is much cheaper compensating for less energy density compared to LCO. The materials differ in their thermal, chemical, and physical properties. As a second component, is the electron-conducting material, which is a necessary additive as the active materials themselves do typically not provide sufficient conductivity. Suitable materials are carbon-based materials like graphite, graphene, or carbon black *etc.* which show a very high electron conductivity. The addition of these materials decreases the overall percentage of active material in the cathode, which is why a minimum amount of additive is preferred to keep the percentage of the active material as high as possible. To achieve a homogenous mixture of the cathode composite material the use of the third component is mandatory which is a binder material. The binder material ensures the contact of the active material and the electron conducting material, as well as smooth lithium ion transport throughout the whole cathode material. For the binder material apply the same as for the electron-conducting material, the less necessary the better. In this work, LFP was chosen as active material due to its overall performance as well as its price-performance ratio. As binder material the previously synthesized $(AB)_n$ segmented copolymer used, showing promising ion conducting abilities as well as mechanical stability while proving to be easily processable. As electron-conducting material graphene was selected due to its amazing properties such as outstanding electron conduction, and mechanical,

chemical, and thermal stability. However, high-quality graphene is extremely expensive as well as not very reliable on the quality and very difficult to source, so it was decided to synthesize graphene in this work as well. There are several different methods to synthesize graphene, like exfoliation, chemical vapor deposition (CVD), *etc.* The highest quality graphene is available using CVD, so this method was chosen to synthesize graphene.

3.3.1 Synthesis and characterization of graphene via chemical vapor deposition

There are several different ways to synthesize graphene *via* CVD depending on the starting material as well as the catalyst chosen and the processing procedure. As catalysts mainly two different materials are used commonly which are the transition metals nickel and copper. The differences in terms of reaction mechanisms were already discussed in Chapter 1.4.4. As a promising candidate nickel was selected to be the catalyst used for the graphene synthesis. Hydrogen gas was not available in the CVD setup used for this investigation. For that reason, a different synthetic route was chosen inspired by Kulkarni *et al.*^[97] showing a synthesis starting with aromatic compounds.

During CVD the carbon source gets evaporated onto a heated nickel foil under high vacuum. The nickel foil needs a sufficient temperature enabling the decomposition of the carbon source into elemental carbon and elemental hydrogen. The hydrogen can reduce nickel oxide on the nickel foil surface enabling the carbon to dissolve into the nickel. Upon cooling down the nickel foil to a specific temperature, the carbon atoms move on the nickel surface to build graphene sheets there. After cooling down to room temperature the reaction shall result in graphene coated nickel foil. The here discussed setup is shown schematically (left) as well as in a photograph of the CVD chamber (right) in **Figure 73**.

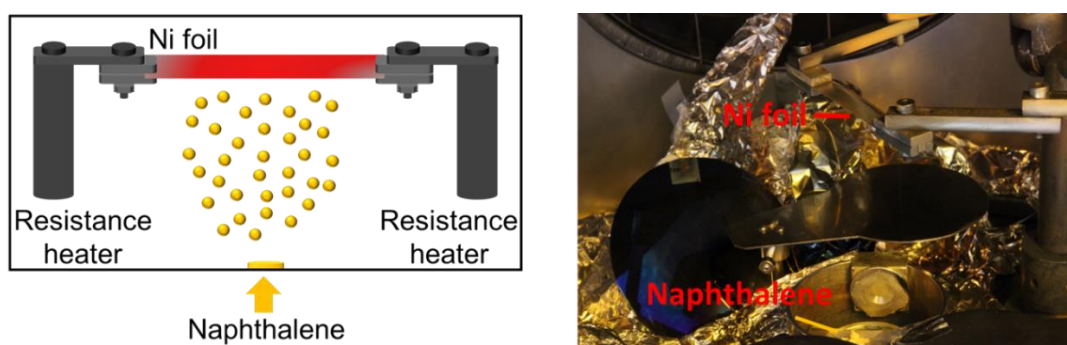


Figure 73: Schematic sketch of the CVD setup (**left**) and a picture of the used setup (**right**). As a catalyst and carrier film, a Ni foil was used and heated in-between two resistance heaters to temperatures between 700 and 1000°C. Here a naphthalene reservoir was used as a carbon source. The naphthalene evaporates during the heating of the Ni foil and was not actively heated.

The nickel foil was heated up by a resistance heater. Since the temperature of the resistance heater depends on the used material a calibration of the temperature needed to be done to ensure setting a

defined temperature during the CVD process. Materials with different melting temperatures were systematically selected to enable the calibration of the setup. The melting temperature is not affected by vacuum which is why high melting materials such as salts or metals themselves were used to determine the melting temperature and therefore set the corresponding level of the resistance heater. The corresponding calibration curve in addition to the correlated materials is shown in **Figure 74**.

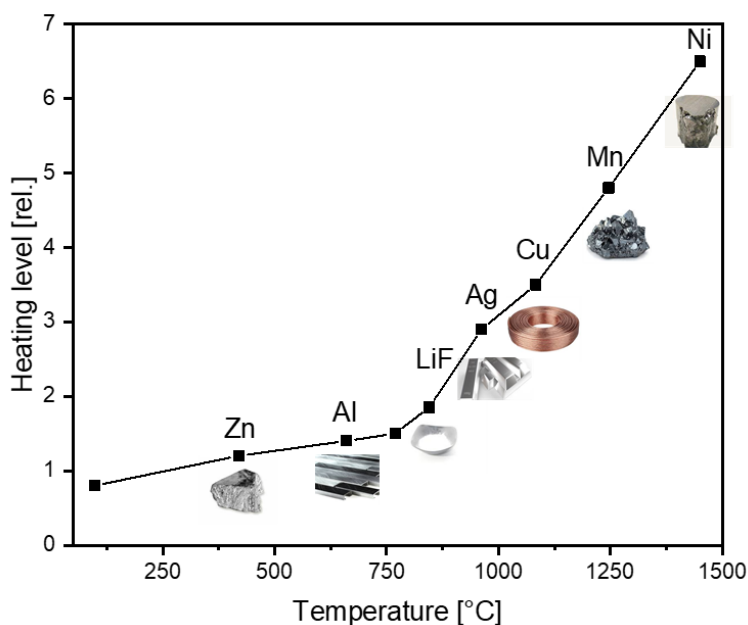


Figure 74: Calibration curve to set the temperature of the nickel foil used in CVD process. Therefore, different materials were melted on top of the nickel foil under vacuum inside the reaction chamber. The resulting melting temperature was monitored in relation to the corresponding heating level of the controller used to heat up the nickel foil.

After calibrating the setup, the first experiments were realized. As a carbon source naphthalene was chosen, inspired by Kulkarni *et al.*^[97]. They drop cast a nanomolar solution of naphthalene in chloroform onto the nickel foil and heated it up afterwards, to receive graphene sheets on the nickel foil after cooling down to room temperature. In this work, three different kinds of aromatic materials were investigated: naphthalene, perylene, and coronene. Their structures are shown in **Figure 75**.

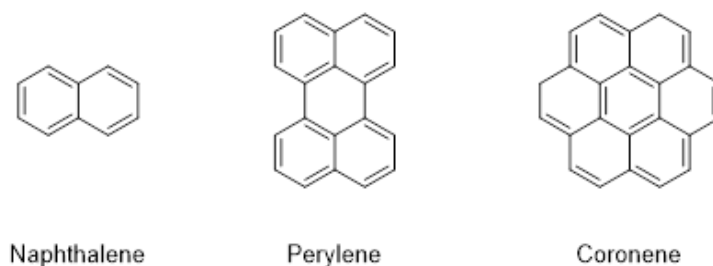


Figure 75: Aromatic compounds investigated for the CVD synthesis of graphene.

The compounds were selected to investigate the influence of the size of the aromatic system of the starting compounds influencing the graphene synthesis. The general CVD setup and the process, here for naphthalene as starting material, is shown in more detail in **Figure 76**.

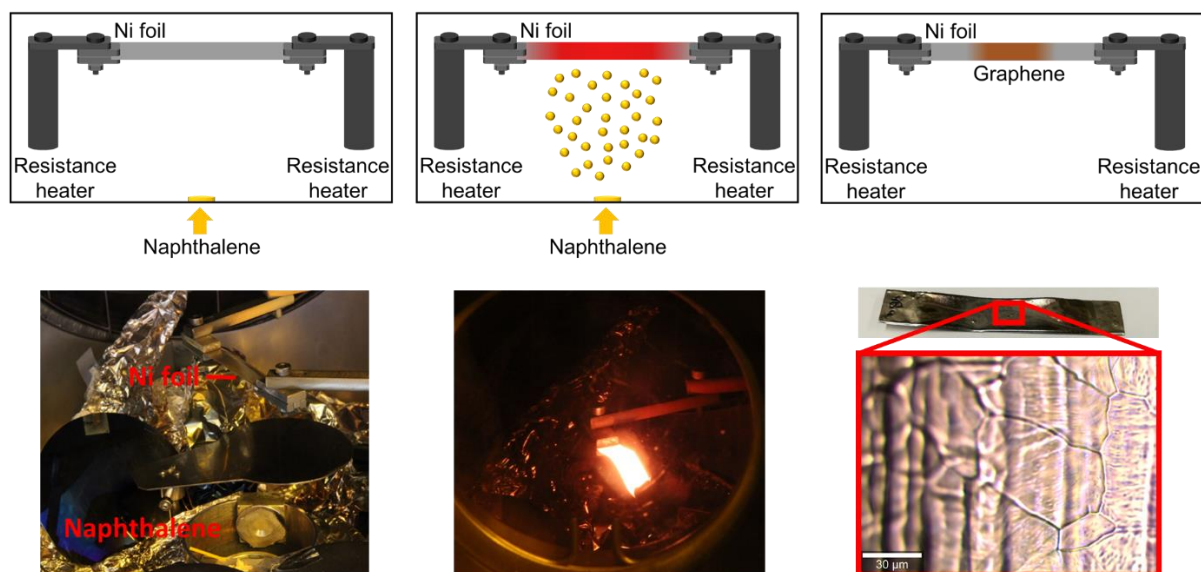


Figure 76: Used chemical vapor deposition setup. The schematic drawings (**above**) and pictures of the real setup (**below**) show the preparation process. As catalyst and carrier film a nickel foil was heated. Here naphthalene evaporates as a carbon source, indirectly heated by the hot nickel foil (700 °C to 1000 °C). After slowly cooling to room temperature graphene sheets were observed as exemplarily shown in the microscopic picture.

The investigated carbon sources were evaporated onto the heated nickel foil. The evaporation rate was determined by quartz microbalances. First, a screening of the nickel temperature was made to investigate the best reaction conditions for graphene synthesis. An overview is given in **Table 8**.

Table 8: Material screening for graphene synthesis.

Aromatic compound	Temperature [°C]	Result
Naphthalene	770	Graphite
Perylene	850	Graphite
Coronene	775	No structure

As it was found, the bigger the aromatic system the more difficult the decomposition of the compounds on the nickel surface towards elemental carbon and hydrogen. Therefore, for future investigations only naphthalene was chosen as an aromatic compound for the graphene synthesis. After screening the starting material, the best reaction conditions were investigated. More detailed investigations towards the optimal nickel temperature for the graphene synthesis were carried out with naphthalene as starting material which was evaporated onto nickel varying the foil temperature. A detailed overview is shown in **Table 9**.

Table 9: Temperature screening for graphene synthesis

Aromatic compound	Temperature [°C]	Result*
Naphthalene	430	No structure
Naphthalene	540	No structure
Naphthalene	660	No structure
Naphthalene	770**	No structure
Naphthalene	820	Graphite
Naphthalene	970	Graphite
Naphthalene	1075	Graphite
Naphthalene	1170	Graphite
Naphthalene	1260	Graphite

*visible with the eye by a brownish color

**best results from Kulkarni *et al.*

According to Kulkarni *et al.*, the best results were received with a nickel foil temperature of 770 °C, where graphene was visible as a brownish material on top of the nickel foil. However, in this work no carbon structures or color changes were visible up to about 820 °C. Increasing the temperature even further, the formation of carbon structures could be observed. The most promising results showed a temperature of 1260 °C. To validate the quality of the received structures Raman spectroscopy measurements were performed. Besides the symmetry of the 2D peak, the most common analysis to determine the number of graphene layers as well as the number of defects and with that the quality of the graphene, is the ratio of the G/2D peak. The resulting number of graphene layers can be calculated in the following:

$$\frac{I_G}{I_{2D}} = 0.14 + \frac{n}{10} ; n \text{ is the number of graphene layers} \quad (11)$$

Using this equation, the number of graphene layers can be calculated considering the ratio of the two peaks 2D and G. The correlating Raman spectra depending on the nickel foil temperature are shown in **Figure 77**.

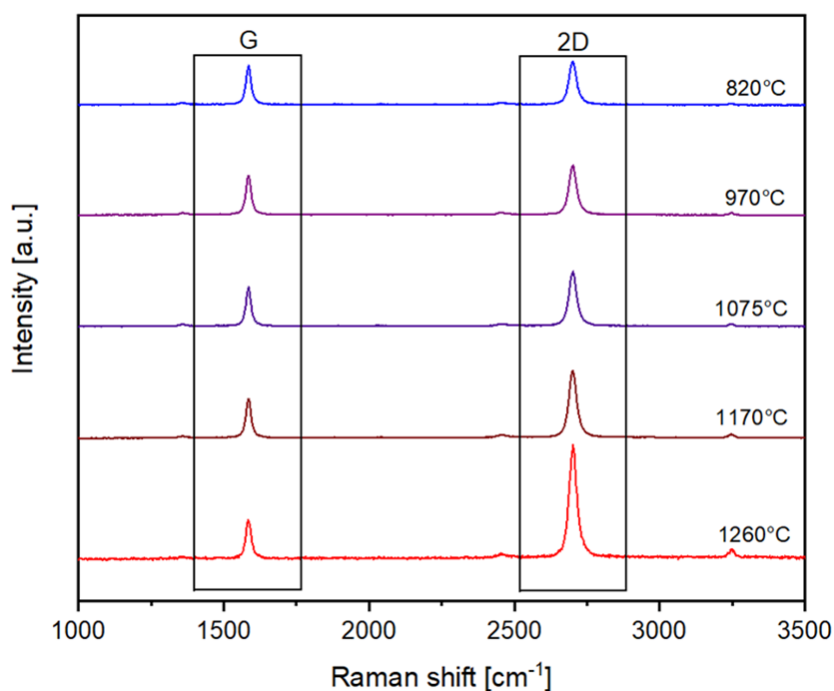


Figure 77: Raman spectroscopy measurements of the resulting graphite or graphene layer respectively, on the surface of the nickel foil, depending on the number of layers. The quality of the graphene improves with increasing ratio of the peaks 2D/G, here increasing with temperature. The highest quality could be observed at 1260 °C. Higher temperatures could not be used due to the CVD setup and the melting temperature of nickel.

With increasing temperature, the quality of the resulting graphene increases. This might be because the nickel oxide on the surface of the foil gets reduced easier at higher temperatures thus the surface is smoother and the carbon atom can diffuse easier into the nickel foil. So due to the lack of hydrogen during this approach, the temperatures necessary to reduce nickel oxide differ from the approach of e.g., Kulkarni *et al.*^[97]. Further investigations increasing the temperature even higher were not able to be conducted since the nickel foil started to rip apart reaching temperature close to the melting temperature of nickel (1455 °C). An overview of the G/2D values in correspondence with the temperature and the resulting number of graphene layers is shown in **Table 10**.

Table 10: Screening of synthesis parameters of graphene

Aromatic compound	Temperature [°C]	G/2D ratio	Number of layers*
Naphthalene	820	0.90	8
Naphthalene	970	0.78	6
Naphthalene	1075	0.65	5
Naphthalene	1170	0.56	4
Naphthalene	1260	0.34	2

*according to equation (4)

As already depicted in the Raman spectra in **Figure 77** the quality of the graphene sheets increased with increasing temperature of the nickel foil used as catalyst material. The same results show the calculated number of graphene layers determined *via* Raman spectroscopy while using equation (4). The best result was observed using 1260 °C for the nickel foil temperature. In this experiment bilayer graphene with a very good quality could be synthesized. However, it was not possible to achieve big sheets of bilayer graphene on the nickel surface. Further investigations showed that on the same sample different numbers of layers were detected depending on the measurement spot. **Figure 78** shows two characteristic Raman spectra from the same sample surface measuring two different spots. While there was bilayer graphene detectable, besides the number of graphene layers distinguished (blue). This might correlate with the smoothness of the nickel surface. The smoother the nickel surface the better the quality of the graphene after the synthesis. However, if there are grain boundaries remaining on the surface they can act as “seeds” for the formation of multilayer graphene.

The blue spectrum correlates with multilayer graphene while the red spectrum correlates to high quality graphene with a maximum of two layers. These measurements show the difficulty of the realization of a large-area homogeneous graphene layer by the used CVD process. High-quality graphene can be easily accompanied by multilayer graphene within the same specimen.

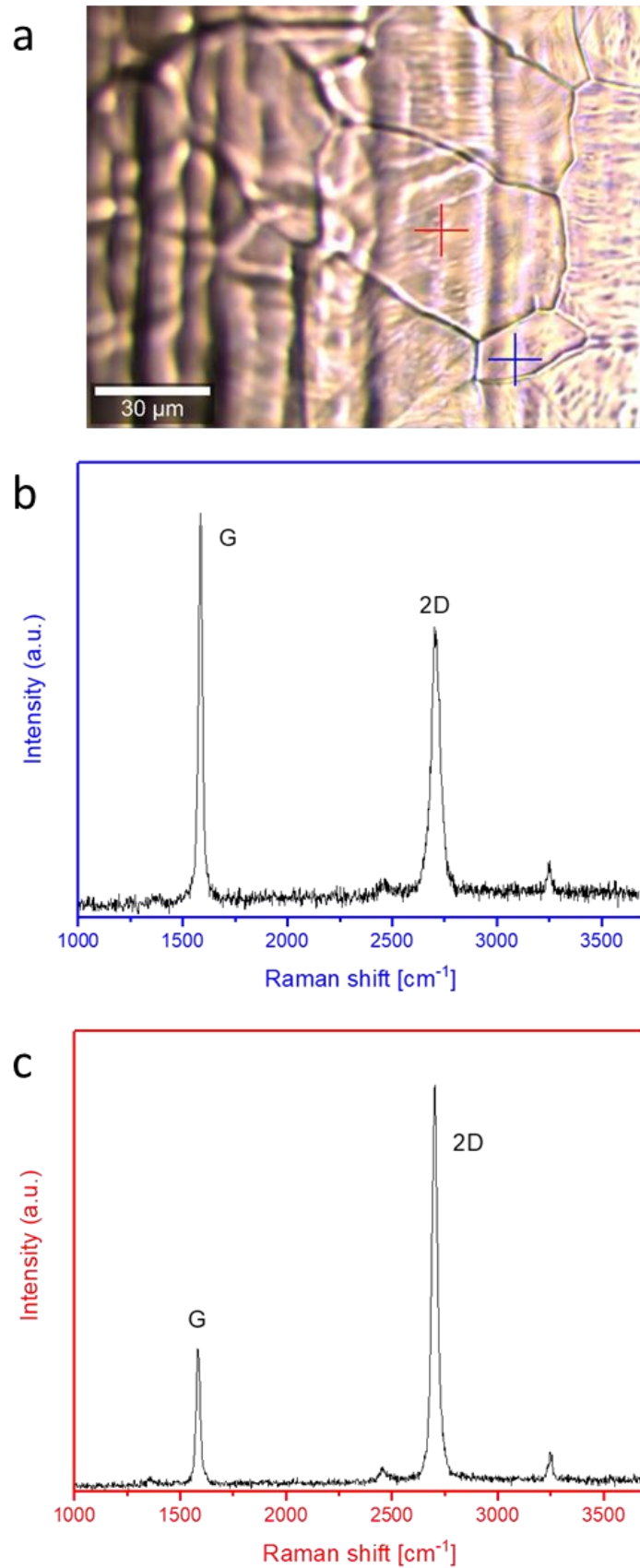


Figure 78: Raman analysis of the graphene sheets shown on the surface of the nickel foil. Several different spots were measured and two characteristic Raman spectra are shown. The blue spectrum clearly shows there are several graphene layers in this sample. The red spectrum corresponds to high-quality graphene with a maximum number of two layers.

In addition to Raman spectroscopy, SEM pictures were taken to further investigate the graphene results and are shown in **Figure 79**.

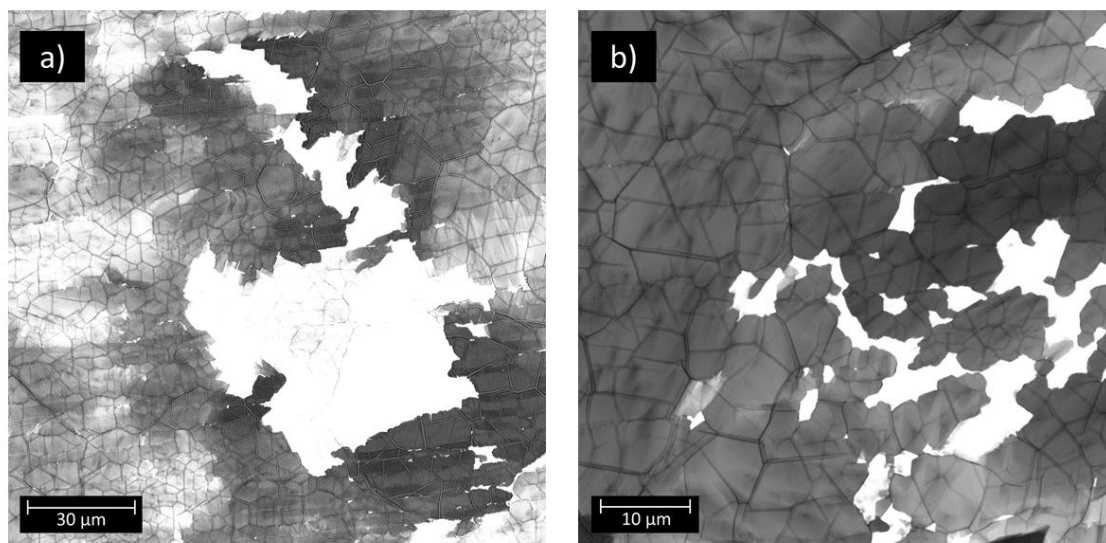


Figure 79: SEM pictures of the graphene sheets on the nickel surface. There are clear sheets visible. Different brightness at different parts of the sample might indicate different number of graphene layers depending on the brightness. Nevertheless, the thin sheets in the middle of (a) indicate, that there are spots where the synthesis of single-layer graphene was successful. This indicates that the synthesis of single-layer graphene was only partially successful.

As shown in **Figure 79**, there are spots on the nickel foil where you can observe bi- or even monolayer graphene indicated by the high brightness of the sample at these areas. However, in the same picture multilayer graphene can be clearly observed indicated by the less bright areas of the SEM pictures, as few-layer graphene is a transparent material. In the case of multilayer graphene, the sheets are not transparent anymore.

Due to the lack of big amounts of high-quality graphene for the investigation as conductive material in the cathode material of a lithium ion battery, exfoliated graphene was purchased from a commercial source to ensure enough material is available.

3.3.2 Melt-processing of cathode materials for lithium ion batteries

In this chapter, a novel cathode material was investigated which is melt-processable and therefore enables a wide field of possible processing procedures. As described before, see **Figure 72**, the cathode consists of 3 major components: the active material, the binder material, and the electron-conducting material. To achieve good melt-processability, the binder material is the most important part as it controls the mechanical and thermal properties. The active material and the electron-conducting additive usually consist of non-melttable components. For this investigation, the $(AB)_n$ segmented copolymers were selected as the binder material in the cathode material while graphene was selected

as electron conducting material. The (AB)_n segmented copolymer showed promising melt-processing abilities as shown in Chapter 3.1.3. As explained before, the amount of binder material should be as small as possible to allow a larger amount of active material to be used, but enough to enable processing of the cathode mixture. Here, the cathode composition was optimized by screening the lowest amount of electron-conducting material necessary to achieve decent electron conduction. Afterwards, the amount of (AB)_n segmented copolymer could be investigated towards the best overall material composition, which was found to be 11 wt-% of graphene, 35 wt-% of (AB)_n segmented copolymer, and 54 wt-% of LFP as active material. This mixture was continuously compounded keeping the melt at 200 °C for 20 min to achieve a homogeneous mixture of the cathode material. Compounding the cathode material in the melt of the (AB)_n segmented copolymer eliminates the need for a solvent. The usual methods to prepare cathode material are by preparing slurries in common solvents like NMP. Here, high-boiling solvents like NMP are very difficult to remove completely in further processing steps. This issue can be avoided by using the (AB)_n segmented copolymer melt as “solvent” and binder material itself.

After compounding the cathode material several melt-processing techniques were investigated. First, the material was processed *via* compression molding. This method proved impractical as the resulting film for the cathode material should be very thin (<100 microns). To achieve thin films the material has to be compression molded using a high pressure (>5 tons). During this procedure, the composite separated, leading to a brittle film where the polymer was pressed to the outer rim, and the active and conducting materials were mainly in the center. Because of this result, the compression molding technique was not applicable. A different investigated approach was melt-processing *via* extrusion-based additive manufacturing or rather 3D printing. For 3D printing applications, the preparation of filament is necessary. In this work, the filament was prepared *via* injection molding directly after the compounding of the still-hot melt mixture. A schematic setup of this procedure is shown in **Figure 80**.

The three components: LFP as active material, graphene as electron conducting material, and (AB)_n segmented copolymer as binder material were mixed in a compounder for 20 min at 200 °C followed by 10 min at 220 °C to ensure a homogeneous mixture of all components. The hot melt was then hot transferred into the plunger-typed injection molding setup. As mold, a cavity with the shape of a filament rod was used. A PTFE tube was placed inside the mold to make sure that the filament does not adhere to the metal mold. The PTFE tube has an inner diameter of 3 mm which is a common diameter for a filament for extrusion-based 3D printing applications. After the removal of the Teflon tube, the filament rods were used for 3D printing.

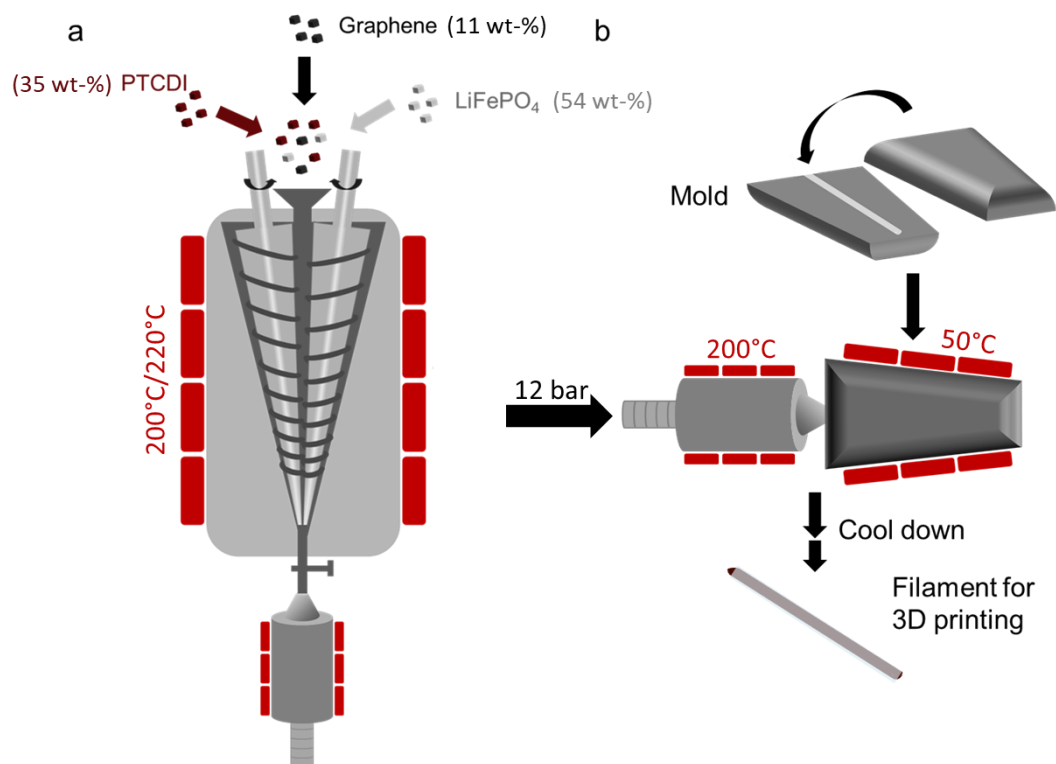


Figure 80: Schematic drawing of the filament rod processing of the cathode materials. First, the three components were compounded to ensure a homogeneous mixture (a). Afterward, the hot mixture was transferred to the plunger-type injection molding setup and filament rods for 3D printing were prepared.

The printing setup was similar to the one used before for the extrusion-based 3D printing of the electrolyte. However, this time the material was not printed directly on the P-surface 141 but on a current collector substrate used for lithium ion battery cathode materials. The selected substrate was a carbon-coated aluminum foil. Aluminum is a standard current collector for cathodes in lithium ion battery applications. As a further development, aluminum is coated with carbon to increase the adhesion of the cathode material and ensure good contact. This is necessary for the smooth transport of the electrons out of the cathode material towards the current collector. An SEM picture of such a carbon-coated aluminum foil is shown in **Figure 81**.

In the SEM picture, on top of the aluminum foil, the carbon layer with a thickness of roughly 1 μm is observable. This SEM picture could ensure the quality and smoothness of the coated layer. Therefore, this carbon-coated current collector was used as the substrate for the 3D printing of the cathode material. As optimized operating parameters an extruder temperature of 180 $^{\circ}\text{C}$ and a bed temperature of 80 $^{\circ}\text{C}$ were used. The thickness of the resulting cathode material was tailored to obtain 50 microns. The 3D printing setup was similar to the one used for the extrusion-based 3D printing of the (AB)_n segmented copolymers (cf. **Figure 48**).

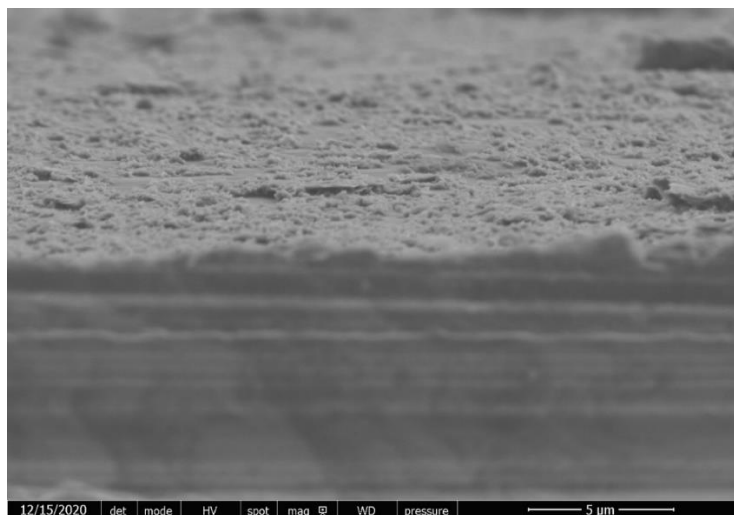


Figure 81: SEM picture of carbon-coated aluminum foil used as current collector. On top of this substrate, the cathode material was deposited as a thin layer by extrusion-based 3D printing. The thickness of the carbon coating could be determined to be roughly 1 micrometer. The carbon coating shows a relative smooth surface.

A filament rod of the cathode material consisting of LFP, graphene, and $(AB)_n$ segmented copolymer, **2b** (PTCDI-Jeff(2003)-PTCDA), was fed into the liquefier by the driving wheel. In the liquefier, with a temperature of 180 °C, the $(AB)_n$ segmented copolymer melted due to the disaggregation of the perylene imide units. Therefore, the binder polymer melts and allows the material to become viscous enabling the 3D printing process. The viscous material was then printed onto the carbon-coated aluminum foil which was placed on P-surface 141. The bed temperature was heated to 80 °C which is close to the melting temperature of the $(AB)_n$ segmented copolymer. This allowed a slow solidification process and thus the formation of perylene imide stacking without quenching the material in a more amorphous state. After the printing process, the cathode material was allowed to cool down to room temperature for further investigations such as the calibration of the thickness of the material and conductivity measurements.

3.3.3 Conclusion of the chapter

This chapter shows the preparation of a melt-processable lithium ion battery cathode material. For the purpose of the conductive additive of the cathode material, graphene was synthesized *via* CVD. High-quality graphene sheets could be synthesized using nickel foil as a catalyst and carrier substrate. However, reproducible large-area graphene films usable for the processing of a cathode material were not achieved. Therefore, graphene was purchased and used as an electron conducting additive in the cathode material processing. The melt-processability of the demonstrated cathode material allows for avoiding solvents like NMP. Such typically high-boiling solvents are almost impossible to be completely removed after film preparation of the cathode. This can lead to safety issues in a resulting solvent-prepared battery cell. In this chapter successful 3D printing of solvent-free solid-state cathode materials was demonstrated allowing new manufacturing procedures and possibly new cell designs of lithium ion batteries.

3.4 Solvent-free solid-state lithium ion battery *via* melt-processing

This chapter combines the previous two chapters by combining the two prepared materials to establish a fully melt-processed lithium ion battery. Chapter 3.2 showed the possibility to melt-process a solvent-free solid-state electrolyte to form thin electrolyte films. Chapter 3.3 established the melt-processing of a solvent-free solid-state cathode material. To prepare a fully working lithium ion battery, in addition to the electrolyte and cathode materials, there is the need for an efficient anode material. As described before, the main goal is to use pure lithium metal as anode material. However, the use of pure lithium instead of the most common graphite-based anode material is limited by the typically used electrolyte. The lack of sufficient mechanical stability leads to the formation of lithium dendrites and thus to serious safety issues of the lithium ion battery. In this work, a solvent-free solid-state electrolyte material was successfully synthesized. Not only the solid-state but also the elastic behavior can help to avoid dendrite formation, which allows the use of lithium metal as anode material for lithium ion batteries. The solid-state battery was prepared as follows: for both materials, the filament rods for extrusion-based 3D printing were prepared as described before

3.4.1 Lithium ion battery via extrusion-based 3D printing

After the preparation of the filament rods and optimization of the 3D printing parameters for each material, the materials are combined obtaining a fully melt-processed lithium ion battery. The setup is shown in **Figure 82**.

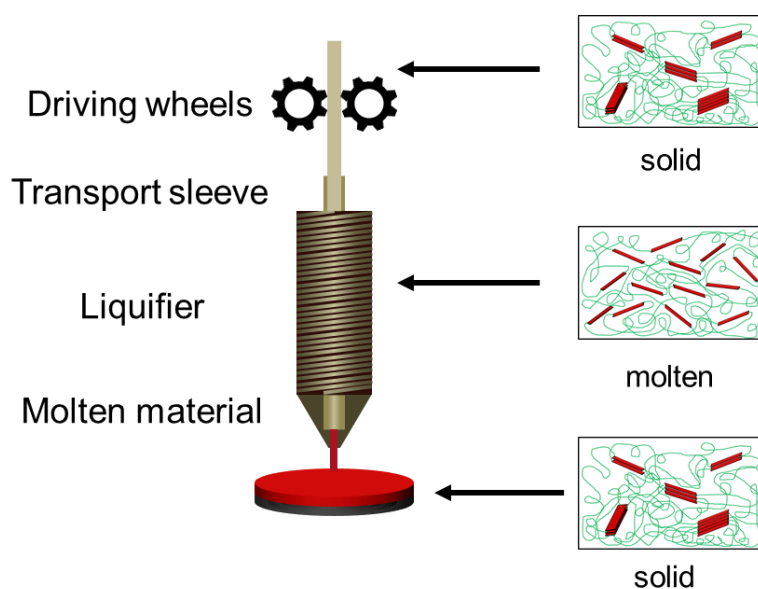


Figure 82: Schematic drawing of the extrusion-based 3D printing of the electrolyte and cathode material. The solid electrolyte and cathode material are melted in the liquefier to enable 3D printing while upon cooling the material solidifies in the deposited layer.

For the purpose of extrusion-based 3D printing, filament sticks were prepared via injection molding which then were fed into the 3D printer. The materials were printed right on top of each other ensuring a smooth interface between the layers which is necessary for a good performance of the finally achieved battery. First, a 130 μm thick film of the cathode material was 3D printed onto the surface of the carbon-coated aluminum foil with a diameter of 14 mm, adapted to the coin cell setup (inner diameter of 18 mm) with some buffer for the fabrication process afterward (cf **Figure 83**).

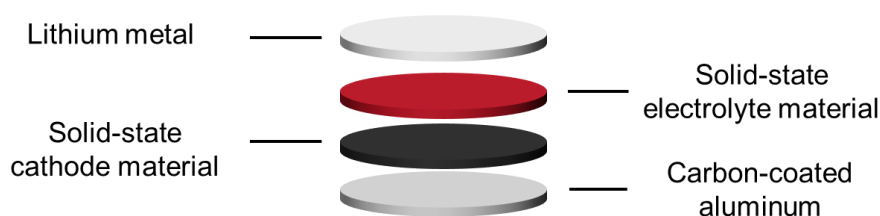


Figure 83: Schematic drawing of the full battery setup. From bottom to top: carbon-coated aluminum, solid-state cathode material, solid-state electrolyte material, and lithium metal on top. The cathode material was prepared as a blend of lithium iron phosphate, $(\text{AB})_n$ segmented copolymer and graphene. The electrolyte material was prepared as a blend of $(\text{AB})_n$ segmented copolymer and LiTFSI.

The temperature of the liquefier was kept at 180 $^{\circ}\text{C}$ as optimized before. The bed temperature was set to 110 $^{\circ}\text{C}$ to ensure the material was not quickly quenched and had enough time for the perylene imide units to form the physically crosslinked network. After the solidification of the cathode material, the bed temperature was kept at 110 $^{\circ}\text{C}$. Then the filament rod was changed with the electrolyte material and the nozzle temperature was set to 130 $^{\circ}\text{C}$ which was optimized before to achieve the best printing results for the electrolyte material. The diameter of the electrolyte film was selected to be slightly larger than the cathode material to ensure the cathode material is covered completely avoiding any short circuits. The thickness of the electrolyte film was set to 130 μm as well. **Table 11** summarizes the used optimized printing parameters.

Table 11: Summary of the 3D printing parameters of the cathode and electrolyte materials.

	Cathode material	Electrolyte material
Nozzle temperature [$^{\circ}\text{C}$]	180	130
Bed temperature [$^{\circ}\text{C}$]	110	110
Thickness [μm]	130	130
Diameter [mm]	14	14.2

To investigate the interface of the Al/cathode/electrolyte sequence the layers were investigated via SEM microscopy. An obtained picture is depicted in **Figure 84**.

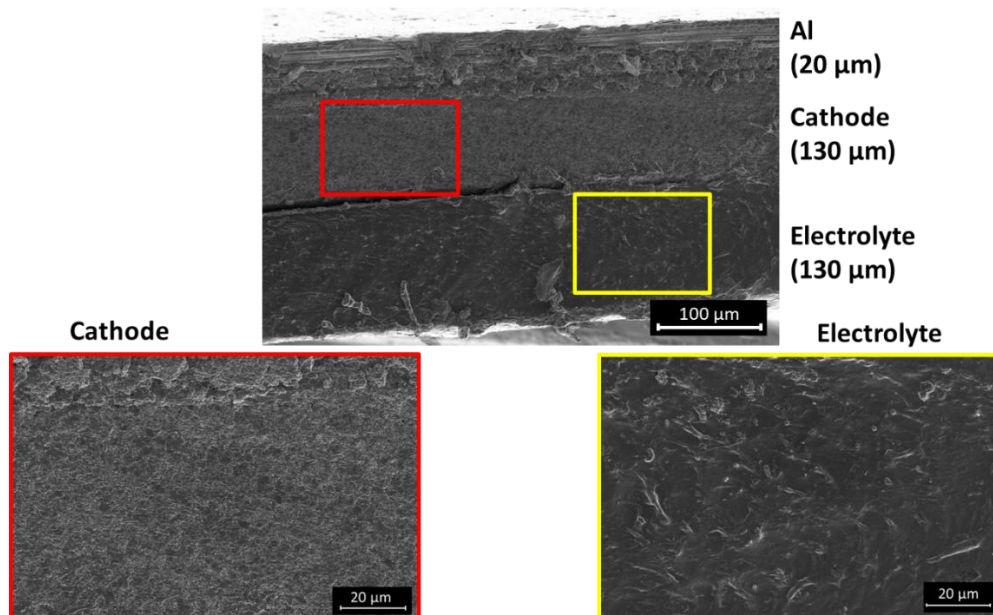


Figure 84: Sideview of SEM pictures of the cathode and electrolyte material (**2b-LiTFSI** (PTCDI-Jeff(2003)-PTCDA-LiTFSI) [20:1]) printed on a carbon-coated aluminum foil. The samples were cut vertically from the 3D printed sample. The pictures demonstrate the homogeneity of the cathode and electrolyte materials. The contact between the cathode and the electrolyte material is observed very tight.

From top to bottom, there is the carbon-coated aluminum foil, the cathode material as well as the electrolyte material. In lithium ion batteries often the loss of contact between the current collector and the cathode material can lead to issues regarding the overall performance of the battery. The SEM picture shows there is a really smooth interface between the aluminum foil and the cathode material. The cathode material itself is homogeneously mixed (red square). Therefore, this indicates that filament rod preparation *via* compounding and melt-processing in terms of extrusion-based 3D printing leads to a very homogeneous mixture of the cathode material. The electrolyte (yellow square) shows a very homogeneous material as well.

After the observation of the high quality of the 3D printed cathode and electrolyte films, the thickness of the cathode as well as the electrolyte could be lowered to 50 microns by the optimization of the Z-gap between the 3D printing build surface and printer nozzle. Thinner cathode and electrolyte layers decrease the internal resistance of the cell according to equation (4). The films with a layer thickness of 50 μm were used for the preparation of the full battery.

To finalize the battery cell, a pure metallic lithium foil with a diameter of 12 mm was placed on top of the electrolyte layer. A diameter of 12 mm was selected to ensure that the lithium does not come into contact with the cathode material during the assembly process in the glove box. In this context, the mechanical stability of the novel electrolyte material allows the usage of lithium as the anode material. The complete cell structure is depicted in **Figure 85**.

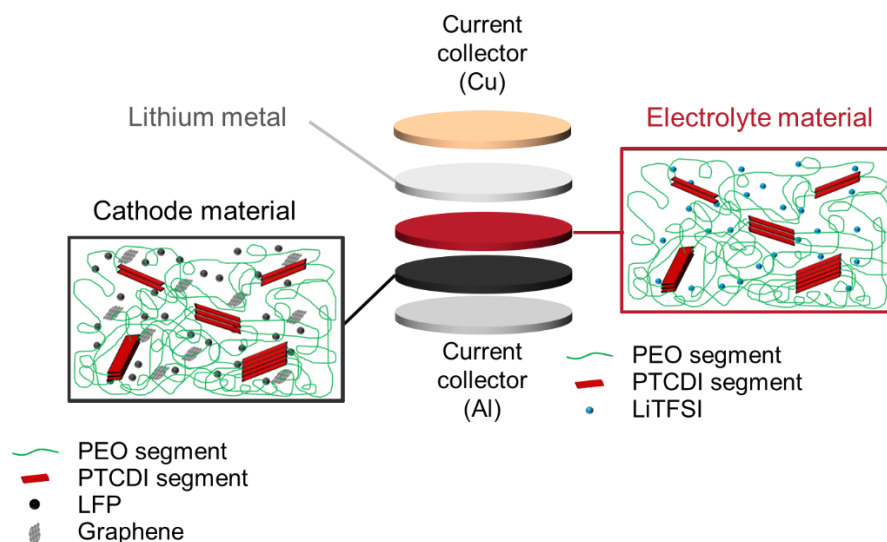


Figure 85: Schematic drawing of the layered structure of the extrusion-based 3D printed lithium ion battery.

The complete cell consists of 5 components as shown in **Figure 85** from top to bottom: copper as the current collector, lithium metal as the anode material, the 3D printed electrolyte material, the 3D printed cathode material as well as aluminum as the current collector. The main component of the electrolyte and the binder polymer of cathode materials is the synthesized $(AB)_n$ segmented copolymer **2b** (PTCDI-Jeff(2003)-PTCDA). The difference in these two materials arises from different ratios and different additive materials.

This cell setup was put together in the glove box under inert conditions due to the use of lithium using the same crimping setup as shown for the electrolyte material (cf. Chapter 3.2.3). After encapsulating the battery, the cell was transferred out of the glove box and was characterized *via* galvanostatic cycling with potential limits (GCPL) investigations. The potential window for GCPL measurements correlates with the rated voltage of the used active material. The rated voltage of LFP-based systems is around 3.2 - 3.3 V vs Li/Li⁺. Therefore, the GCPL measurements were made in a potential window from 2.5 - 4.2 V which is typically applied to LFP-based systems. The current density was set to 0.1 mA cm⁻¹ and the current was kept constant at 280 mA. The C-rate describes the charging and discharging current depending on the overall capacity of the cell. It can be calculated by measuring the time necessary to fully charge or discharge the battery while keeping the current at a constant value. The C-rate can be described by the following equation:

$$C - rate = \frac{1C}{t_{full} [h]} \quad (12)$$

A C-rate of 1 C means the cell charges and discharges each in one hour, a C-rate of 1/10 C means charging and discharging takes 10 hours. The measurement time can therefore increase to very long

periods of time. However, the GCPL process simulates the usage of the battery best. The charge and discharge cycles are repeated over and over, just like the usage of batteries in applications and devices. The slower the charging of the cell the higher the capacity, because the material has more time to intercalate the lithium ions into the lattice and to transport lithium ions from the electrolyte interface deeper into the cathode material. The capacity of the battery cell correlates with the active material of the cathode. In this case, the active material used was LFP which has a theoretical capacity of 175 mAh g⁻¹. For the GCPL measurement, a C-rate of 0.1 C was chosen. The resulting capacity in dependence on the potential and the number of cycles is depicted in **Figure 86**.

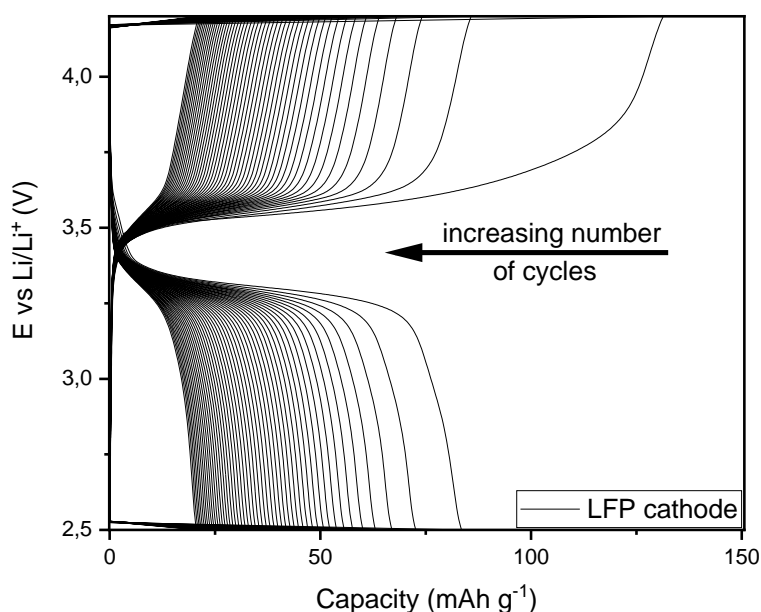


Figure 86: Galvanostatic cycling (C rate of 0.1 C) of the lithium ion battery manufactured *via* extrusion-based 3D printing. As cathode material, the before processed lithium iron phosphate (LFP) material (11% graphene, 35% **2b** (PTCDI-Jeff(2003)-PTCDA), and 54% LFP) was used with **2b-LITFSI** (PTCDI-Jeff(2003)-PTCDA-LITFSI) [20:1] as electrolyte and lithium metal as anode material. While the initial charging of the coin battery cell shows a capacity of about 130 mAh g⁻¹ (in regards to the cathode material), the capacity fades with the increasing number of cycles. This can be assigned to material degradation within the cathode material.

The GCPL measurement shows that the prepared cell is a working lithium ion battery with an initial charge capacity for the active material of 130 mAh g⁻¹. The initial discharge capacity is around 80 mAh g⁻¹ which is roughly half of the specific capacity of LFP. The coulombic efficiency was calculated according to the following equation:

$$C_{\text{coulombic}} = \frac{C_{\text{discharge}}}{C_{\text{charge}}} * 100 \quad (13)$$

The maximum coulombic efficiency was determined to be at 96 % which is a good value for lithium ion batteries. However, with the increasing number of cycles the capacity decreases further until after 40 cycles, the capacity is at around 25 mAh g⁻¹. This loss of capacity could be explained by material

degradation or some rearrangements in the macroscopic structure, leading to a worse transport of the lithium ions and thus to a bigger internal resistance. This would lead to a decrease in capacity because the lithium ions are not transported through the whole cathode material but only intercalate in the area close to the electrolyte interphase. As this lithium ion battery preparation technique *via* 3D printing was aimed to be a proof of principle, no further investigations towards the change of the cathode material during charge and discharge were conducted. Due to the presented stability of the electrolyte material in the previous chapter not showing any significant degradation after more than 1200 cycles in an anode half-cell, the capacity decrease of the full cell is attributed to the cathode. In a conclusion, the preparation of a fully 3D printed lithium ion battery was successful and demonstrates the outstanding properties of the synthesized $(AB)_n$ segmented copolymer.

3.4.2 Conclusion of the chapter

The final chapter concludes with the preparation of a fully melt-processed lithium ion battery. The melt-processing of electrolyte and cathode layers was realized *via* extrusion-based 3D printing allowing new ways of tailoring the shape for new battery designs. The achieved battery showed promising results towards the use of melt-processable lithium ion batteries. All used materials were solvent-free solid-state materials avoiding any safety issues concerning residual solvent in the encapsulated cell. The exclusively used solid-state materials prohibit the dendrite formation of lithium and thus allows the use of pure lithium as anode material making this a promising electrolyte material for future investigations. A working battery with a capacity of 80 mAh g^{-1} was achieved with a maximum coulombic efficiency of 96 %.

4. Experimental Part

4.1 Materials

The reagents were purchased from Sigma Aldrich (Jeffamine ED-Series, PTCD, Naphthalene, Perylene, Coronene, LiTFSI), Alfa Aesar (Nickel foil, Lithium foil), SS Nano (Exfoliated graphene), TCI (tert butyl phthalic anhydride), Carbosynth (Lithium iron phosphate), PI KEM (stainless steel electrodes, wavesprings, coin cells C2032), ChemPur (Carbon coated aluminum foil) and Merck (0.1N HCl in isopropanol). All chemicals were used as received.

The molecular weights of the diamines were determined by end group titration.

4.2 Characterization methods

End group titration

The number average molecular weight M_n of the diamines (PDMS-diamines, PEG-diamines, Jeffamine ED-900) was determined by potentiometric titration of the amine end groups using an 809 Titrand robot with a Solvotrode easyClean electrode from Metrohm. The prepolymers were weighed into a 100 mL flask and dissolved in 60 mL of equal volume mixture of isopropanol (p.a.) and tetrahydrofuran (p.a.). The PEG-diamines were initially dried at 100 °C under high vacuum for at least 2 h. To titrate the amine end groups a standard titrant of 0.1 N HCl in isopropanol (Merck) was used. The number average molecular weight of the diamines was calculated according to equation 14. An average of three measurements is given.

$$M_n = m_{polymer} \cdot \frac{\xi}{c \cdot V} \quad (14)$$

With $m_{polymer}$ being the mass of the diamines, ξ the number of functional end groups (here: 2), c the concentration of the titrant and V being the consumed volume.

¹H-nuclear magnetic resonance spectroscopy (¹H-NMR)

¹H-NMR spectroscopy was performed on a BRUKER Avance 300 spectrometer with an operating frequency of 300 MHz. Deuterated chloroform and deuterated THF-d8 were used as solvents. Chemical shifts are reported in ppm relative to the known value of residual solvent signal.

Differential scanning calorimetry (DSC)

Differential scanning calorimetry was conducted on a DSC3+ STARe System from Mettler Toledo. The heating and cooling runs were performed at a scan rate of 10 K min⁻¹ under a constant flow of dry nitrogen (50 mL min⁻¹). Indium was used for calibration.

Thermogravimetric analysis (TGA)

Thermogravimetric analyses were performed on a Mettler Toledo TGA/DSC3+ STARE System at a heating rate of 10 K min⁻¹ under constant flow of nitrogen.

Dynamic mechanical analysis (DMA)

Dynamic mechanical thermal analysis of bulk material of thin polymer films were measured within a metal pocket in a single cantilever mode using a DMA 1 Stare System from Mettler Toledo at a heating rate of 5 K min⁻¹ and a frequency of 2 Hz.

Fourier-transform infrared spectroscopy (FT-IR)

FT-IR measurements were performed on a Perkin Elmer FTIR Spectrum 100 spectrometer using the attenuated total reflectance unit (ATR). The spectra were recorded from 4000 – 650 cm⁻¹ using 16 scans and a resolution of 4 cm⁻¹.

Ultraviolet-visible spectroscopy (UV/Vis)

UV/Vis absorbance (375 – 650 nm) was measured using a Jena Analytics reader FLASH scan 530 (Jena, Germany). The UV/Vis active dye, Lumogen® Red F300, was added to the softer copolymer. The samples were spin-coated (THF, 5wt-%, 2000 rpm) on a 384-well microplate. The reported absorbance values are standardized to the thickness measured for each sample.

Raman spectroscopy

Raman measurements were performed on a combined Raman-imaging/scanning force microscope system (Witec Alpha 300 RA+) with a UHTS 300 spectrometer and a back-illuminated Andor Newton 970 EMCCD camera. Raman spectra were obtained using an excitation wavelength of $\lambda = 532$ nm and an integration time of 0.5 s/pixel (100x objective). All spectra were subjected to a cosmic ray removal routine and baseline correction.

X-ray diffraction (XRD)

X-ray data were collected on a STOE IPDS II diffractometer (173 K, graphite monochromated Mo-K α 1 radiation ($\lambda = 0.71073$ Å)).

Scanning electron microscopy (SEM)

All samples were sputtered with approximately 1.3 nm of platinum in a Cressing 208HR sputter and analyzed by SEM Zeiss Leo 1530 (Zeiss, Jena, Germany) at 3.0 kV.

The scaffold fabricated by MEW was characterized using a Crossbeam 340 scanning electron microscope from Carl Zeiss Microscopy GmbH, Germany at 3.0 kV.

Transmission electron microscopy (TEM)

Transmission electron microscopy was conducted on a Zeiss Leo EM922 Omega microscope operated at 80 kV.

Potentiostatic electrochemical impedance spectroscopy (PEIS)

All electrochemical measurements were performed on a BioLogic VMP3[®] potentiostat working with the software EC-Lab V11.01. The temperature was controlled by a Vötsch VT 4002[®] oven. All preparations, cell assembling and disassembling were performed in an argon filled glove box equipped with a copper catalyst for gas purification ($\text{H}_2\text{O} < 0.1 \text{ ppm}$ and $\text{O}_2 < 1 \text{ ppm}$). The overall ionic conductivities of all films were studied via potentiostatic impedance spectroscopy (PEIS). Subsequently, impedance spectra were recorded at 60 °C, 25 °C, 30 °C, 40 °C, 50 °C, 60 °C, 70 °C and 80 °C. At each temperature, the impedance measurement started after 1.5 h of annealing to guarantee enough time for thermal equilibration.

Cyclic voltammetry (CV)

The electrochemical stability window of the neat polymers and films were studied via cyclic voltammetry (CV). Copper-lithium Cu/electrolyte/Li asymmetric CR2032 coin cells were assembled and hermetically sealed. The assembly was pressed at room temperature using an electric pressure-controlled coin cell crimping machine (MSK-160D, MTI).

The cells were transferred to the oven and mounted into a coin cell rack connected to the potentiostat. Cyclic voltammetry experiments were performed by scanning a potential between $E_1 = -0.2 \text{ V}$ and $E_2 = 4.2 \text{ V}$ vs. Ref ($E_{WE} = E_i = 0 \text{ V}$ vs. EOC and reverse scan towards $E_f = 0 \text{ V}$ vs. EOC) with a scan rate of $dE/dt = 1 \text{ mV s}^{-1}$.

Galvanostatic cycling with potential limits (GCPL)

GCPL was carried out in an asymmetrical Li/electrolyte/cathode material cells in two-electrode configuration. The assembly was pressed at room temperature using an electric pressure-controlled coin cell crimping machine (MSK-160D, MTI). After transferring the cells to the climate chamber they were mounted into a custom-made coin cell rack and connected to the potentiostat. First the cells were annealed at 70 °C for 12 hours to ensure good contact between all materials. The measurement was conducted at 70 °C and the potential was measured every 10 mV. The cells were subsequently charged and discharged for up to 1250 cycles. As current a C-Rate of 1/10 C was used.

4.3 Processing methods

Extrusion-based 3D printing

A FFF desktop 3D printer (3NTR A4, Italy) was used in this study. The nozzle diameter was 450 μm . The 3D digital models of the geometries were first designed with Autodesk Fusion 360 and additionally sliced with the software Slic3r (Version 1.3.0).

Injection molding

Injection molding filaments for 3D printing were produced using a DSM Xplore 12mL injection molding machine (cf. **Figure 47**). Injection molding was performed with an injection/holding pressure of 6 bar for 5s.

CVD

Chemical vapor deposition of graphene was conducted in a Balzer PLS 500 evaporation chamber. The nickel foil was placed in-between two resistive heaters. The temperature of the nickel foil could be controlled by controlling the current applied to the resistive heaters and was calibrated before. Naphthalene was evaporated out of a tungsten boat placed below the nickel foil, heated only passively by the hot nickel foil (cf. **Figure 73**).

4.4 Synthesis of tBPA end-capped (AB)_n segmented copolymers

Jeffamine ED-900 and Jeffamine ED-2003 were titrated using potentiometric end group titration to determine the exact molar mass of the Jeffamine. The titration was done with 0.1N HCl in isopropanol solution. The resulting molar masses were used to calculate the Jeffamine to perylene ratio in the upcoming reaction procedures.

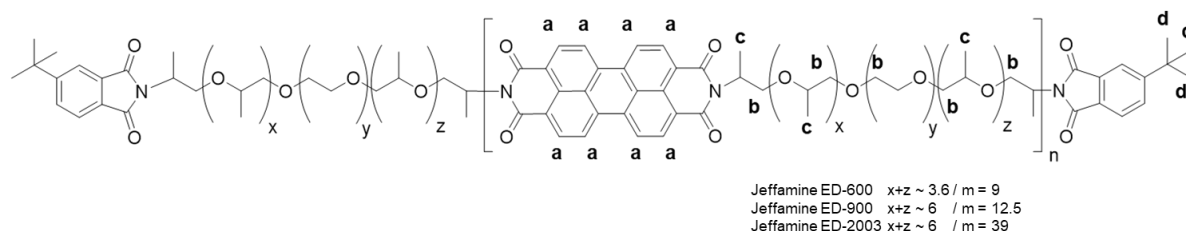
General procedure

A stainless-steel metal reactor, with a wall thickness of 7 mm, was pre-heated to 80 °C under constant argon flow. After one hour, PTCDA (392, 2 g mol⁻¹, 1 eq.) was filled into the metal reactor and Jeffamine ED-900 (894 g mol⁻¹, 1.25 eq.), Jeffamine ED-2003 (2018 g mol⁻¹, 1.25 eq.) and 1:1 molar ratio of Jeffamine ED-900 (894 g mol⁻¹, 0.625 eq.), Jeffamine ED-2003 (2018 g mol⁻¹, 0.625 eq.), respectively, were added in the metal reactor. The reactor was sealed with a HNBR rubber on top and the mixture was heated up to 200 °C and stirred for 25 hours at least under inert conditions. The reaction progress was monitored *via* FT-IR spectroscopy. The resulting (AB)_n segmented copolymer was used as received for the end-capping process.

Endcapping procedure of tBPA end-capped (AB)_n segmented copolymers

After synthesis of the (AB)_n segmented copolymer the end-capping was done in the same one-pot setup as used before. The reaction mixture was allowed to cool down to 80 °C. Upon reaching 80 °C 4-*tert*-butyl phthalic anhydride (204.22 g mol⁻¹, 5 eq.) was added and the mixture was heated to 200 °C and stirred for 20 hours. The reaction process was monitored via FT-IR spectroscopy. After completing the end-capping reaction the mixture was allowed to cool down to room temperature and the tBPA end-capped (AB)_n segmented copolymer was extracted out of the metal reactor.

FT-IR (cm⁻¹): 3500, 3120, 2870, 1850, 1770, 1755, 1730, 1696, 1653, 1593, 1506, 1456, 1406, 1344, 1300, 1233, 1093, 1017, 937, 860, 810, 758, 745, 730.



¹H-NMR (300 MHz, THF-d₅): δ (ppm) = 8.2-8.6 (m, 80H, perylene-CH^a), 3.2-4.5 (m, 100H, CH₂^b), 0.7-1.9 (m, 120H, CH₃^c), 1.3 (s, 18H, CH₃^d).

DSC (2nd heating, 10 K min⁻¹):

1a (PTCDI-Jeff(900)-tBPA): T_{m,Jeff}: 7 °C; T_{m,Pery}: 189 °C

1b (PTCDI-Jeff(900/2003)-tBPA): $T_{m,Jeff}$: 24 °C; $T_{m,Pery}$: 166 °C

1c (PTCDI-Jeff(2003)-tBPA): $T_{m,Jeff}$: 31 °C; $T_{m,Pery}$: 95 °C

TGA (5%-weight loss):

1a (PTCDI-Jeff(900)-tBPA): 393 °C

1b (PTCDI-Jeff(900/2003)-tBPA): 396 °C

1c (PTCDI-Jeff(2003)-tBPA): 395 °C

Yield: 40 g

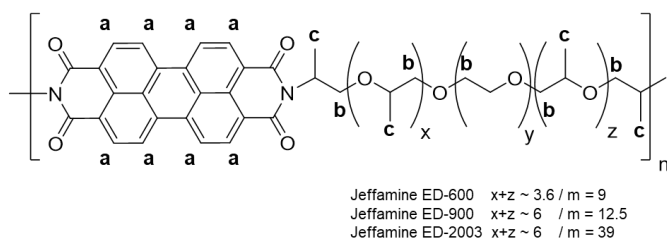
4.5 Synthesis of perylene end-capped (AB)_n segmented copolymers

Jeffamine ED-900 and Jeffamine ED-2003 were titrated using potentiometric end group titration to determine the exact molar mass of the Jeffamine. The titration was done with 0.1N HCl in isopropanol solution. The resulting molar masses were used to calculate the Jeffamine to perylene ratio in the upcoming reaction procedures.

General procedure

A stainless-steel metal reactor, with a wall thickness of 7 mm, was pre-heated to 80 °C under constant argon flow. After one hour, PTCDA (392, 2 g mol⁻¹, 1 eq.) was filled into the metal reactor and Jeffamine ED-900 (894 g mol⁻¹, 0.625 eq.) and Jeffamine ED-2003 (2018 g mol⁻¹, 0.625 eq.) or solely Jeffamine ED-2003 (2018 g mol⁻¹, 1.25 eq.), respectively, were added in the metal reactor. The reactor was sealed with a HNBR rubber on top and the mixture was heated up to 200 °C and stirred for 25 hours at least under inert conditions. The reaction progress was monitored *via* FT-IR spectroscopy. The resulting (AB)_n segmented copolymer was used as received for further processing.

FT-IR (cm⁻¹): 3500, 3120, 2870, 1770, 1755, 1730, 1696, 1653, 1593, 1506, 1456, 1406, 1344, 1300, 1233, 1093, 1017, 937, 860, 810, 758, 745, 730.



¹H-NMR (300 MHz, THF-d₅): δ (ppm) = 8.2-8.6 (m, 80H, perylene-CH^a), 3.2-4.5 (m, 100H, CH₂^b), 0.7-1.9 (m, 120H, CH₃^c).

DSC (2nd heating, 10 K min⁻¹):

2a (PTCDI-Jeff(900/2003)-PTCDA): $T_{m,Jeff}$: 13 °C; $T_{m,Pery}$: 174 °C

2b (PTCDI-Jeff(2003)-PTCDA): $T_{m,Jeff}$: 25 °C; $T_{m,Pery}$: 104 °C

TGA (5%-weight loss):

2a (PTCDI-Jeff(900/2003)-PTCDA): 395 °C

2b (PTCDI-Jeff(2003)-PTCDA): 395 °C

Yield: 40 g

4.6 Synthesis of graphene via chemical vapor deposition

Nickel foil sheets with a size of 1x7 cm were punched out of a nickel foil. A nickel foil sheet was placed in between two resistance heaters inside an evaporation chamber. The temperature of the used Nickel foil was calibrated based on the melting points of various materials in vacuum while increasing the power of the resistance heaters (cf. figure **Figure 73**).

General procedure of the graphene synthesis

The nickel foil was placed in between the resistance heaters and the naphthalene was placed in a tungsten boat below the nickel foil. A shutter was used to avoid sublimation of naphthalene before the temperature was reached (cf **Figure 73**). Once the aimed temperature was reached the shutter was opened and the naphthalene was sublimated onto the hot nickel surface as depicted in the picture below. The amount of naphthalene was monitored using quartz microbalances or by measuring the weight of the naphthalene placed in the tungsten boat.

Different temperatures were used, an overview is shown in **Table 9**.

Higher than 800 °C graphite and multilayer graphene could be observed. Best results could be achieved at 1170°C with bilayer graphene.

5. References

- [1] A. Manthiram,
"An Outlook on Lithium Ion Battery Technology",
ACS central science **2017**, *3*, 1063.
- [2] A. Manthiram,
"A reflection on lithium-ion battery cathode chemistry",
Nature communications **2020**, *11*, 1550.
- [3] J. Schnell, T. Günther, T. Knoche, C. Vieider, L. Köhler, A. Just, M. Keller, S. Passerini, G. Reinhart,
"All-solid-state lithium-ion and lithium metal batteries – paving the way to large-scale production",
Journal of Power Sources **2018**, *382*, 160.
- [4] S. Nowak, M. Winter,
"Elemental analysis of lithium ion batteries",
J. Anal. At. Spectrom. **2017**, *32*, 1833.
- [5] M. Armand, P. Axmann, D. Bresser, M. Copley, K. Edström, C. Ekberg, D. Guyomard, B. Lestriez, P. Novák, M. Petranikova, W. Porcher, S. Trabesinger, M. Wohlfahrt-Mehrens, H. Zhang,
"Lithium-ion batteries – Current state of the art and anticipated developments",
Journal of Power Sources **2020**, *479*, 228708.
- [6] J.-Y. Hwang, S.-T. Myung, Y.-K. Sun,
"Sodium-ion batteries: present and future",
Chemical Society reviews **2017**, *46*, 3529.
- [7] P. Leung, X. Li, C. Ponce de León, L. Berlouis, C. T. J. Low, F. C. Walsh,
"Progress in redox flow batteries, remaining challenges and their applications in energy storage",
RSC Adv. **2012**, *2*, 10125.
- [8] M. B. Armand, in *Materials for Advanced Batteries* (Eds.: D. W. Murphy, J. Broadhead, B. C. H. Steele), Springer US. Boston, MA **1980**, p. 145.
- [9] G. E. Blomgren,
"The Development and Future of Lithium Ion Batteries",
J. Electrochem. Soc. **2017**, *164*, A5019-A5025.
- [10] A. M. Haregewoin, A. S. Wotango, B.-J. Hwang,
"Electrolyte additives for lithium ion battery electrodes: progress and perspectives",
Energy Environ. Sci. **2016**, *9*, 1955.
- [11] R. Chen, Q. Li, X. Yu, L. Chen, H. Li,
"Approaching Practically Accessible Solid-State Batteries: Stability Issues Related to Solid

- Electrolytes and Interfaces",
Chemical reviews **2020**, *120*, 6820.
- [12] Q. Wang, P. Ping, X. Zhao, G. Chu, J. Sun, C. Chen,
"Thermal runaway caused fire and explosion of lithium ion battery",
Journal of Power Sources **2012**, *208*, 210.
- [13] Q. Wang, L. Jiang, Y. Yu, J. Sun,
"Progress of enhancing the safety of lithium ion battery from the electrolyte aspect",
Nano Energy **2019**, *55*, 93.
- [14] L. Yue, J. Ma, J. Zhang, J. Zhao, S. Dong, Z. Liu, G. Cui, L. Chen,
"All solid-state polymer electrolytes for high-performance lithium ion batteries",
Energy Storage Materials **2016**, *5*, 139.
- [15] C. Sun, J. Liu, Y. Gong, D. P. Wilkinson, J. Zhang,
"Recent advances in all-solid-state rechargeable lithium batteries",
Nano Energy **2017**, *33*, 363.
- [16] F. Zheng, M. Kotobuki, S. Song, M. O. Lai, L. Lu,
"Review on solid electrolytes for all-solid-state lithium-ion batteries",
Journal of Power Sources **2018**, *389*, 198.
- [17] P. Yao, H. Yu, Z. Ding, Y. Liu, J. Lu, M. Lavorgna, J. Wu, X. Liu,
"Review on Polymer-Based Composite Electrolytes for Lithium Batteries",
Frontiers in chemistry **2019**, *7*, 522.
- [18] *Principles and applications of lithium secondary batteries*,
Wiley-VCH, Weinheim **2012**.
- [19] J. Asenbauer, T. Eisenmann, M. Kuenzel, A. Kazzazi, Z. Chen, D. Bresser,
"The success story of graphite as a lithium-ion anode material – fundamentals, remaining
challenges, and recent developments including silicon (oxide) composites",
Sustainable Energy Fuels **2020**, *4*, 5387.
- [20] Y. Jing, Z. Zhou, C. R. Cabrera, Z. Chen,
"Graphene, inorganic graphene analogs and their composites for lithium ion batteries",
J. Mater. Chem. A **2014**, *2*, 12104.
- [21] L. Long, S. Wang, M. Xiao, Y. Meng,
"Polymer electrolytes for lithium polymer batteries",
J. Mater. Chem. A **2016**, *4*, 10038.
- [22] N. Nitta, F. Wu, J. T. Lee, G. Yushin,
"Li-ion battery materials: present and future",
Materials Today **2015**, *18*, 252.

- [23] W. Xu, J. Wang, F. Ding, X. Chen, E. Nasybulin, Y. Zhang, J.-G. Zhang, "Lithium metal anodes for rechargeable batteries", *Energy Environ. Sci.* **2014**, *7*, 513.
- [24] X.-B. Cheng, R. Zhang, C.-Z. Zhao, Q. Zhang, "Toward Safe Lithium Metal Anode in Rechargeable Batteries: A Review", *Chemical reviews* **2017**, *117*, 10403.
- [25] C. Yang, K. Fu, Y. Zhang, E. Hitz, L. Hu, "Protected Lithium-Metal Anodes in Batteries: From Liquid to Solid", *Advanced materials (Deerfield Beach, Fla.)* **2017**, *29*.
- [26] C. Julien, A. Mauger, A. Vijn, K. Zaghib, *Lithium Batteries: Science and Technology*, Springer, Cham **2016**.
- [27] A. Mauger, M. Armand, C. M. Julien, K. Zaghib, "Challenges and issues facing lithium metal for solid-state rechargeable batteries", *Journal of Power Sources* **2017**, *353*, 333.
- [28] P. Verma, P. Maire, P. Novák, "A review of the features and analyses of the solid electrolyte interphase in Li-ion batteries", *Electrochimica Acta* **2010**, *55*, 6332.
- [29] A. Wang, S. Kadam, H. Li, S. Shi, Y. Qi, "Review on modeling of the anode solid electrolyte interphase (SEI) for lithium-ion batteries", *npj Comput Mater* **2018**, *4*.
- [30] S. K. Heiskanen, J. Kim, B. L. Lucht, "Generation and Evolution of the Solid Electrolyte Interphase of Lithium-Ion Batteries", *Joule* **2019**, *3*, 2322.
- [31] J. O. Besenhard, M. Winter, J. Yang, W. Biberacher, "Filming mechanism of lithium-carbon anodes in organic and inorganic electrolytes", *Journal of Power Sources* **1995**, *54*, 228.
- [32] X.-B. Cheng, M.-Q. Zhao, C. Chen, A. Pentecost, K. Maleski, T. Mathis, X.-Q. Zhang, Q. Zhang, J. Jiang, Y. Gogotsi, "Nanodiamonds suppress the growth of lithium dendrites", *Nature communications* **2017**, *8*, 336.
- [33] G. Wan, F. Guo, H. Li, Y. Cao, X. Ai, J. Qian, Y. Li, H. Yang, "Suppression of Dendritic Lithium Growth by in Situ Formation of a Chemically Stable and Mechanically Strong Solid Electrolyte Interphase", *ACS applied materials & interfaces* **2018**, *10*, 593.

- [34] K. Xu,
"Electrolytes and interphases in Li-ion batteries and beyond",
Chemical reviews **2014**, *114*, 11503.
- [35] M. S. Ding, K. Xu, S. S. Zhang, K. Amine, G. L. Henriksen, T. R. Jow,
"Change of Conductivity with Salt Content, Solvent Composition, and Temperature for
Electrolytes of LiPF₆ in Ethylene Carbonate-Ethyl Methyl Carbonate",
J. Electrochem. Soc. **2001**, *148*, A1196.
- [36] A. Manthiram, X. Yu, S. Wang,
"Lithium battery chemistries enabled by solid-state electrolytes",
Nat Rev Mater **2017**, *2*.
- [37] J. B. Goodenough, K.-S. Park,
"The Li-ion rechargeable battery: a perspective",
Journal of the American Chemical Society **2013**, *135*, 1167.
- [38] D. E. Fenton, J. M. Parker, P. V. Wright,
"Complexes of alkali metal ions with poly(ethylene oxide)",
Polymer **1973**, *14*, 589.
- [39] X. Wang, X. Lu, B. Liu, Di Chen, Y. Tong, G. Shen,
"Flexible energy-storage devices: design consideration and recent progress",
Advanced materials (Deerfield Beach, Fla.) **2014**, *26*, 4763.
- [40] Y. Hu, X. Sun,
"Flexible rechargeable lithium ion batteries: advances and challenges in materials and process
technologies",
J. Mater. Chem. A **2014**, *2*, 10712.
- [41] B. Sun, J. Mindemark, K. Edström, D. Brandell,
"Polycarbonate-based solid polymer electrolytes for Li-ion batteries",
Solid State Ionics **2014**, *262*, 738.
- [42] Y. Jiang, X. Yan, Z. Ma, P. Mei, W. Xiao, Q. You, Y. Zhang,
"Development of the PEO Based Solid Polymer Electrolytes for All-Solid State Lithium Ion
Batteries",
Polymers **2018**, *10*.
- [43] P. Chu,
"Sm₂O₃ composite PEO solid polymer electrolyte",
Journal of Power Sources **2003**, *115*, 288.
- [44] X. Zhang, J. Xie, F. Shi, D. Lin, Y. Liu, W. Liu, A. Pei, Y. Gong, H. Wang, K. Liu, Y. Xiang, Y. Cui,
"Vertically Aligned and Continuous Nanoscale Ceramic-Polymer Interfaces in Composite Solid

- Polymer Electrolytes for Enhanced Ionic Conductivity",
Nano letters **2018**, *18*, 3829.
- [45] W. Li, Y. Pang, J. Liu, G. Liu, Y. Wang, Y. Xia,
"A PEO-based gel polymer electrolyte for lithium ion batteries",
RSC Adv. **2017**, *7*, 23494.
- [46] M. Y. Zhang, M. X. Li, Z. Chang, Y. F. Wang, J. Gao, Y. S. Zhu, Y. P. Wu, W. Huang,
"A Sandwich PVDF/HEC/PVDF Gel Polymer Electrolyte for Lithium Ion Battery",
Electrochimica Acta **2017**, *245*, 752.
- [47] V. Bocharova, A. P. Sokolov,
"Perspectives for Polymer Electrolytes: A View from Fundamentals of Ionic Conductivity",
Macromolecules **2020**, *53*, 4141.
- [48] Z. Xue, D. He, X. Xie,
"Poly(ethylene oxide)-based electrolytes for lithium-ion batteries",
J. Mater. Chem. A **2015**, *3*, 19218.
- [49] R. C. Agrawal, G. P. Pandey,
"Solid polymer electrolytes: materials designing and all-solid-state battery applications: an overview",
J. Phys. D: Appl. Phys. **2008**, *41*, 223001.
- [50] M. S. Grewal, M. Tanaka, H. Kawakami,
"Bifunctional poly(ethylene glycol) based crosslinked network polymers as electrolytes for all-solid-state lithium ion batteries",
Polym. Int. **2019**, *68*, 684.
- [51] P. Han, Y. Zhu, J. Liu,
"An all-solid-state lithium ion battery electrolyte membrane fabricated by hot-pressing method",
Journal of Power Sources **2015**, *284*, 459.
- [52] W.-S. Young, W.-F. Kuan, T. H. Epps,
"Block copolymer electrolytes for rechargeable lithium batteries",
J. Polym. Sci. Part B: Polym. Phys. **2014**, *52*, 1.
- [53] A. Panday, S. Mullin, E. D. Gomez, N. Wanakule, V. L. Chen, A. Hexemer, J. Pople, N. P. Balsara,
"Effect of Molecular Weight and Salt Concentration on Conductivity of Block Copolymer Electrolytes",
Macromolecules **2009**, *42*, 4632.

- [54] B. Huang, Z. Pan, X. Su, L. An,
"Recycling of lithium-ion batteries: Recent advances and perspectives",
Journal of Power Sources **2018**, 399, 274.
- [55] W. Lee, S. Muhammad, C. Sergey, H. Lee, J. Yoon, Y.-M. Kang, W.-S. Yoon,
"Advances in the Cathode Materials for Lithium Rechargeable Batteries",
Angewandte Chemie (International ed. in English) **2020**, 59, 2578.
- [56] E. M. C. Jones, Ö. Ö. Çapraz, S. R. White, N. R. Sottos,
"Reversible and Irreversible Deformation Mechanisms of Composite Graphite Electrodes in
Lithium-Ion Batteries",
J. Electrochem. Soc. **2016**, 163, A1965-A1974.
- [57] R. Yazami, P. Touzain,
"A reversible graphite-lithium negative electrode for electrochemical generators",
Journal of Power Sources **1983**, 9, 365.
- [58] M. Pfanzelt, P. Kubiak, M. Fleischhammer, M. Wohlfahrt-Mehrens,
"TiO₂ rutile—An alternative anode material for safe lithium-ion batteries",
Journal of Power Sources **2011**, 196, 6815.
- [59] M. Ge, J. Rong, X. Fang, C. Zhou,
"Porous doped silicon nanowires for lithium ion battery anode with long cycle life",
Nano letters **2012**, 12, 2318.
- [60] U. Maver, A. Žnidaršič, M. Gaberšček,
"An attempt to use atomic force microscopy for determination of bond type in lithium battery
electrodes",
J. Mater. Chem. **2011**, 21, 4071.
- [61] X. Yang, G. Zhang, J. Prakash, Z. Chen, M. Gauthier, S. Sun,
"Chemical vapour deposition of graphene: layer control, the transfer process, characterisation,
and related applications",
International Reviews in Physical Chemistry **2019**, 38, 149.
- [62] S. Yang, M. R. Lohe, K. Müllen, X. Feng,
"New-Generation Graphene from Electrochemical Approaches: Production and Applications",
Advanced materials (Deerfield Beach, Fla.) **2016**, 28, 6213.
- [63] K. P. Loh, S. W. Tong, J. Wu,
"Graphene and Graphene-like Molecules: Prospects in Solar Cells",
Journal of the American Chemical Society **2016**, 138, 1095.

- [64] M. Cai, D. Thorpe, D. H. Adamson, H. C. Schniepp,
"Methods of graphite exfoliation",
J. Mater. Chem. **2012**, *22*, 24992.
- [65] M. El Gemayel, A. Narita, L. F. Dössel, R. S. Sundaram, A. Kiersnowski, W. Pisula, M. R. Hansen,
A. C. Ferrari, E. Orgiu, X. Feng, K. Müllen, P. Samorì,
"Graphene nanoribbon blends with P3HT for organic electronics",
Nanoscale **2014**, *6*, 6301.
- [66] W. Yang, M. Ni, X. Ren, Y. Tian, N. Li, Y. Su, X. Zhang,
"Graphene in Supercapacitor Applications",
Current Opinion in Colloid & Interface Science **2015**, *20*, 416.
- [67] M. E. Foo, S. C. B. Gopinath,
"Feasibility of graphene in biomedical applications",
Biomedicine & pharmacotherapy = Biomedecine & pharmacotherapie **2017**, *94*, 354.
- [68] J. Zhu, R. Duan, S. Zhang, N. Jiang, Y. Zhang, J. Zhu,
"The application of graphene in lithium ion battery electrode materials",
SpringerPlus **2014**, *3*, 585.
- [69] J. Zhang, B. Guo, Y. Yang, W. Shen, Y. Wang, X. Zhou, H. Wu, S. Guo,
"Large scale production of nanoporous graphene sheets and their application in lithium ion
battery",
Carbon **2015**, *84*, 469.
- [70] K. Parvez, S. Yang, X. Feng, K. Müllen,
"Exfoliation of graphene via wet chemical routes",
Synthetic Metals **2015**, *210*, 123.
- [71] M. Yi, Z. Shen,
"A review on mechanical exfoliation for the scalable production of graphene",
J. Mater. Chem. A **2015**, *3*, 11700.
- [72] D. G. Matej, N.-E. Weber, S. Kurasch, S. Wundrack, M. Woszczyna, M. Grothe, T. Weimann, F.
Ahlers, R. Stosch, U. Kaiser, A. Turchanin,
"Functional single-layer graphene sheets from aromatic monolayers",
Advanced materials (Deerfield Beach, Fla.) **2013**, *25*, 4146.
- [73] N. Mishra, J. Boeckl, N. Motta, F. Iacopi,
"Graphene growth on silicon carbide: A review",
Phys. Status Solidi A **2016**, *213*, 2277.
- [74] J. K. Wassei, M. Mecklenburg, J. A. Torres, J. D. Fowler, B. C. Regan, R. B. Kaner, B. H. Weiller,
"Chemical vapor deposition of graphene on copper from methane, ethane and propane:

- evidence for bilayer selectivity",
Small (Weinheim an der Bergstrasse, Germany) **2012**, *8*, 1415.
- [75] M. R. Anisur, P. Chakraborty Banerjee, C. D. Easton, R. K. Singh Raman,
"Controlling hydrogen environment and cooling during CVD graphene growth on nickel for improved corrosion resistance",
Carbon **2018**, *127*, 131.
- [76] S. Xu, L. Zhang, B. Wang, R. S. Ruoff,
"Chemical vapor deposition of graphene on thin-metal films",
Cell Reports Physical Science **2021**, *2*, 100372.
- [77] M. Losurdo, M. M. Giangregorio, P. Capezzuto, G. Bruno,
"Graphene CVD growth on copper and nickel: role of hydrogen in kinetics and structure",
Physical chemistry chemical physics PCCP **2011**, *13*, 20836.
- [78] C.-M. Seah, S.-P. Chai, A. R. Mohamed,
"Mechanisms of graphene growth by chemical vapour deposition on transition metals",
Carbon **2014**, *70*, 1.
- [79] A. C. Ferrari, D. M. Basko,
"Raman spectroscopy as a versatile tool for studying the properties of graphene",
Nature nanotechnology **2013**, *8*, 235.
- [80] A. C. Ferrari, J. C. Meyer, V. Scardaci, C. Casiraghi, M. Lazzeri, F. Mauri, S. Piscanec, Da Jiang, K. S. Novoselov, S. Roth, A. K. Geim **2006**.
- [81] V. A. Sugiawati, F. Vacandio, T. Djenizian,
"All-Solid-State Lithium Ion Batteries Using Self-Organized TiO₂ Nanotubes Grown from Ti-6Al-4V Alloy",
Molecules (Basel, Switzerland) **2020**, *25*.
- [82] K. Ishizu, S. Uchida,
"Ordered lattice formation of (AB)_n type star copolymers",
Polymer **1994**, *35*, 4712.
- [83] B. Xu, Y. G. Lin, J. C. W. Chien,
"Energetic ABA and (AB)_n thermoplastic elastomers",
J. Appl. Polym. Sci. **1992**, *46*, 1603.
- [84] S. M. Barbon, J.-A. Song, D. Chen, C. Zhang, J. Lequieu, K. T. Delaney, A. Anastasaki, M. Rolland, G. H. Fredrickson, M. W. Bates, C. J. Hawker, C. M. Bates,
"Architecture Effects in Complex Spherical Assemblies of (AB)_n -Type Block Copolymers",
ACS Macro Lett. **2020**, *9*, 1745.

- [85] J. Mechau, A. Frank, E. Bakirci, S. Gumbel, T. Jungst, R. Giesa, J. Groll, P. D. Dalton, H.-W. Schmidt,
"Hydrophilic (AB)_n Segmented Copolymers for Melt Extrusion-Based Additive Manufacturing",
Macromol. Chem. Phys. **2021**, *222*, 2000265.
- [86] G. Hochleitner, E. Fürsattel, R. Giesa, J. Groll, H.-W. Schmidt, P. D. Dalton,
"Melt Electrowriting of Thermoplastic Elastomers",
Macromolecular rapid communications **2018**, *39*, e1800055.
- [87] Q. Guan, B. Norder, L. Chu, N. A. M. Besseling, S. J. Picken, T. J. Dingemans,
"All-Aromatic (AB)_n-Multiblock Copolymers via Simple One-Step Melt Condensation
Chemistry",
Macromolecules **2016**, *49*, 8549.
- [88] M. Jin, M. Stihl, R. Giesa, C. Neuber, H.-W. Schmidt,
"(AB)_n Segmented Copolyetherimides for 4D Printing",
Macromol. Mater. Eng. **2021**, *306*, 2000473.
- [89] R. J. Spontak, S. D. Smith,
"Perfectly-alternating linear (AB)_n multiblock copolymers: Effect of molecular design on
morphology and properties",
J. Polym. Sci. Part B: Polym. Phys. **2001**, *39*, 947.
- [90] J. M. Zielinski, R. J. Spontak,
"Confined single-chain model of microphase-separated multiblock copolymers. 1. (AB)_n
copolymers",
Macromolecules **1992**, *25*, 653.
- [91] M. Guo, L. M. Pitet, H. M. Wyss, M. Vos, P. Y. W. Dankers, E. W. Meijer,
"Tough stimuli-responsive supramolecular hydrogels with hydrogen-bonding network
junctions",
Journal of the American Chemical Society **2014**, *136*, 6969.
- [92] G. Hernández, N. Casado, R. Coste, D. Shanmukaraj, L. Rubatat, M. Armand, D. Mecerreyes,
"Redox-active polyimide–polyether block copolymers as electrode materials for lithium
batteries",
RSC Adv. **2015**, *5*, 17096.
- [93] F. Würthner, C. R. Saha-Möller, B. Fimmel, S. Ogi, P. Leowanawat, D. Schmidt,
"Perylene Bisimide Dye Assemblies as Archetype Functional Supramolecular Materials",
Chemical reviews **2016**, *116*, 962.

- [94] G. Hernández, N. Casado, A. M. Zamarayeva, J. K. Duey, M. Armand, A. C. Arias, D. Mecerreyes, "Perylene Polyimide-Polyether Anodes for Aqueous All-Organic Polymer Batteries", *ACS Appl. Energy Mater.* **2018**, *1*, 7199.
- [95] S. Ma, M. Jiang, P. Tao, C. Song, J. Wu, J. Wang, T. Deng, W. Shang, "Temperature effect and thermal impact in lithium-ion batteries: A review", *Progress in Natural Science: Materials International* **2018**, *28*, 653.
- [96] S. J. An, J. Li, C. Daniel, D. Mohanty, S. Nagpure, D. L. Wood, "The state of understanding of the lithium-ion-battery graphite solid electrolyte interphase (SEI) and its relationship to formation cycling", *Carbon* **2016**, *105*, 52.
- [97] U. Mogera, N. Kurra, D. Radhakrishnan, C. Narayana, G. U. Kulkarni, "Low cost, rapid synthesis of graphene on Ni: An efficient barrier for corrosion and thermal oxidation", *Carbon* **2014**, *78*, 384.

6. Appendix

6.1 Additional topics investigated during the PhD

During this thesis several additional topics were investigated. Selected topics are discussed in the upcoming chapters.

6.1.1 Physical vapor deposition of hole transport material for perovskite solar cell applications
Physical vapor deposition of hole materials for perovskite solar cell applications. This work was published in ACS, "Applied energy materials", DOI: 10.1021/acsaem.9b00260.

7. Acknowledgment

An dieser Stelle möchte ich mich bei allen Personen bedanken ohne deren Unterstützung diese Arbeit nicht möglich gewesen wäre.

Zuallererst möchte ich mich bei Herrn Prof. Dr. Hans-Werner Schmidt für die Möglichkeit bedanken meine Dissertation in seiner Arbeitsgruppe, der Makromolekular Chemie I, durchführen zu können. Besonderer Dank gilt hier den vielfältigen, interessanten Themenstellungen, die gute Betreuung sowie die Möglichkeit Ideen einzubringen und diese während meiner Arbeit umzusetzen. Die fortlaufend hilfreichen Diskussionen und neue Ideen trugen sehr stark zum erfolgreichen Abschluss der Doktorarbeit bei.

Ebenfalls möchte ich mich für die finanzielle Unterstützung des *Solar Technology Goes Hybrid (SolTech)* Projekts bedanken.

Ein sehr großer Dank geht an Dr. Christian Neuber, für die unzähligen Hilfestellungen und die fortlaufende Unterstützung während der gesamten Promotion. Die Tür war immer offen!

Vielen Dank auch die *Battery Crew*: Domi, Alex und Jannik für die Unterstützung bei allen Batterithemen.

Danke an Alex, Sandra und Jutta für die Hilfe rund um technische Themen und Fragestellungen.

Petra und Christina verdienen einen besonderen Dank. Ohne sie würde der Lehrstuhl nicht so laufen wie er es immer getan hat.

Bei Andi Frank, Dr. Holger Schmalz und Dr. Wolfgang Milius möchte ich mich für REM, Raman bzw. XRD Messungen bedanken.

Dem gesamten MC I Lehrstuhl danke ich für die fantastische Atmosphäre die über Jahre stets geherrscht hat, die auch über die Uni hinaus für gute Stimmung gesorgt hat.

Ich möchte ebenfalls Christian Hils und Johannes von Szczepanski danken, die durch ihre Praktika bzw. Masterarbeit das Projekt ebenfalls unterstützt haben.

Ein riesiger Dank geht an meine Freunde und meine Familie ohne die das gesamte Studium, inklusive Promotion, niemals möglich gewesen wäre. Ihr habt mich allzeit unterstützt und ward immer für einen da!

Last but not least möchte ich mich bei Karina bedanken, dass sie mich auch in nicht so guten Zeiten stets unterstützt hat und auch damit dazu beigetragen hat, dass diese Arbeit erfolgreich fertiggestellt wurde.

8. (Eidesstattliche) Versicherungen und Erklärungen

(§ 9 Satz 2 Nr. 3 PromO BayNAT)

Hiermit versichere ich eidesstattlich, dass ich die Arbeit selbstständig verfasst und keine anderen als die von mir angegebenen Quellen und Hilfsmittel benutzt habe (vgl. Art. 97 Abs. 1 Satz 8 BayHIG).

(§ 9 Satz 2 Nr. 3 PromO BayNAT)

Hiermit erkläre ich, dass ich die Dissertation nicht bereits zur Erlangung eines akademischen Grades eingereicht habe und dass ich nicht bereits diese oder eine gleichartige Doktorprüfung endgültig nicht bestanden habe.

(§ 9 Satz 2 Nr. 4 PromO BayNAT)

Hiermit erkläre ich, dass ich Hilfe von gewerblichen Promotionsberatern bzw. -vermittlern oder ähnlichen Dienstleistern weder bisher in Anspruch genommen habe noch künftig in Anspruch nehmen werde.

(§ 9 Satz 2 Nr. 7 PromO BayNAT)

Hiermit erkläre ich mein Einverständnis, dass die elektronische Fassung meiner Dissertation unter Wahrung meiner Urheberrechte und des Datenschutzes einer gesonderten Überprüfung unterzogen werden kann.

(§ 9 Satz 2 Nr. 8 PromO BayNAT)

Hiermit erkläre ich mein Einverständnis, dass bei Verdacht wissenschaftlichen Fehlverhaltens Ermittlungen durch universitätsinterne Organe der wissenschaftlichen Selbstkontrolle stattfinden können.

.....

Ort, Datum

Unterschrift

